Tilting of Surficial Strata and Groundwater Level Fluctuations in the Subsiding Mimbres Basin, New Mexico

By

William C. Haneberg
Principal Investigator
New Mexico Bureau of Mines and Mineral Resources
New Mexico Institute of Mining and Technology

and

Robert L. Friesen
Graduate Research Assistant
New Mexico Bureau of Mines and Mineral Resources
New Mexico Institute of Mining and Technology

TECHNICAL COMPLETION REPORT

Project Number 1423954

February 1993

New Mexico Water Resources Research Institute

in cooperation with

New Mexico Bureau of Mines and Mineral Resources

The research on which this report is based was financed in part by the U.S. Department of the Interior, Geological Survey, through the New Mexico Water Resources Research Institute. Additional funding was provided by the New Mexico Water Resources Research Institute, the New Mexico Bureau of Mines and Mineral Resources, and the New Mexico Institute of Mining and Technology Graduate Office.

DISCLAIMER

The purpose of Water Resources Research Institute technical reports is to provide a timely outlet for research results obtained on projects supported in whole or in part by the institute. Through these reports, we are promoting the free exchange of information and ideas, and hope to stimulate thoughtful discussion and actions that may lead to resolution of water problems. The WRRI, through peer review of draft reports, attempts to substantiate the accuracy of information contained in its reports, but the views expressed are those of the authors and do not necessarily reflect the views and policies of the U.S. Department of the Interior, nor does mention of trade names or commercial products constitute their endorsement by the United States government.

ACKNOWLEDGEMENTS

We wish to acknowledge several people whose efforts contributed to the success of this project. John Hawley and David Love provided field assistance and background materials; June Cox continued to allow access to the fissure on her land for scientific study; Bill Bedford kept watch over the instrumentation at our field site; Dan Detmer compiled well logs and assisted with sample analysis; and Larry Johnson and the employees of LarJon Drilling provided drilling services. In addition, this work could not have been completed without the budgetary expertise of Patricia McLain, Darlene Reeves, Judy Vaiza, and Lois Devlin. Technical reviews by Mike Carpenter of the U.S. Geological Survey and Gary Holzhausen of Applied Geomechanics, Inc. improved the present report and provided valuable suggestions for future work. Editorial comments by Cathy Ortega-Klett of NM Water Resources Research Institute also helped to bring the report into compliance with NMWRRI standards.

This study was funded by the U.S. Geological Survey (award number 14-08-0001-G2108), the New Mexico Water Resources Research Institute (project number 1423954), and the New Mexico Bureau of Mines and Mineral Resources. In addition, Robert Friesen was supported in part by a New Mexico Institute of Mining and Technology research fellowship.

ABSTRACT

Tilts and water levels near an earth fissure in the Mimbres Basin of southern New Mexico were monitored between January and September 1992, using a network of borehole tiltmeters and piezometers fitted with water level transducers. The objective of this study was to compare observed tilts near the fissure with the deformation patterns predicted by existing models of plane strain draping and differential compaction. Short-term tilt and water level records exhibit diurnal and semi-diurnal cycles superimposed on long-term trends, which can be explained using a regression model that includes earth tide, barometric, and annual irrigation harmonics, plus a linear monotonic trend. Daily water level maxima generally correspond to daily tilt maxima, and suggest that the fissure closes as water level rises. Long-term records (tens to hundreds of days) show complicated patterns of oblique tilt both toward and away from the fissure. These patterns are inconsistent with a model of simple plane strain stretching perpendicular to the fissure, and are not easily correlated with long-term changes in water level beneath the fissure. A model of an elastic plate subjected to complicated loading suggests that highly variable tilts may be a consequence of shallow stratigraphic and/or structural irregularities.

key words— fissures (geology), land subsidence, overdraft, soil mechanics, stress

TABLE OF CONTENTS

LIST OF FIGURES

LIST OF TABLES

INTRODUCTION

GOALS

This study was undertaken in order to 1) observe deformation of surficial strata surrounding an earth fissure in response to seasonal groundwater level fluctuations in the Mimbres Basin of New Mexico and 2) determine whether mathematical models developed to analyze the draping and differential compaction of compressible elastic layers adequately describe the observations. Deformation was monitored using a network of four microradian-sensitivity borehole tiltmeters and two piezometers installed near the earth fissure. Observed tilt patterns were much more complicated than those predicted by simple models of plane strain perpendicular to the fissure; therefore, the scope of the study was expanded to include preliminary work on an alternative model of surficial deformation resulting from subsidence of a hypothetical groundwater basin. This study will be of interest to those interested in measuring small ground deformation associated with various forms of land subsidence, to those interested in the prediction and/or avoidance of areas susceptible to fissuring, and to those interested in the origin of earth fissures. This report summarizes work conducted between July 1991 and October 1992 by the principal investigator and one graduate research assistant. Copies of two papers related to this project are included as appendices, and additional material is contained in a New Mexico Institute of Mining and Technology Master of Science thesis in Mineral Engineering (Friesen 1992).

GEOLOGIC SETTING

The Mimbres Basin lies within the Mexican Highlands Section of the Basin and Range physiographic province (Gile et al. 1981). The basin is a closed drainage basin that includes portions of Grant, Sierra and Dona Ana counties and most of Luna County in southwestern New Mexico. Clemons (1986) indicated that, prior to Basin and Range style deformation, much of central Luna County was covered by Tertiary volcanic rocks consisting primarily of Oligocene ashflow tuffs along with scattered rhyolite and basaltic andesite flows. These materials buried older rocks that had been exposed by the Laramide orogeny, which was waning by late Eocene time (Seager 1983). Basin and Range style deformation began in middle Miocene time with the onset of extensional faulting (Clemons and Mack 1988). Movement associated with north-northwesterly trending fault zones created the major ranges and adjoining basins present in the area today. The Florida Mountains, as an example, are an east-northeasterly tilted fault block that was uplifted by movement along the West Florida Mountains Fault, which is a range bounding normal fault (figure 1) (Clemons 1992). At the same time, the block opposite the Florida Mountains subsided, forming what is today the Mimbres Basin. Vertical offset along this fault is estimated to be approximately 1200 m (Clemons 1985).

The Mimbres Basin was initially filled with Eocene to Miocene volcanic rocks from adjacent uplift (volcanic) areas. Overlying this material are upper Tertiary to Holocene alluvial sediments that can be divided into two units. The lower unit, lying below 1200 m elevation, is finer grained and contains primarily reddish clays indicative of alluvial fan and playa deposits of mid-Pleistocene age and older. The upper unit, which occurs above 1200 m elevation, consists of interbedded lenses of gravels, sands, silts, and clays that are representative of fan-delta or splay deposits derived from the Mimbres River (Contaldo and Mueller 1991). Clemons (1986) inspected cuttings from four deep wells drilled for gas and oil exploration in the basin near Deming. He established the basin's bedrock floor to be at the top of a consolidated Miocene-Oligocene volcanic sequence. Utilizing this criterion, he determined that the thickness of basin-fill sediments varies from 1290 m east of Deming to 700 m in the area west of Deming and north of Red Mountain. In the graben that lies between the Snake Hills and Seventy-six fault zones, a maximum basin-fill thickness of 1070 m is inferred from analysis of complete Bouguer anomalies within the area (Contaldo and Muller 1991).

HYDROLOGY OF THE MIMBRES BASIN

Main Aquifers

Groundwater resources in the Mimbres Basin were first investigated by Darton (1914). He documented the existence of a large aquifer extending southward from Deming to the foot of the Tres Hermanas mountains and

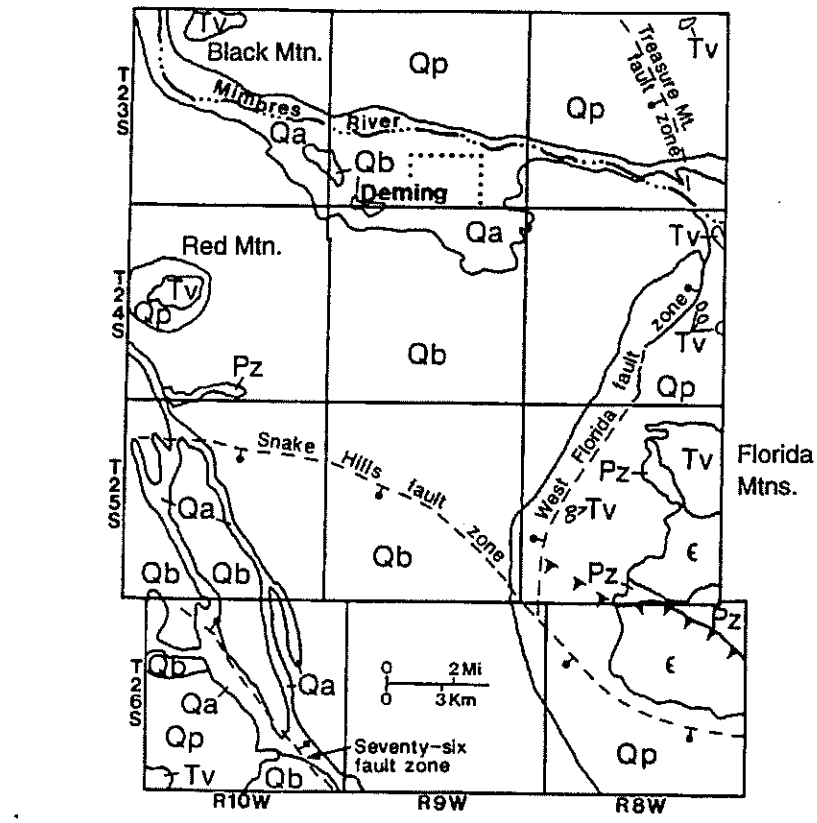

Qa - Quaternary axial river and basin-floor arroyo deposits
Qb - Quaternary basin-floor deposits and fluvial fan deposits of Mimbres River
Qp - Quaternary piedmont-slope deposits
Tv - Tertiary volcanics and volcaniclastics
Pz - Paleozoic sedimentary rocks
Є - Cambrian igneous and metamorphic rocks
- Normal fault, ball and bar on downthrown side, dashed where inferred
- Reverse fault, barbs on upthrown side, dashed where inferred

FIGURE 1. Geology of the Mimbres Basin (Contaldo and Mueller 1991) and index map illustrating location of the Mimbres Basin in south-central New Mexico.

thensoutheastward to the Palomas Lakes in Mexico. Much of the water is contained within highly variable and discontinuous sand and gravel deposits ranging in thickness from as little as 2 m to 15 m (Darton 1914). These deposits form a largely unconfined aquifer within the upper portion of the basin-fill alluvium, generally within 60 m of the surface.

The aquifer is recharged primarily by runoff from the Mimbres Mountains, Black Range, and Cooke's Range, all of which are drained by the Mimbres River. Additionally, some contributions are made by the San Vicente Arroyo which drains the Pinos Altos Range and Silver City area. The upper course of the Mimbres River is perennial as are portions of the San Vicente Arroyo (Theis 1939). However, the lower courses of these drainages are ephemeral, flowing past Deming only during rapid snowmelt or after periods of exceptional rainfall (Darton 1916). Consequently, the recharge to the aquifer is in the form of seepage from the river as it exits the mountains and flows onto unconsolidated basin-fill deposits. Minor amounts of recharge are contributed by runoff from the Florida Mountains (White 1929). Rainfall upon the basin floor, averaging a little less than 25 cm per year, is largely lost through evapotranspiration and hence is a small component of total recharge. However, some recharge may occur in areas with coarse grained soils that allow water to percolate downward, whereas areas with exposed clay deposits tend to pond water for longer periods of time allowing it to evaporate (Contaldo 1989).

Darton (1914) and White (1929) determined that water flows through the aquifer from the northwest to the southeast, following the general topography of the area. The flow velocity of the water averages between 0.5 and 1 m per day (White 1929).

Groundwater Consumption and Overdraft

Groundwater pumping began in the Deming area between 1908 and 1913, coinciding with the arrival of settlers in the area (Darton 1914; Fiedler 1927). The major uses of the water include domestic supply, agricultural irrigation, livestock watering, and industrial needs, with irrigation by far the largest user. At the time of Darton's study (1914), an estimated 200 pumping wells were in operation withdrawing about 12×10^6 m^3 of water per year from the aquifer. Due to various factors, the number of wells decreased to a low of about 25 wells in 1918-19 followed by an increase in pumping beginning in 1923-24 (White 1929). Fiedler (1927) reported 80 pumping wells irrigating 2,000 hectares (ha) in 1927 and, by 1941, the acreage irrigated had increased to 4,900 ha (Conover and Akin 1942). In 1969, this amount had risen to 25,000 ha irrigated within all of Luna County, mostly for sorghum, cotton, and other small grains (NM Interstate Stream Commission 1974). Total groundwater withdrawals within the county in 1970 amounted to 170×10^6 m^3 but have since decreased to lower levels of 138×10^6 m^3 in 1985 and 128×10^6 m^3 in 1990 (Wilson 1986; Wilson 1992). Luna County groundwater withdrawals are projected to rise to 202×10^6 m^3 by the year 2000 and to almost 278×10^6 m^3 by 2020 (NM Interstate Stream Commission 1974).

The effects of pumping groundwater from the Mimbres Basin have been researched by McLean (1977), Contaldo (1989), and Contaldo and Mueller (1991). Prior to the onset of pumping, White (1929) believed that the aquifer system was in a delicate state of equilibrium. Pumping increased discharge from the aquifer so that it soon exceeded the natural recharge into the aquifer. The result was disruption of the equilibrium, and effective mining of the aquifer (White 1929). Contaldo (1989) documented long-term water level declines along with seasonal fluctuations that coincide with agricultural needs. Water levels drop in the spring and summer when irrigation needs are greatest, followed by a recovery period through the fall and winter. However, the recovery level has seldom since reached the pre-irrigation level of the previous year, resulting in a net decline in the water table for the year.

The area experiencing the largest groundwater overdraft is south of Deming in the southcentral portion of the basin (figure 2) (Contaldo 1989). The water table depression forms a cone that is overlain by a region of intense agricultural activity that has been the location of drawdowns in excess of 33 m from 1910 to 1987. The total area affected by dropping water levels is about 880 km^2 (Contaldo and Mueller 1991). Coinciding with the overdraft is subsidence of the land surface within the affected areas. Many cases of land subsidence caused by fluid extraction have been documented in other area (Poland 1984; Lofgren 1976; Holzer 1984; Sato et al. 1984; Larson and Pewe 1986). As water levels drop, the effective stress upon aquifer materials increases, causing reorientation and compaction of the material and, eventually, subsidence of the land surface.

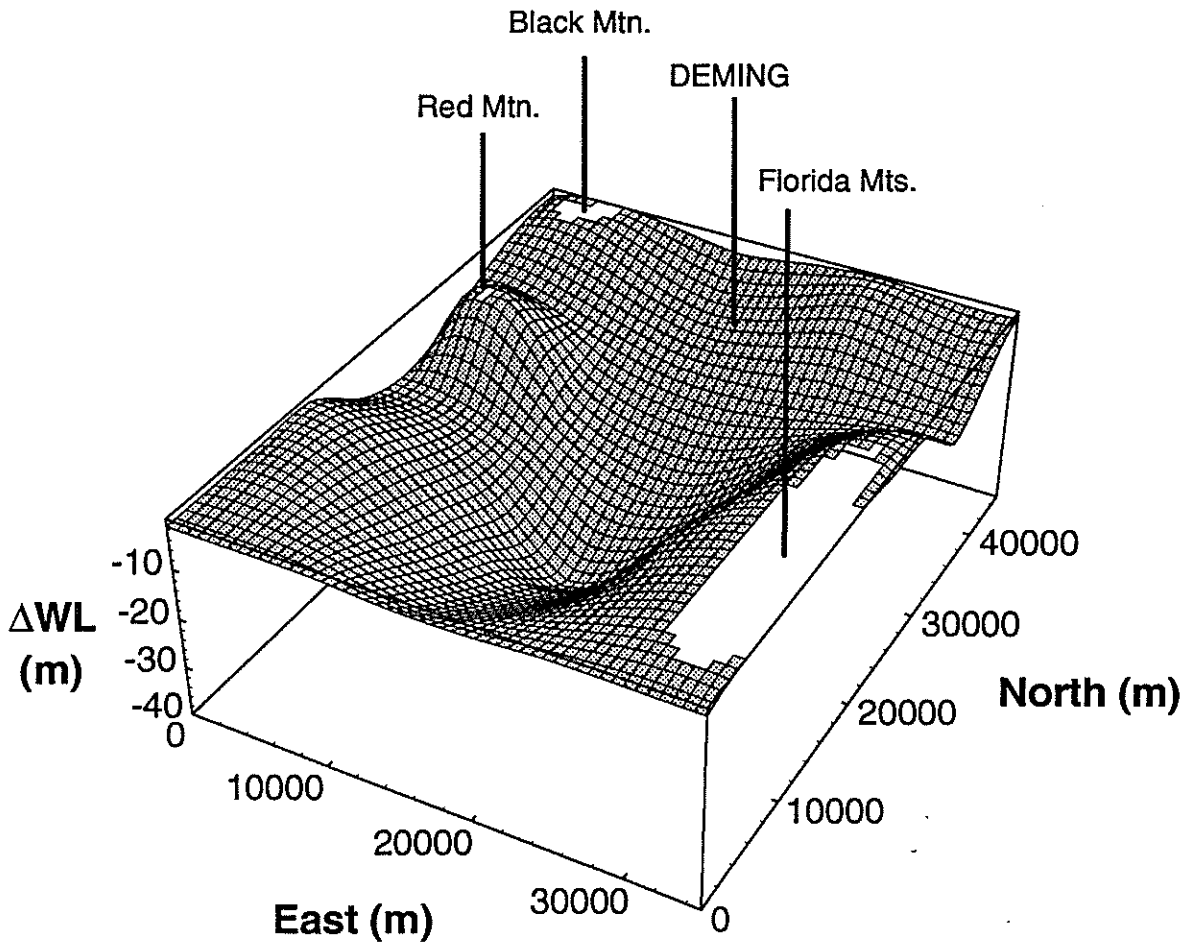

FIGURE 2. Mimbres Basin aquifer drawdowns, 1910-1987. (Interpolated from Contaldo and Mueller 1991).

Contaldo (1989) analyzed data from the National Geodetic Survey, which resurveyed portions of level lines established in 1935. He found that by 1953, approximately 7 cm of subsidence had occurred near the center of the basin, and that the amount of subsidence increased towards the center of the cone of depression. Additionally, two water wells completed near the center of the cone of depression during the 1950s have wells heads protruding 34 and 35 cm above the ground surface, providing a crude estimate of subsidence during between 1955 and 1985 (Contaldo, 1989). These estimates are minimum possible values due to the effects of skin friction and deformation of the well casings. The wells, along with the limited level line survey data, indicate that land subsidence is greatest in the area centered over the cone of depression (Contaldo, 1989). Taken over the 35 year interval, the subsidence near the wells appears to be occurring at a rate of about 1 cm/yr. Contaldo (1989) also constructed drawdown maps for 1910-1987 and 1970-1987, which yield maximum averge drawdown rates of 46 and 48 cm/yr near the center of the basin. Combination of the re-leveling and projecting wellhead estimates suggests that subsidence near the center of the Mimbres basin was at least 40 to 50 cm in 1985.

Domenico and Schwartz (1990, p. 219-220) tabulated values of maximum subsidence and head decrease in 15 basins throughout the world, and found that ratios of subsidence to head decrease ($S/\Delta h$) were clustered into two groups: those with $S/\Delta h \geq 0.09$ and those with $S/\Delta h \leq 0.025$. If both subsidence and head decrease are measured over the same time interval, then the subsidence-to-head ratio is equivalent to the specific compaction, $(\Delta S/\Delta t)/(\Delta h/\Delta t)$, as defined by Carpenter (1986). Average post-1955 subsidence and head decrease rates of approximately 1 cm/yr and 47 cm/yr, respectively, yield a value of $S/\Delta h \leq 0.021$ for the Mimbres Basin. There are, however, serious limitations to this simple empirical approach, which does not take into account factors the duration of time since groundwater overdraft and/or subsidence began, pre-consolidation stresses in compacting clay layers, and elastic storage coefficients. The few available data, nonetheless, suggest that the estimated $S/\Delta h$ ratio of the Mimbres Basin aquifer is comparable to that calculated for other subsiding groundwater basins around the world.

EARTH FISSURES

BACKGROUND

Earth fissures are most commonly found in areas of groundwater overdraft and, consequently, land subsidence, such as alluvial basins of the southwestern United States, where groundwater pumping has occurred largely in response to the needs of agriculture and, to a lesser extent, of metropolitan areas. Fissures have been documented and studied in the south-central Arizona area (Boling 1984; Carpenter 1988; Epstei, 1987; Holzer and Pampeyan 1981; Jachens and Holzer 1979; Larson and Pewe 1986; Sandoval and Bartlett 1991), Las Vegas, Nevada (Holzer and Pampeya, 1981), southwestern New Mexico (Contaldo 1989; Contaldo and Mueller 1991; Haneberg et al. 1991), west Texas (Keaton and Shlemon 1991), San Jacinto Valley, California (Lofgren 1976; Holzer 1984), and Fremont Valley, California (Holzer and Pampeyan 1981). Other occurrences have been reported in Utah (Holzer 1984) and Idaho (Lofgren 1975).

Fissures have also been discovered in areas where groundwater overdraft is inconsequential, including New Mexico (Haneberg et al. 1991), west Texas (Keaton and Shlemon 1991) and in the Dry Lake Valley, Nevada area (Keaton and Miller 1992). Possible causes for fissure formation in these areas include localized subsidence associated with faults (Holzer 1984; Haneberg et al. 1991), neotectonic extension (Keaton and Miller 1992), aseismic fault slip, neotectonic folding, earthquake induced ground failure, or dissolution of soluble mineralogies in the subsurface (Keaton and Shlemon 1991).

Earth fissures are zones of ground failure. Field evidence, such as the appearance of small depressions and/or hairline cracks prior to opening and the observation of eroded portions of fissures beneath unruptured ground, suggests that fissures form as tension cracks in the subsurface (Boling 1984; Holzer 1984; Contaldo 1989). Immediate surface expression, if any, is generally restricted to a crack with only a few millimeters of horizontal separation perpendicular to the trace of the fissure. The evolution of large fissures and voids from small cracks is the result of subsurface erosion or piping. Subsurface ruptures act as pathways for percolating water movement and transport of soils downward. Piping of soil continues until the subsurface void space becomes so large that

overlying material can no longer support itself. The resulting collapse creates a more familiar surface feature consisting of a large deep crack with sharp edges and vertical sidewalls (Pewe 1990). Depths of newly formed fissures are difficult to ascertain due to the constricted opening, however, they are frequently 2 to 3 m deep, with one being measured to a depth of 25 m (Holzer 1984). Fissure widths are commonly on the order of 1 to 2 m but can be much wider. Erosional processes such as slumping and piping continue transporting soil material downward to fill subsurface voids which cause gradual widening of the fissure. Concurrently, the fissure depth decreases as the fissure is gradually filled in. Older fissures appear only as curvilinear surface depressions because of erosional infilling (Contaldo and Mueller 1991).

FISSURE STUDIES IN THE MIMBRES BASIN

Earth fissures within the Mimbres Basin have been studied by Contaldo (1989), Contaldo and Mueller (1991), Haneberg et al. (1991), and Haneberg and Friesen (1992a). A total of 13 fissure locations have been documented, most in the south-central portion of the basin, 10 to 20 km south of Deming, New Mexico (Contaldo and Mueller 1991). The cluster of fissures is centered above the cone of water table declines (figure 3) documented by Contaldo (1989) and McLean (1977). The fissures generally formed in areas in which the water table has fallen more than 21 m, although two fissures are located in areas with water table drops of 18 m and 11 m. The fissures are also temporally associated with water level declines: older fissures are found near the cone apex while younger fissures are found along the cone margin (Contaldo 1989). It appears that the decrease in water table elevation is the driving mechanism for fissure formation.

The locations of fissures within the region affected by water level declines may be controlled by buried bedrock topography. Examination of a complete Bouguer anomaly gravity survey in the basin reveals that most of the fissures may overlie irregularities in bedrock topography (Contaldo 1989). One fissure is located near the Treasure Mountain fault zone east of Deming (figure 1) where gravity data suggest rapid changes in the depth to bedrock. Other fissures, south of Deming, occur near an apparent buried bedrock ridge while still others are located near a steep gravity gradient inferred to represent the Snake Hills fault zone. Variations in thickness of basin-fill alluvium can lead to differential compaction of the aquifer matrix upon dewatering resulting in bending and stretching of the alluvium. This deformation creates tensile stresses and cracks within the alluvium.

It is possible that the bedrock and structural irregularities indicated by the basin-wide gravity survey control the location of fissures within the basin. However, the Snake Hills fault zone strikes northwest-southeast while most of the fissures in the area trend north-south. Fissures formed by draping of sediments over this structural irregularity should also trend in a northwest-southeasterly direction, which is not the case. In addition, faults and other irregularities within the basin-fill alluvium, which may also control fissure formation, have been documented by Haneberg et al. (1991) using seismic reflection surveys on the order of hundreds of meters in length. Hence, the mechanism controlling fissure location within the Mimbres basin cannot be clearly identified at present.

The fissures within the area form one of two distinct patterns: 1) orthogonal to polygonal fissure systems with polygons reaching up to 366 m across, and 2) linear to curvilinear fissures reaching lengths of 614 m (Contaldo 1989). The different fissure forms may be caused by soil variations, including clay content, in the affected areas (Contaldo 1989). Surface expressions of the fissures range from hairline cracks to a series of aligned potholes to openings reaching 9.7 m in width with a maximum measured depth of 12.8 m (Contaldo and Mueller, 1991). Younger fissures typically have sharp vertical walls but are gradually filled in by erosional processes to form shallow troughs and depressions. Others are quickly filled in by ranchers and farmers to prevent injury to cattle and interception of irrigation water. Fissures not filled in often intercept surface drainage and initiate tributary gullying. This results in higher concentrations of soil moisture near the fissure leading to increased vegetation along the fissure (Contaldo 1989).

ORIGIN OF EARTH FISSURES

A number of hypotheses have been put forth in attempts to understand the origin of earth fissures. The theories include differential compaction, seepage forces, capillary stresses, regional basin subsidence, and hydrocompaction. Differential compaction is the most commonly accepted link between water level changes and fissure formation. As groundwater levels drop, the buoyant effect of water, which supports a portion of the overburden stress, decreases so

that the aquifer matrix must carry the additional stress once shared with the water. The increased stress results in reorientation of grains and compaction of the matrix and eventual lowering of the land surface.

The amount of compaction is directly proportional to the thickness of compressible material in the dewatered portion of the aquifer. Changes in the thickness of basin-fill sediments that are draped over shallow buried bedrock irregularities— for example ridges, hills, or fault zones— can give rise to differential vertical compaction. Under large-scale pumping and land subsidence, sediments overlying such topography compact varying amounts and, as a result, are stretched and bent creating tensile stresses within the alluvium. If this stress exceeds the strength of the alluvium, failure will occur. Many fissures are located in areas undergoing horizontal strain that coincide with points of maximum convex upward curvature of the bedrock surface, as determined using shallow gravity (Peterson 1962; Holzer 1984; Jachens and Holzer 1979; Larson and Pewe 1986) and seismic reflection surveys (Haneberg et al. 1991).

In addition to variations in thickness, other causes of differential compaction include the stratigraphic variability of sediments (clays and silts compress more than coarse grained deposits) and variations in permeability, which affect the rate at which water may be expelled from a deposit under increased stress and, hence, vary the rate of its compaction (Pewe 1990). Fault zones may create a groundwater barrier where, under pumping, water levels drop faster on one side of the fault than on the other. This can lead to differential compaction of the sediments over the fault zone (Holzer 1984).

Lofgren (1971) and Helm (1992) proposed that seepage forces created by the flow of water toward a pumping center, could initiate fissure formation. Forces of this type would result in compressional stresses in the vicinity of the pumping center and tensional stresses and concentric crack formation along the periphery of the cone of water level decline. Some instances of fissure formation around the margins of such pumping centers have been documented but many exceptions within the same areas have also been reported (Holzer 1984). Also, some areas that have developed large cones of groundwater level drawdowns, such as Las Vegas, Nevada and Houston, Texas, do not exhibit this pattern of fissuring and contain fissures which, by this theory, would have formed in zones of compression near the wells (Holzer 1984).

Capillary stresses have been suggested as another possible cause of fissure formation. As an aquifer is dewatered, large negative capillary stresses develop in the zone above the dropping water table creating horizontal tensile stresses that would cause the deposit to contract (Holzer 1984). The result would be similar to large desiccation cracks that develop complex polygonal patterns in fine grained sediments of playas studied by Neal et al. (1968). This mechanism may prove important to fissure formation in areas containing fine grained playa-type deposits. However, the desiccation mechanism for fissure development in an alluvial basin environment, with its highly variable basin-fill sediments, has not been rigorously tested (Holzer 1984).

Regional-differential compaction has been used to explain surface faulting associated with petroleum withdrawal and has been shown to produce radial tensile strains around the margins of the subsiding basin. However, the occurrence and orientation of fissures within centers of basins in south-central Arizona and the Houston, Texas area preclude their formation by a regionally controlled compaction process (Holzer 1984). Additionally, Holzer (1984) points out that the broad extent of compacting aquifer systems, relative to their thickness, inhibits horizontal displacements on a basin-wide scale sufficient to initiate fissuring.

SITE CHARACTERIZATION AND INSTRUMENTATION

LOCATION AND GENERAL DESCRIPTION

The fissure described in this report is located within NE 1/4, NE 1/4, Section 32, T25S, R9W. The site is 12 miles due south and 2 miles due west of Deming, New Mexico. The study site lies within an area of gently sloping rounded hills that rise a few meters above surrounding flats and shallow unchanneled drainages (figure 4). A mobile home sits on such a rise at an elevation of 1291 m above sea level. To the north, the site slopes gradually down to a shallow depression that drains in an easterly direction. Another shallow depression exists south of the mobile home.

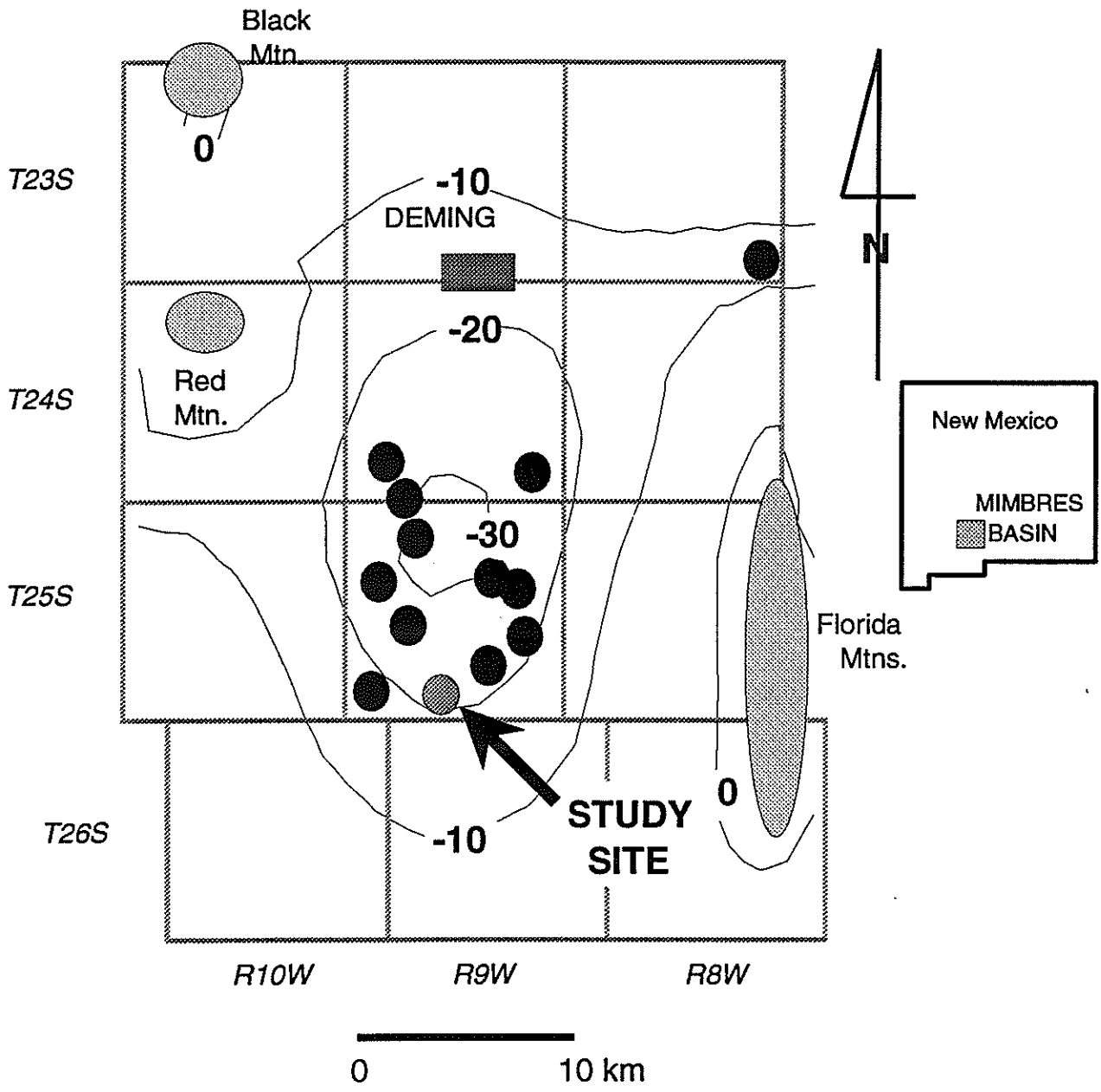

FIGURE 3. Fissure locations (dots), study site (light dot), and groundwater drawdown contours (in meters), 1910-1987. (adapted from Contaldo and Mueller 1991).

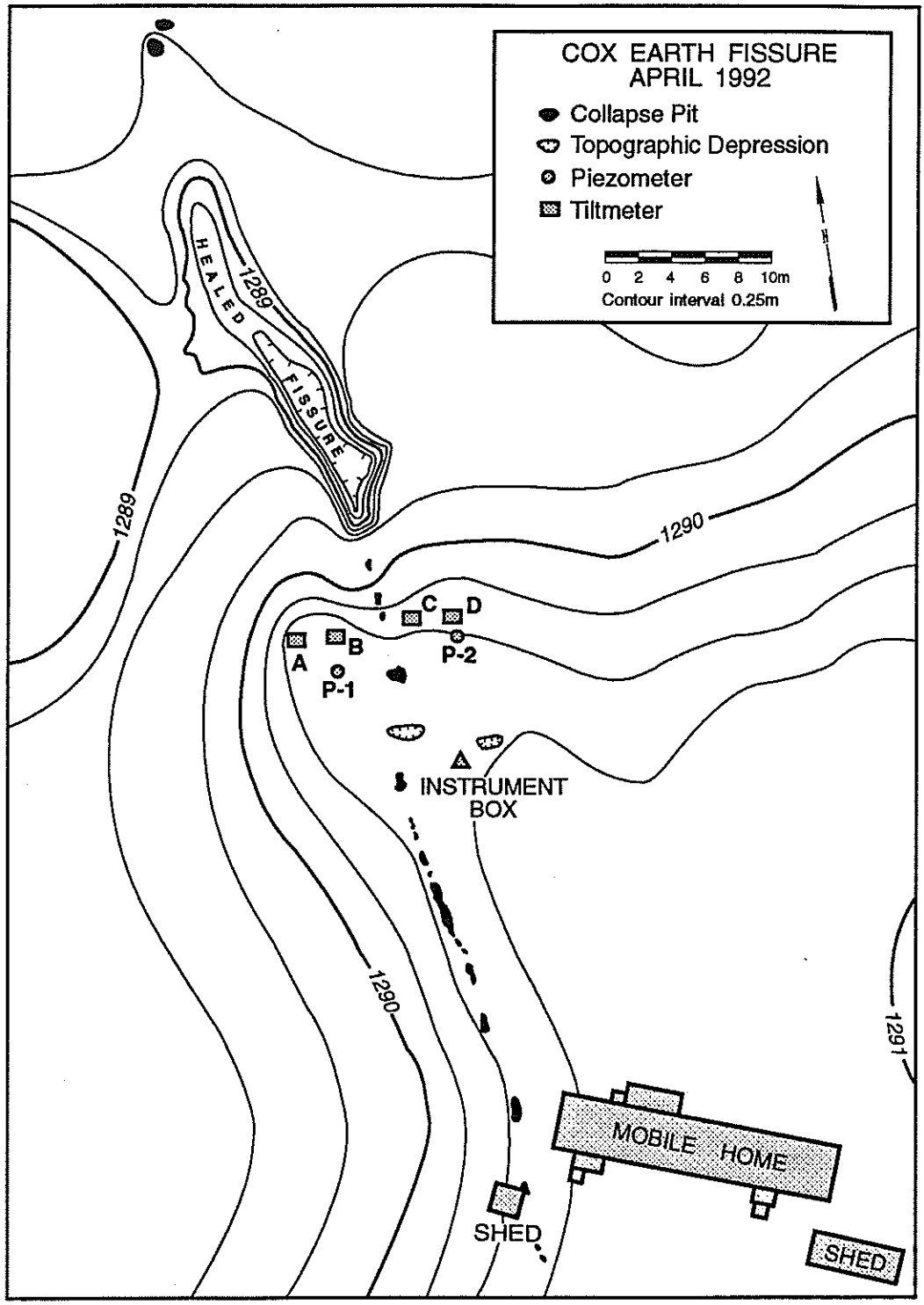

FIGURE 4. Site map showing fissure location and instrumentation layout.

Soils

Surface materials within the basin have been mapped and described by Neher and Buchanan (1980) and by Seager (1992). Within the south-central portion of the basin, Neher and Buchanan (1980) categorize the soils within the Mimbres Association, which consists of well drained soils including some that have been occasionally inundated. These soils are found on bottom land within the broad, central portion of the basin.

At the study site, both Seager (1992) and Neher and Buchanan (1980) describe the soils as associated with alluvial fan deposits of the Mimbres River. The soils are mixtures of gravel, sand, loam, silt, and clay. Seager (1992) separates the soils into two categories: a coarser grained sand and gravel facies of distributary channels that stand about 1 m above the surrounding lowlands, and a fine grain facies of loam, silt, and clay that is found in the interdistributary flats. Both soils grade downward into gravel and sand lenses. The thickness of the soils ranges from 1.5 m to about 7 m (Seager 1992).

Climate and Vegetation

The climate of the southern Mimbres Basin is within the drier portion of the BS (steppe) climate according to the Koeppen system of climate classification (Mueller 1988). Other climate systems along with some variations of the Koeppen system categorize the climate as true desert and Mueller (1988) suggests that the area be regarded as the northern extension of the Chihuahuan Desert.

In the Deming area, the average mean temperature ranges from 5.2° C in January to 26.6° C in July (Mueller 1988). Precipitation averages 23.5 cm per year with the largest portion falling during the period from July to September, during the annual monsoon season. Free surface evaporation averages 180-190 cm annually (Mueller 1988) and evaporation from a Class A pan may reach 277 cm per year (Neher and Buchanan 1980).

Vegetation at the site consists of mesquite, creosote, yucca and various annual weeds and grasses (Neher and Buchanan 1980). The quantity of vegetation varies considerably with the amount of annual precipitation.

Inhabitants

Two people live in the mobile home at the site. The trailer is serviced by a water well, believed to be 64 m deep, adjacent to the southeast corner of the trailer, and a septic tank that is located south of the trailer.

History of Fissure

Much of the information regarding the fissure's development was compiled by Contaldo (1989). The fissure consists of two segments. The southern portion of the north-northeasterly trending fissure, which opened in June 1982 and is 218 m long, was backfilled by ranchers soon after it opened to prevent injury to their cattle. Piping of the backfill material downward to fill subsurface voids led to formation of cracks and aligned potholes that indicate the fissure's location.

The northern fissure segment, which is being monitored, appeared during an intense thunderstorm in October 1984. This segment trends in a north-south direction for a distance of 454 m. The middle portion of the segment lies within the shallow drainage depression north of the mobile home. During the storm, the fissure intercepted all the runoff through the drainage without filling (June Cox 1991, personal communication). Initial measurements indicated that the fissure was about 2.4 m wide and up to 6.7 m deep in this area. To the north of the depression, the fissure consisted of aligned potholes and a small crack 0.6 to 10 cm wide. Between the depression and the topographic rise to the south, the fissure is marked by potholes and a small topographic depression. This zone of the fissure, approximately 15 m long, appears to bridge a right-step offset of approximately 5 m between the fissure expressions on the rise and in the depression (figure 4). On the rise, the fissure was expressed by a crack 0.6 to 12.7 cm wide and up to 4.9 m deep. The fissure trends between the mobile home and an out-building exposing a

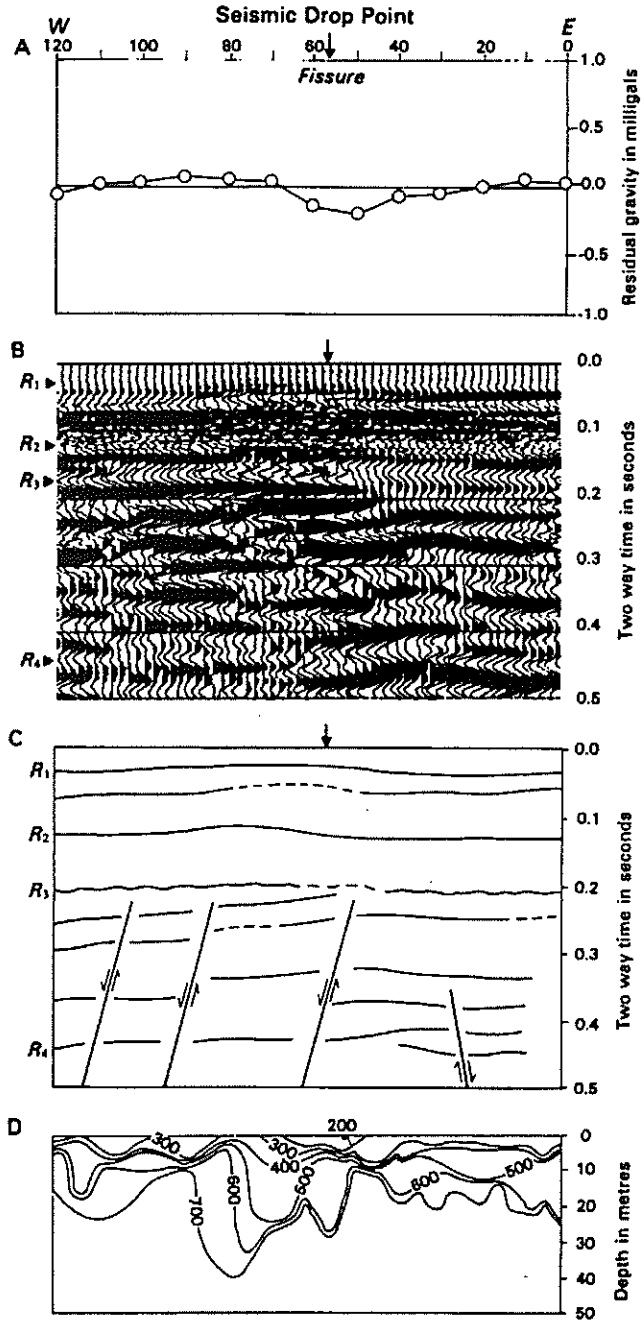

FIGURE 5. Results of geophysical surveys across Deming fissure studied in this report. A) 1st order gravity anomaly. B) Seismic reflection profile. C) Tracing of prominent reflectors with interpreted faults. D) P-wave velocities for uppermost 50 m of the reflection profile. (Haneberg et al. 1991).

sewerline linking the trailer and the septic tank. The fissure continues south of the trailer as a series of potholes aligned along a hairline crack and may link with the southern fissure segment at depth (Contaldo 1989). Since its formation, erosional processes have transformed the fissure into a gully-like feature 8.5 m wide and about 1.5 m deep.

PREVIOUS SEISMIC AND GRAVITY SURVEYS

Shallow seismic reflection and gravity surveys were conducted at the study site by Haneberg et al. (1991). Seismic drop points were established at 10 m intervals along a line, 1500 m long, oriented perpendicular to the trace of the fissure. Gravity readings were taken every at every fifth drop point (50 m) along the seismic line in order to find first-order Bouguer anomalies.

The gravity profile obtained by Haneberg et al. (1991) reveals a small (–0.20 mgal) gravity low about 200 m wide across the fissure (figure 5a). The seismic reflection survey determined that reflectors at the site are fairly continuous above 75 m depth but discontinuous below, leading to the interpretation of several buried down-to-the-west normal faults below an angular disconformity within the basin-fill (figure 5b and c). This disconformity may mark the contact between older and younger basin fill. Additionally, a decrease in arrival times of the uppermost reflector, lying at 10 m depth, indicate a small structural high, which is believed to be a coarse-grained channel-fill deposit with an estimated 2 m of relief, in the area of the fissure. P-wave velocities indicate a low velocity zone beneath the fissure (figure 5d). Velocities this low (<335 m/s) may be a result of highly weathered surface deposits that have been transported downward to fill subsurface voids, zones of reduced compression at depth, or some combination of the two. Based upon the coincident gravity low and structural high, Haneberg et al. (1991) believe that the fissure may have developed in response to differential compaction of sediments draped over a relatively incompressible channel-fill deposit.

PIEZOMETERS

Two piezometers were installed at the study site, one on the west side of the fissure and one on the east. This configuration allowed detection of water level differences across the fissure. A mud rotary rig was used to drill both piezometers and drill cuttings samples were collected at 3 m intervals for later analysis. As drilling proceeded, circulation was lost on both holes but neither hole was completely drained of drilling mud. Circulation was regained after the mud was thickened with additional bentonite. The final depths of piezometers P-1 and P-2 are 49 m and 49.5 m, respectively, with a static water level 42.4 m below the land surface. Following drilling, each piezometer was fitted with 10 cm PVC casing with 0.51 mm perforations over a 6.1 m screened interval. Backfill consisted of a pea gravel pack over the screened interval that was topped by a bentonite seal. Drill cuttings were used to complete the backfill. The piezometers were then developed by repeated bailing for approximately one hour.

Transducers

Each piezometer was fitted with a Druck PDCR 830 submersible pressure transducer with an operating range of 0 to 103 kPa (0 to 10.6 m of water) and a specified accuracy of 0.1% of the total range. Resolution is controlled by the recording device, and in this study is 13 Pa (1.3 mm of water). The transducers were connected by a vented cable to the data recorder, which provides excitation voltage to the transducers. A desiccant at the opening of the vent tube inhibits condensation that otherwise might travel down the vent tube and damage the transducer.

Lithology

Analysis of samples from the piezometer boreholes revealed gravels, sands, silts, and clays in varying proportions throughout both boreholes. Plots, revealing zones with greater proportions of silt and clay or coarse material are found in figure 6 and figure 7 for piezometers P1 and P2 respectively. Both boreholes exhibit similar trends along their lengths with the P1 plots consistently shifted to the left by 10-15%. This is the result of washing P1 samples to remove drilling mud, which also removed naturally occurring silts and clays and left behind a larger percentage of coarser materials.

Near the surface, both holes contained high proportions of light brown clay (figure 6). At a depth of 10 m,

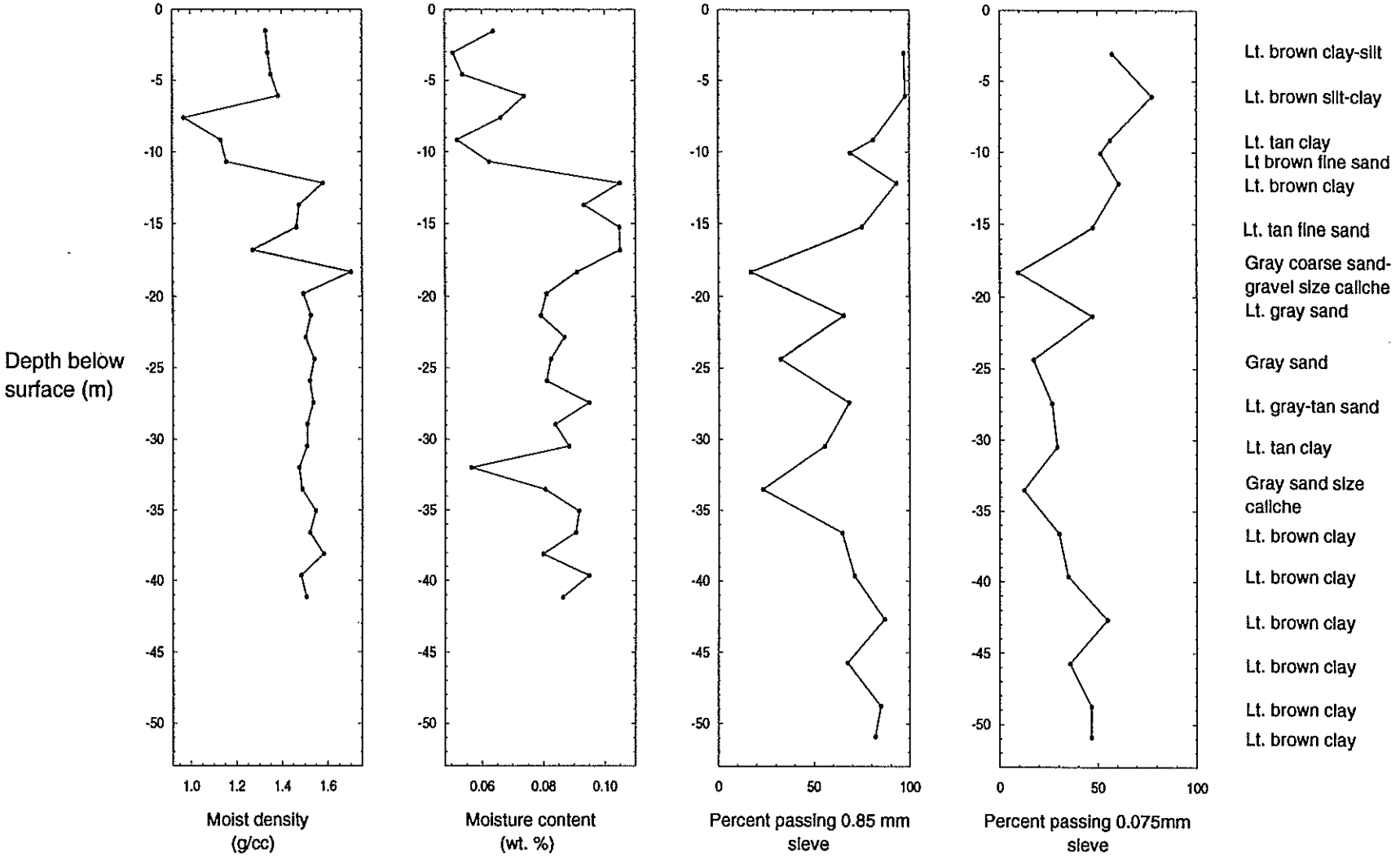

FIGURE 6. Neutron probe, grain size, and lithology data for piezometer P-1.

samples from P1 are coarser, containing fine sand and confirming the interpretation of the seismic reflection survey of Haneberg et al. (1991). Borehole P2 apparently did not intercept this deposit as evidenced by the lack of coarse material recovered (figure 7). Samples from both holes exhibit variable lithologies until 18 m depth where a layer of gray-white coarse sand-gravel size fragments of a caliche zone was encountered. Beneath the caliche lies an interval consisting of mixtures of varying amounts of clay, silt and sand. At 33 m lies another coarse grain caliche layer followed by clay, silt, and sand mixtures to the bottom of the holes.

Neutron Probe Survey

In addition to the grain size analysis, subsurface density and soil moisture contents were measured using a CPN Model 501 Depthprobe (figure 6 and 7). The probe contains a gamma source and detector used for density measurements and a fast neutron source and thermal neutron detector to measure soil moisture content. The probe was lowered down each piezometer with readings taken at 1.5 m intervals. The probe is calibrated for 5 cm diameter casing. The manufacturer was unable to supply the necessary calibration values for 10 cm PVC, but the data do provide information on general trends throughout the soil column and a minimum estimate the density of the surrounding material.

Overall, the neutron probe data suggests a varied soil column with wide ranges of both density and moisture content. Features of note are the presence of a low density, low moisture content zone about 10 m below surface in borehole P1 which coincides with the coarse grained deposit. As with the grain size analysis, the zone appears absent in P2. Also of interest is the region of relatively higher moisture content and density immediately below the coarse deposit which corresponds to a clay rich zone. The coarse grain caliche zone at 18 m depth is marked by high density in P1 and the caliche zone at 33 m depth is noted by decreased moisture contents in both holes.

TILTMETERS

Four Applied Geomechanics Model 722 biaxial borehole tiltmeters are being used to document ongoing deformation near the earth fissure. Each tiltmeter consists of a cylindrical stainless steel body that is 85 cm long and 5.4 cm in diameter. Within each body are two electrolytic sensors, designated X and Y, oriented perpendicular to one another (Applied Geomechanics 1991). The sensors convert changes of tilt angle, referenced to the vertical gravity vector, to changes of resistance that are sensed through an AC half-bridge. Electronics, which were contained on a printed circuit board within the tiltmeter body amplify, actively rectify, and filter AC signals from the sensors to form DC output signals that are proportional to the tilt angle (Applied Geomechanics 1991). The output could then be logged by many types of electronic data-recording devices.

Each tiltmeter includes user-selectable high- and low-gain switches with an optional filter setting. The resolution of each unit at high gain is 0.1 μrad with a calibrated range of ±800 μrad while low gain resolution is 1 μrad over a range of ± 2000 μrad. The filter switch activates one of two, 2-pole Butterworth low-pass filters, each with a different time constant to allow the output signal to stabilize following an instantaneous change in tilt (Applied Geomechanics 1991). A temperature sensor, with a resolution of 0.1 °C, is also included within each tiltmeter.

Each tiltmeter was installed within a 20 cm diamter steel casing that was driven into a pilot hole drilled with an air rotary rig. The driving process ensured adequate coupling of the casing to the surrounding soil materials. Compressed air was forced through a rotating drill bit as it was lowered to the bottom of the hole to clean out the casing. A tiltmeter was then lowered by rope to the bottom of the hole and an amount of #10–20 mesh silica sand, sufficient to hold the tiltmeter in place, was poured into the hole. The tiltmeter was then connected to a power supply and the output monitored by a digital voltmeter while a wedge-shaped tamping tool was used to orient the unit in a vertical position. Tamping continued until the output of both the X and Y channels were within ± 10 mV which ensured that the tiltmeters were in the middle of their measurement range of ±2500 mV. Azimuths of the X and Y axes were recorded for data rotation purposes. Finally, the casing was filled with sand to the top of the tiltmeter, which will enable easy retrieval of the units upon completion of the study. figure 8 is a schematic diagram of a typical installation.

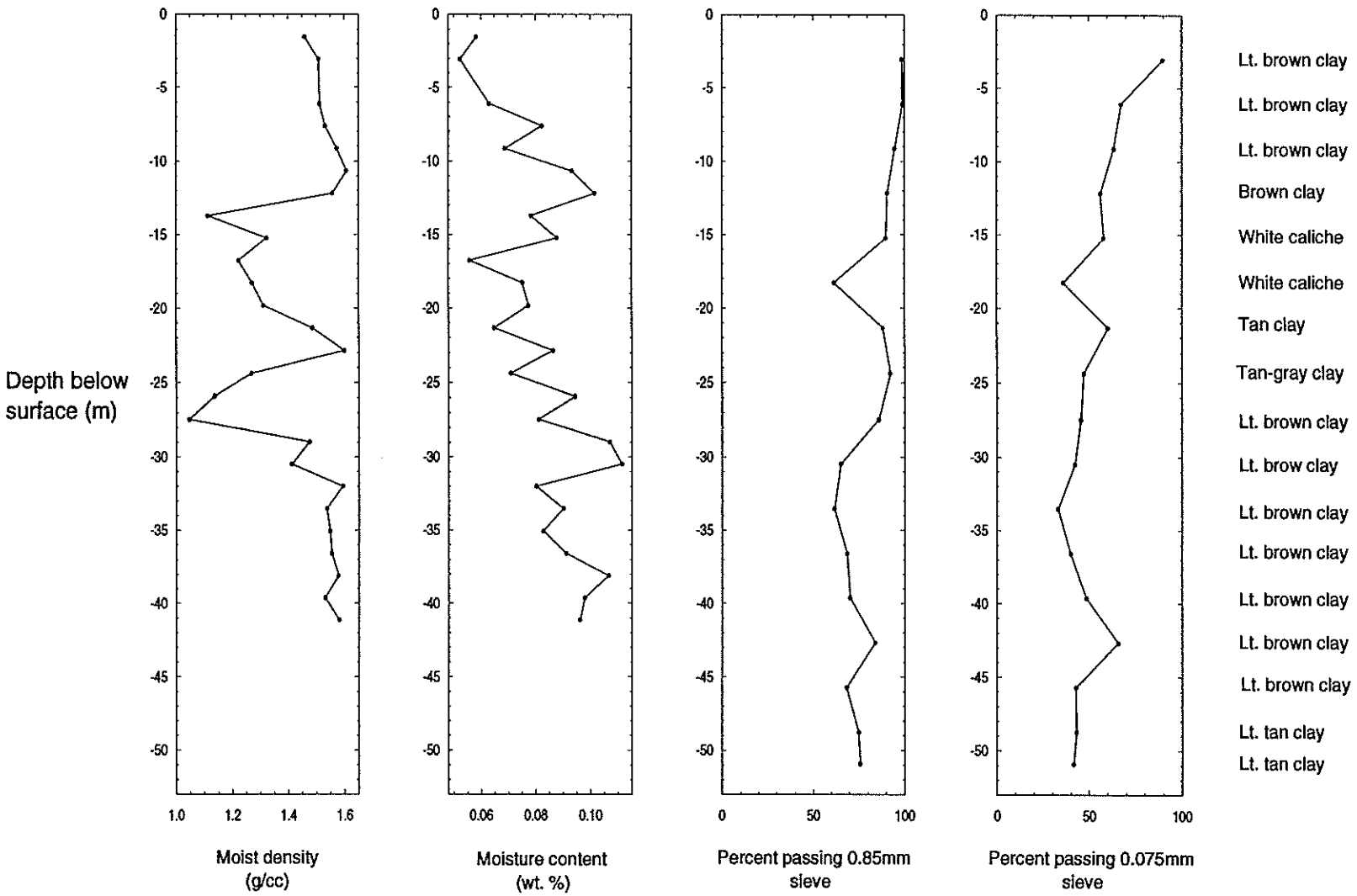

FIGURE 7. Neutron probe, grain size, and lithology data for piezometer P-2.

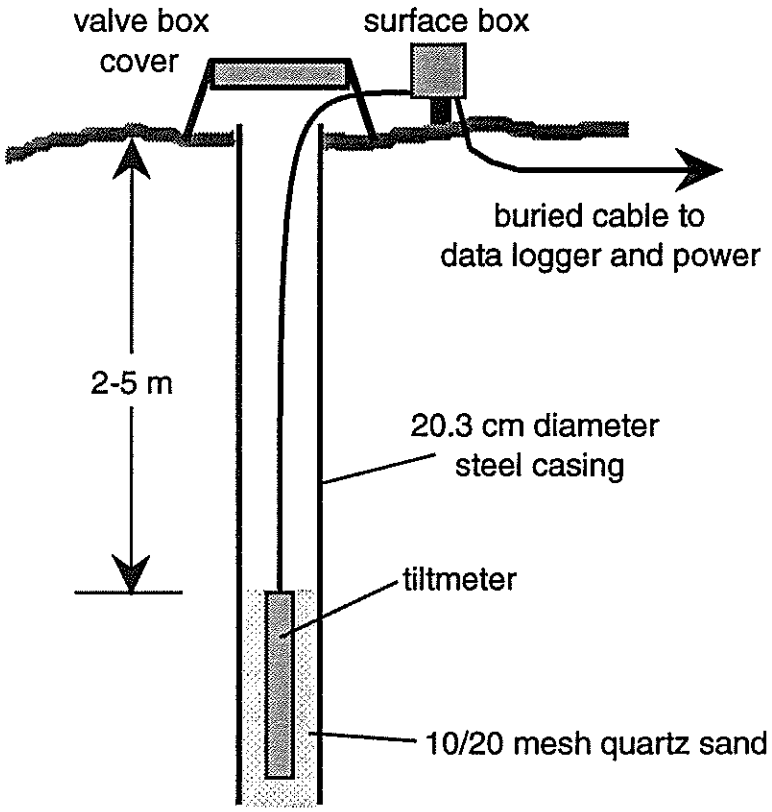

FIGURE 8. Typical tiltmeter installation.

A steel-reinforced cable connects the tiltmeter body to an external switch box which is installed at the surface. The rainproof switch box contains the switches for the tiltmeter's gain and filter settings. Another cable is run from the switch box to the instrumentation cabinet to supply power to the tiltmeter and to carry the DC output signal to the recording device. The cables were buried several centimeters beneath the surface to protect them from weather and cattle which occasionally graze in the area.

The four tiltmeters were installed in a line roughly perpendicular to the trace of the earth fissure and are designated T-A, T-B, T-C, and T-D, respectively, from west to east (figure 4). The depths of the outer units, T-A and T-D, were 2.78 m and 2.70 m respectively while the inner units, T-B and T-C, were at depths of 5.56 m and 6.12 m respectively. The outer instruments were installed at shallower depths after considering models of elastic draping of sediments over rigid bodies which suggest that deformation persists at shallower depths as distance from the fissure increases (Hanneberg, 1992).

DATA COLLECTION SYSTEM

A Campbell Scientific, Inc., CR10 measurement and control module was used to record data at the field site. The CR10 is a user-programmable datalogger/controller which contains 12 analog inputs that may be used as single-ended inputs, or they may be used in pairs for six differential inputs. Three outputs are also incorporated in the unit to supply excitation voltages for various applications. Power is supplied by an external 12 V battery. The CR10 contains 64k bytes of Random Access Memory (RAM) for program and data storage. Monitoring programs are created on a portable PC computer using an editor, provided with the CR10, and are then downloaded to the datalogger via a RS-232 interface. After a period of monitoring, the data are downloaded to the PC and the datalogger reset to resume monitoring operations.

For this study, the number of analog inputs required for the instrumentation exceeded the inputs available on the CR10. Three outputs are needed for each tiltmeter; X-axis, Y-axis and temperature, and four outputs for two differential measurements for each pressure transducer for a total of 20 input channels. An AM416 relay multiplexer from Campbell Scientific, Inc. was used to provide the additional inputs. The AM416 is able to monitor 32 single-ended analog measurements or 16 differential measurements. The unit was powered and controlled by the CR10 which simply monitors one central input on the AM416 that is then sequentially switched into contact with the analog inputs. The system was wired as shown in figure 9. The CR10 datalogger was programmed to query the instruments once each hour. Under these conditions, the CR10 can record about five weeks of data before it will begin overwriting the earliest recorded data.

Power was supplied to the datalogger from a 12V battery which was charged by a Solarex MSX-10L 10 watt solar panel. The solar panel was wired through a Trace Engineering C-30A charge controller. The C-30A has adjustable reconnect and disconnect voltage settings which kept the battery within a desired voltage range and prevented overcharging. A second 12V battery was required to provide a -12V supply to the tiltmeters to enable measurement of tilts in the negative X and Y directions. Very little current was drawn from this battery and, as such, it did not require continuous charging. However, the battery's voltage was monitored and, when necessary, the battery was exchanged with a fresh battery and taken back to the lab for recharging. The instruments were grounded by tying shield wires (and earth ground wiring on the tiltmeters) to a steel rebar driven into the ground next to the instrumentation cabinet.

OBSERVATIONS

PERIOD OF OBSERVATION

Observations at the field site began in December, 1991 and will continue as an ongoings project funded by the New Mexico Bureau of Mines and Mineral Resources. As a result of technical difficulties, however, no data were recovered until January 13, 1992. This report includes only those data collected through September 25, 1992, which are believed to be sufficient to fulfill the stated project goals.

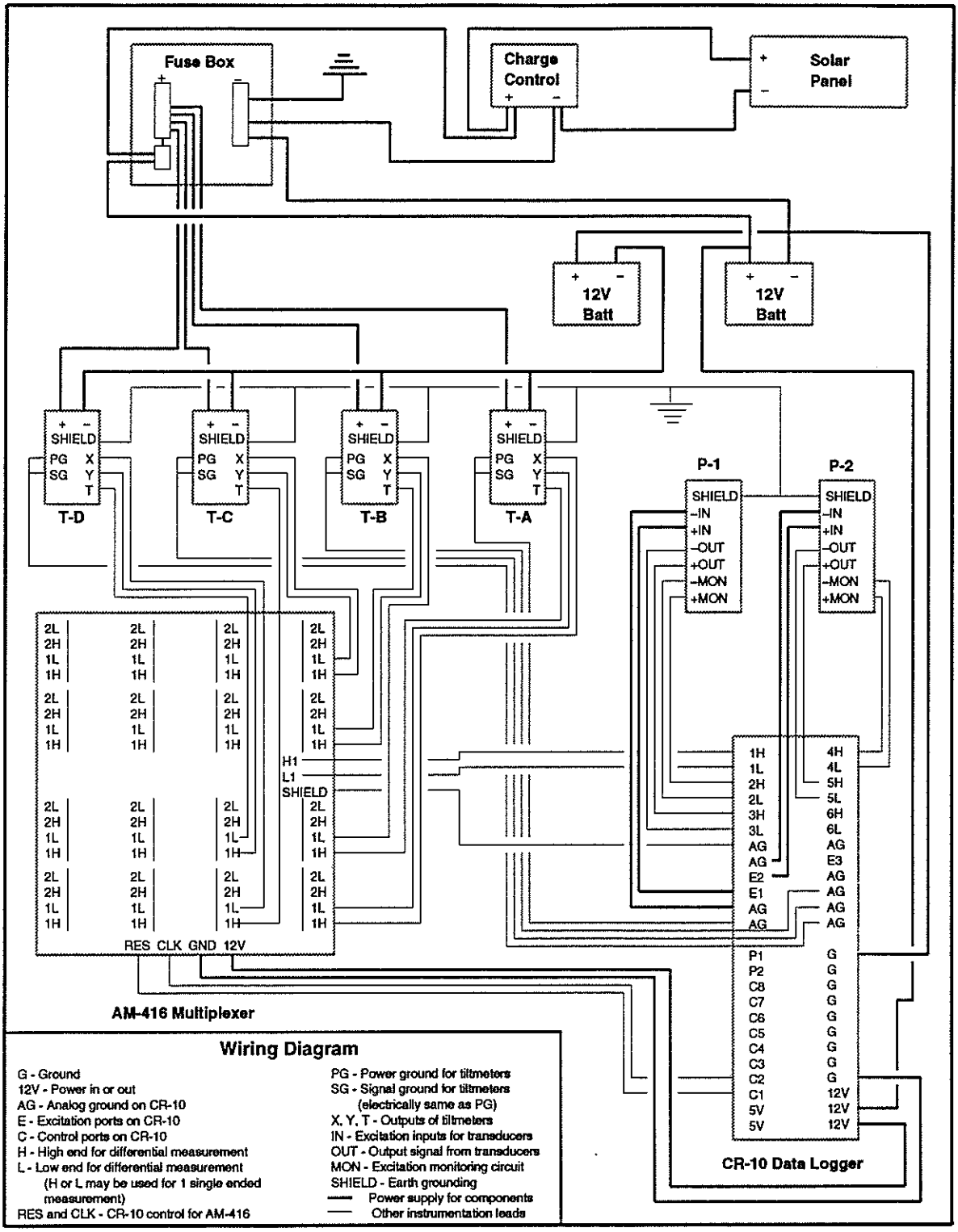

FIGURE 9. Instrumentation wiring diagram.

DATA REDUCTION

The data retrieved from the datalogger were transferred to a computer workstation for analysis. A C-language program was then used to process the original data file by removing output channel numbers and converting millivolt readings into appropriate measurement units of microradians (μrad) for tilt, kilopascals (kPa) for pressure, and degrees centigrade (°C) for temperature. Additionally, tilt readings were rotated to a north-south, east-west coordinate system. The resulting ASCII file was then examined to detect any obvious errors in the data. The errors were easily found by scanning the ASCII file and were even more conspicuous when plotted. Erroneous one-point readings were replaced with zeros. Before plotting or analysis, a subroutine removed any coordinate pair with an inserted zero from the data set.

DATA COLLECTION PROBLEMS

Several difficulties arose as data collection began. The most serious was drainage of the 12V batteries after only a week or two of data collection. Originally, both batteries were tied into the charging system which was thought to be able to maintain the charge. However, after many attempts at various fixes, it was determined that the solar panel could maintain only one 12V battery. The present configuration of charging only one battery with continued monitoring of the second, was adopted and has operated well since the change was made. This problem resulted in many data gaps during the first two months of operation.

Second, problems were experienced with the pressure transducers. Both transducers failed and were returned to the manufacturer for repairs. There, it was found that a small hole had developed in the molding of P1 which allowed water to seep into the unit, rendering it inoperable. The unit was replaced and given the designation P1B. A short was found in P2, causing its malfunction. This unit was also replaced and given the designation P2B. Both units function adequately after being replaced, although questionable readings and trends, with no apparent physical justification, are occasionally noted within the data.

An additional change was made in the way the data logger queries the transducers. This change incorporated a measurement of the actual excitation voltage passed to the transducers from the data logger, in addition to the measurement of output voltage from the transducer. This modification compensated for any small variations of the excitation voltage from the CR10 and increased the accuracy of the reading.

The tiltmeters performed well throughout the study, only occasionally giving obvious spurious data. The only malfunction to date involved T-A, which occurred during maintenance of the system at which time the multiplexer was exposed to the sun for an extended period of time and became quite hot. It is believed that this in some way affected T-A, and lead to erroneous readings. When attempting to correct the malfunction, it was discovered that the instrument was functioning properly so no further action was required. Tiltmeter B was found to have tilted out of its high gain measurement range during the first weeks after installation. This is believed to have been caused by settling of the instrument and sand within the casing. The tiltmeter was nudged back into a vertical orientation with the tamping tool and it continues to operate well. On one occasion, in late June 1992, it was found that the battery providing −12V to the tiltmeters suffered a sudden voltage drop. This resulted in erroneous tilt data being recorded for the last two weeks of the monitoring period (June 19 through July 4). The battery was replaced and the tiltmeters began to function properly once again.

The temperature data from the tiltmeters may be used to determine effects of temperature changes on ground behavior. However, the presence of steel casing, which has a high thermal conductivity, affects the temperature values and may be considerably different from actual soil temperatures.

LONG-TERM RECORDS

Piezometer Records

As a result of the highly fragmented nature of the pressure transducer data, manual measurements of the depth to groundwater were used to examine long-term groundwater fluctuations at the study site. These measurements

were taken with an electronic water level indicator.

The initial water levels were measured in early December 1991, when the static water level was about 42.7 m below the land surface. The aquifer should begin a recovery period during the winter months which lasts until the spring when irrigation pumping resumes, causing a drop in groundwater levels. The change in groundwater levels in the two piezometers and the domestic supply well follow this general trend (figure 10). Records of groundwater level change for all three wells indicate a period of gradual decline, generally 5 cm or less, for the period from December 1991, through February 1992. A short recovery period occurs in March, when groundwater levels rise to the early December level. Then, in late April, groundwater levels fall off in response to increased pumping in the area. The net decline over the period of record is 15-16 cm in each well (figure 10).

Tiltmeter Records

Long-term records for each of the four tiltmeters are displayed in figures 11 through 14. A plan view of the movements of each tiltmeter is shown by plotting the east-west channel versus the north-south channel (figures 15 and 16). Gaps in the records indicate periods of malfunctions which prohibited data collection.

Tiltmeter A began by tilting downward toward the west and then tilting downward in an east-northeasterly direction. Near the end of the data record, T-A traced a loop by tilting toward the west and again, back to the east (figures 11 and 15). Maximum tilt displacement for the unit is 96 μrad for the east-west axis and 49 μrad for the north-south axis.

Small spikes, such as those observed in the y-channel record on Julian days 121 and 205 (figure 11) are believed to be caused by voltage drops when a battery change occurred. It is thought that, after restoring power to the system, the tiltmeters take a period of time to come on line and reestablish the previous readings. The low-pass filter setting probably contributes to this as it filters the large jump in the tilt signal caused by reconnection of the power supply.

The other outer tiltmeter, T-D, generally tilted in an opposite manner to T-A. First, T-D began by tilting downward toward the northeast before turning back toward the south and gradually tilting downward in a southwesterly direction (figure 15). The rate of tilting increased during early summer, which can be seen by comparing the relative movement in the six month period before June 16 with the movement in the three month period after June 16 (figure 15). The east-west channel remained within a relatively narrow range until early June, after which larger tilts downward to the west were recorded (figure 14). The maximum change in tilt over the data record is 189 μrad along the east-west axis and 150 μrad along the north-south axis. Also evident are small, short-term daily fluctuations (figure 15).

Tilting of T-B is also complicated and illustrates various cycles of deformation. This unit tilted downward in a north-northeasterly direction before tilting downward toward the southeast (figure 16). Again, relatively rapid tilting was recorded during the period from July 4 through September 25, with the unit tracing semicircular patterns superimposed upon a long-term southeasterly trend. Total east-west tilt during the period is 59 μrad with the unit tilting 61 μrad in the north-south direction. Small daily fluctuations can also be seen in the data record along with a small spikes in the y-channel record on Julian days 115 and 121 (figure 12).

Tiltmeter C traced a broad arc during the observation period. Between January and June, the unit tilted first down toward the west and then tilted down toward the north (figure 16). In July, T-C began tilting downward in a northeasterly direction and finally tilted downward in an easterly direction for the final two months of the data record. The change in tilt over the record is 105 μrad along the east-west axis and 135 μrad along the north-south axis.

Long-term records for the four tiltmeters are summarized in a series of five schematic diagrams (figure 17). This figure illustrates, again, the large variation in both tilt direction and magnitude for the different units over the course of the study. Generally, the two outer tiltmeter records have a component of tilt inward, toward the fissure, for all periods except for the January record. During this time, the units tilt downard away from the fissure. The inner tiltmeters have some component towards each other, except for the late July and September records. In late July, T-B and T-C tilt in approximately opposite directions, while in September, T-C tilts away from T-B.

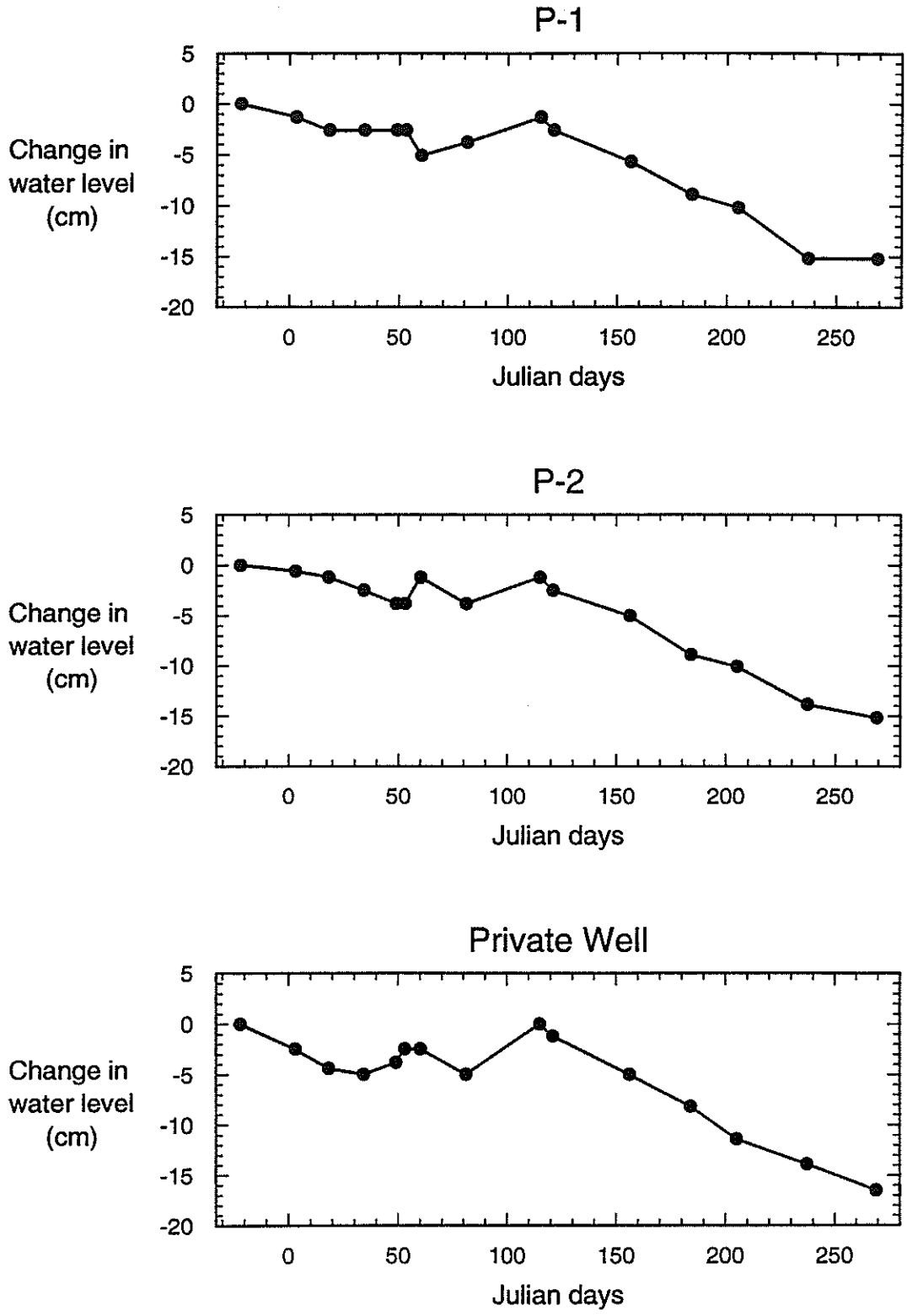

FIGURE 10. Groundwater level fluctuations at study site (December 10, 1991 – September 25, 1992).

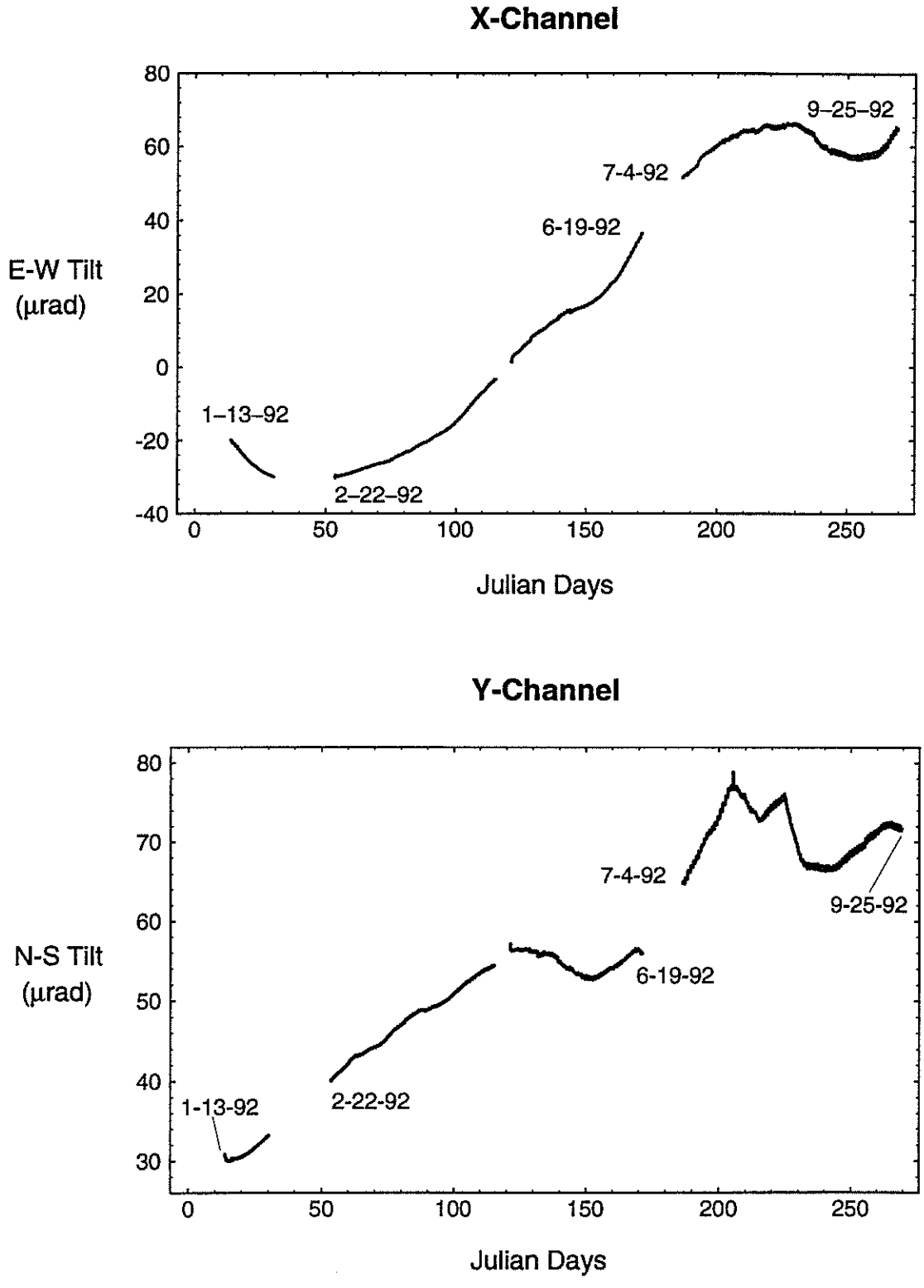

FIGURE 11. Long-term tilt records for Tiltmeter A (east and north - positive, south and west - negative).

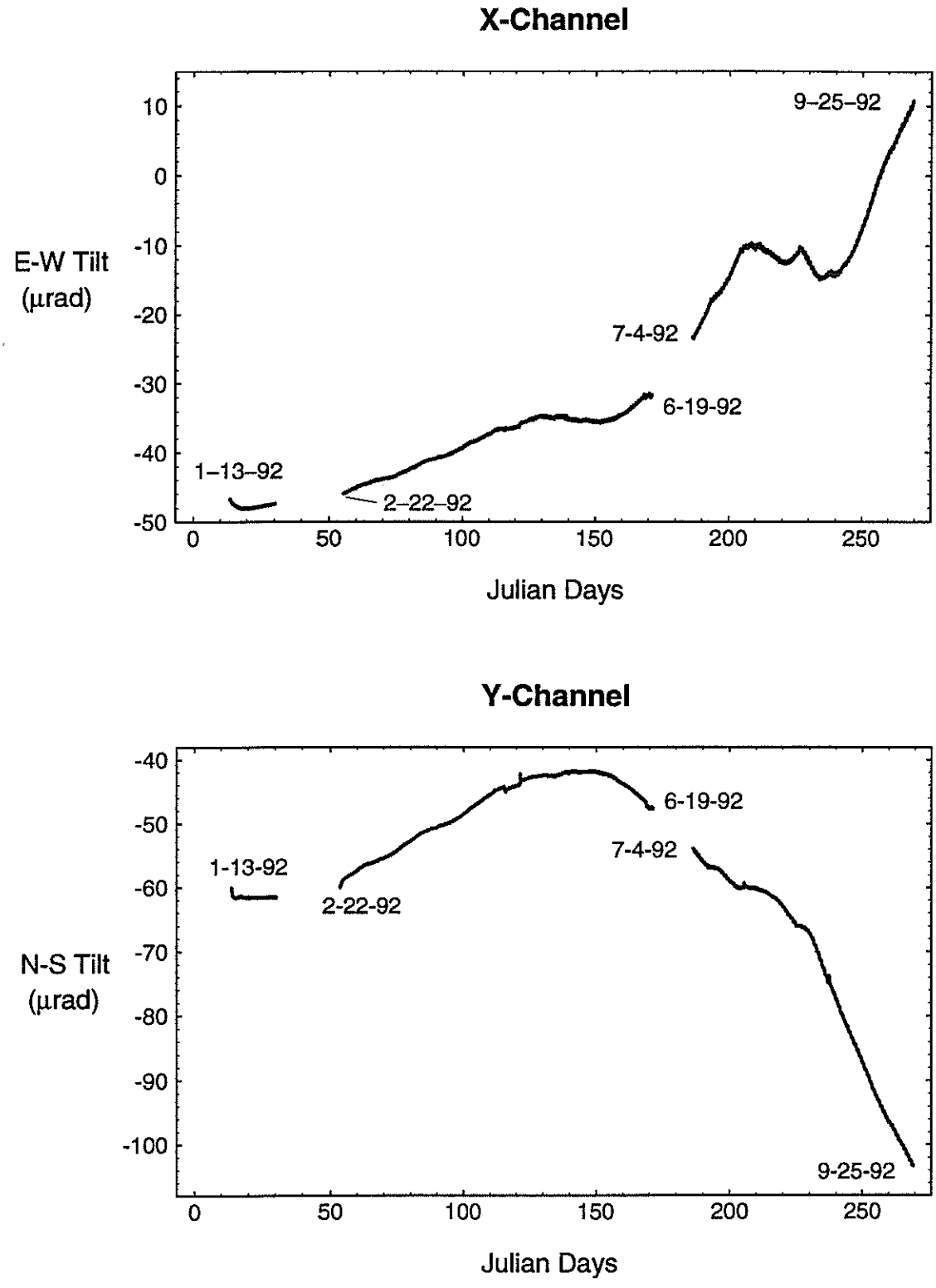

FIGURE 12. Long-term tilt records for Tiltmeter B (east and north - positive, south and west - negative).

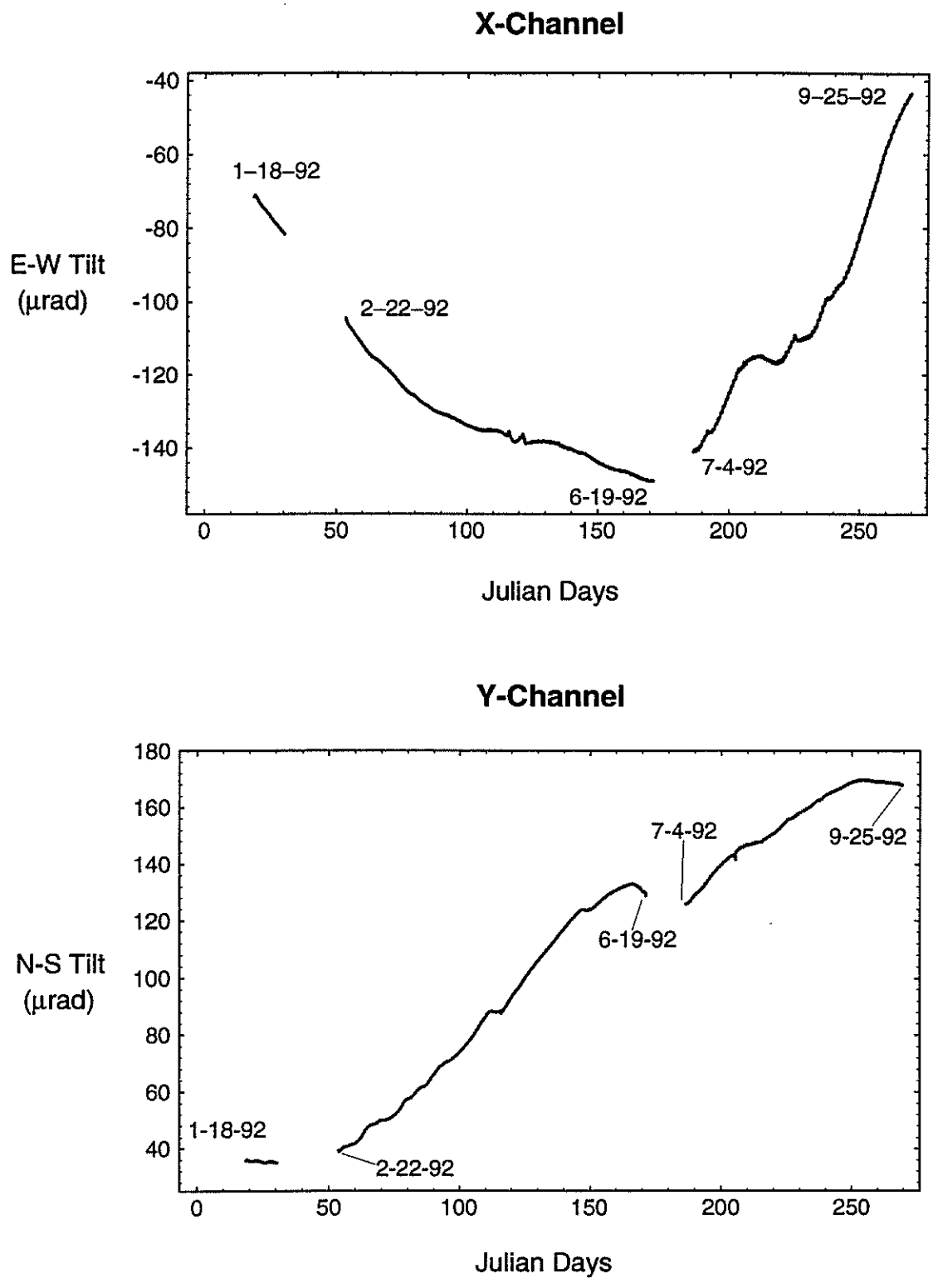

FIGURE 13. Long-term tilt records for Tiltmeter C (east and north - positive, south and west - negative).

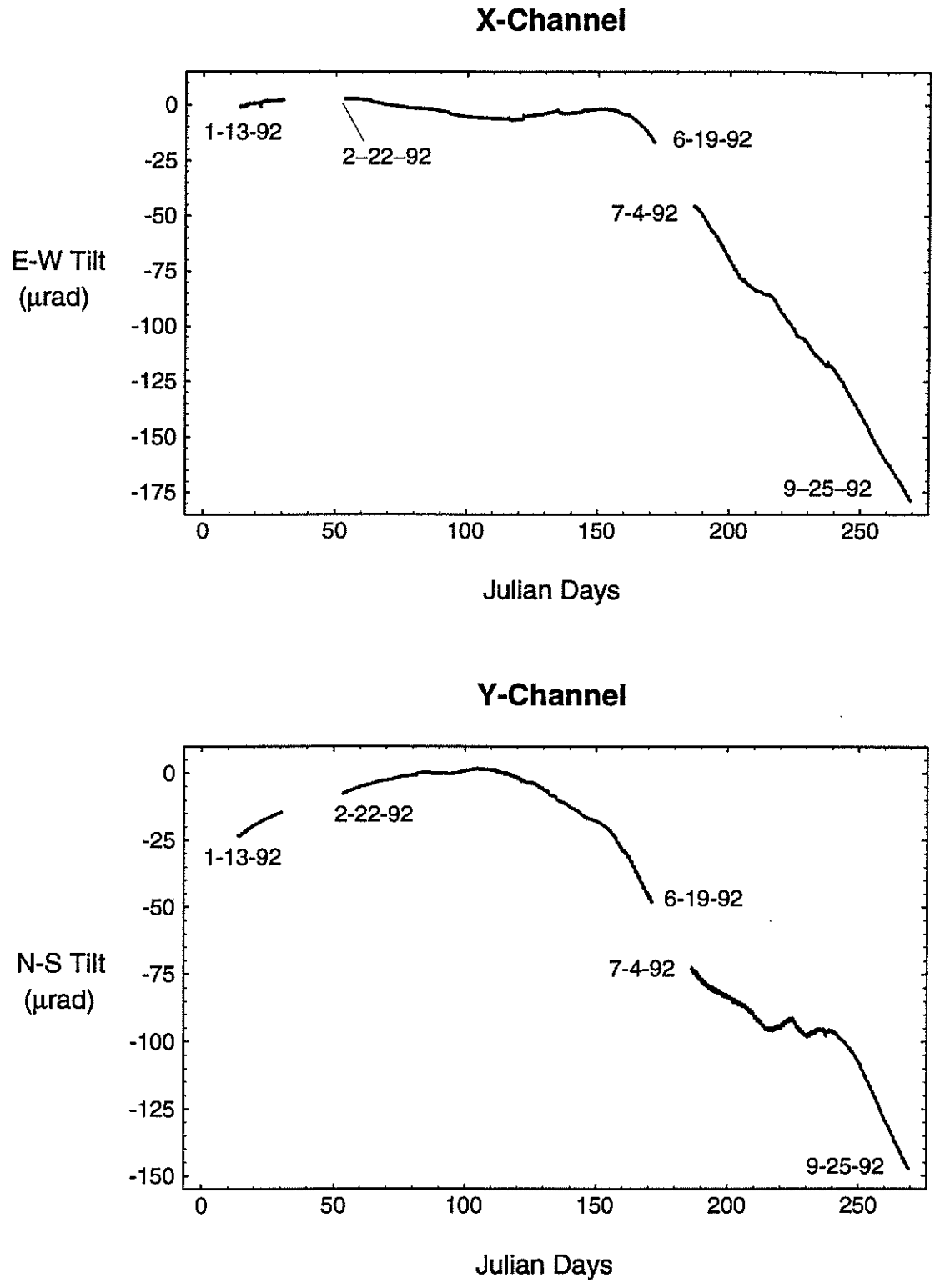

FIGURE 14. Long-term tilt records for Tiltmeter D (east and north - positive, south and west - negative).

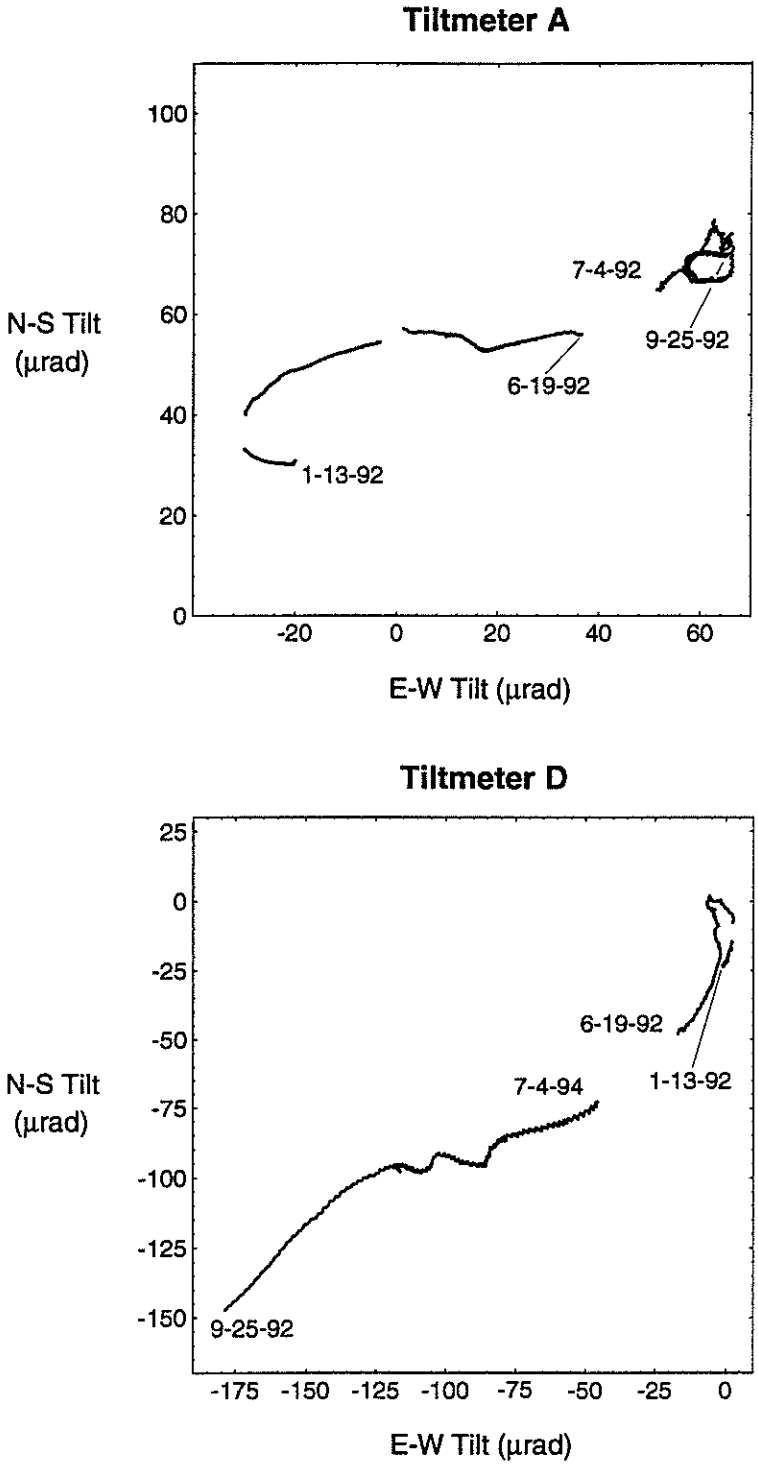

FIGURE 15. Plan view of tilt movements for outer tiltmeter stations(east and north - positive, south and west - negative).

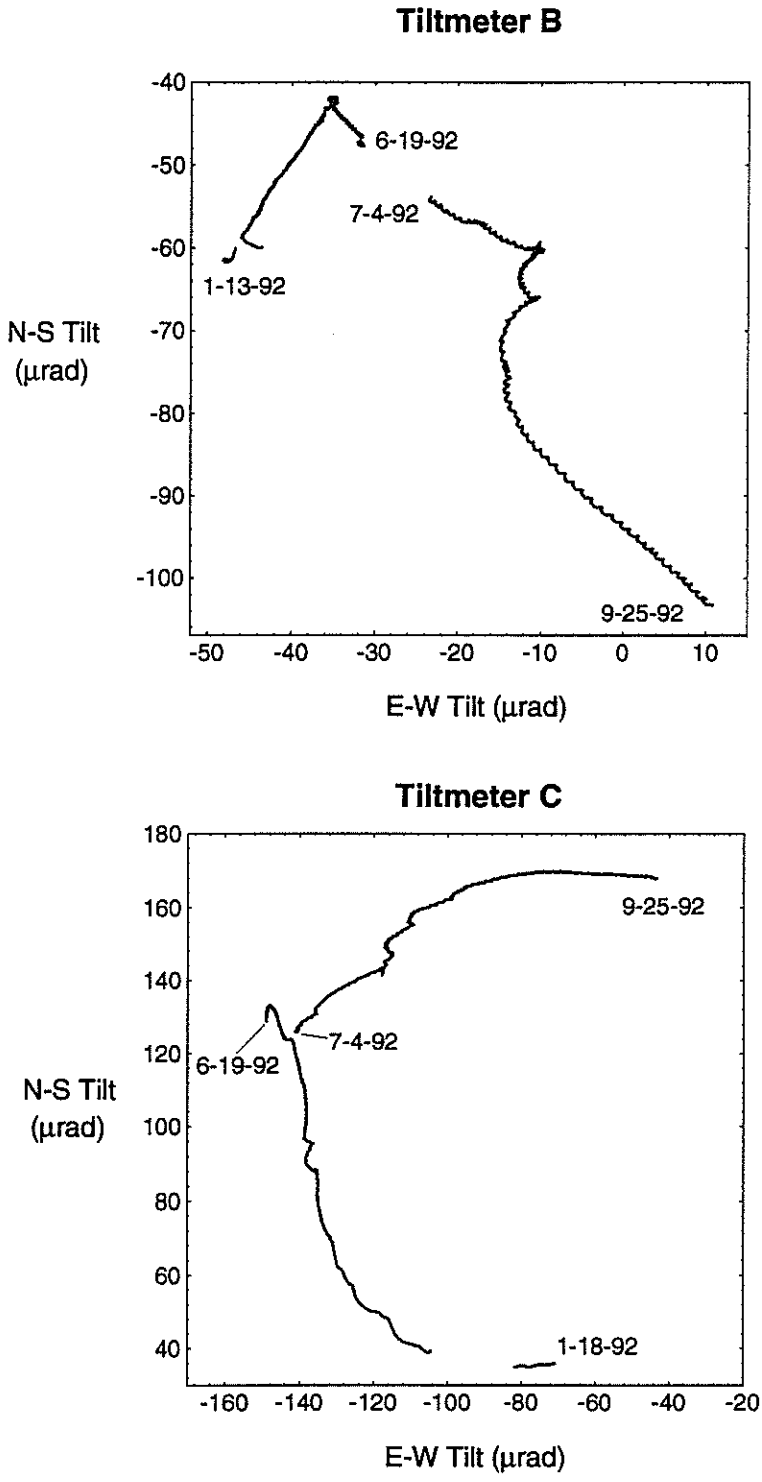

FIGURE 16. Plan view of tilt movements for inner tiltmeter stations (east and north - positive, south and west - negative).

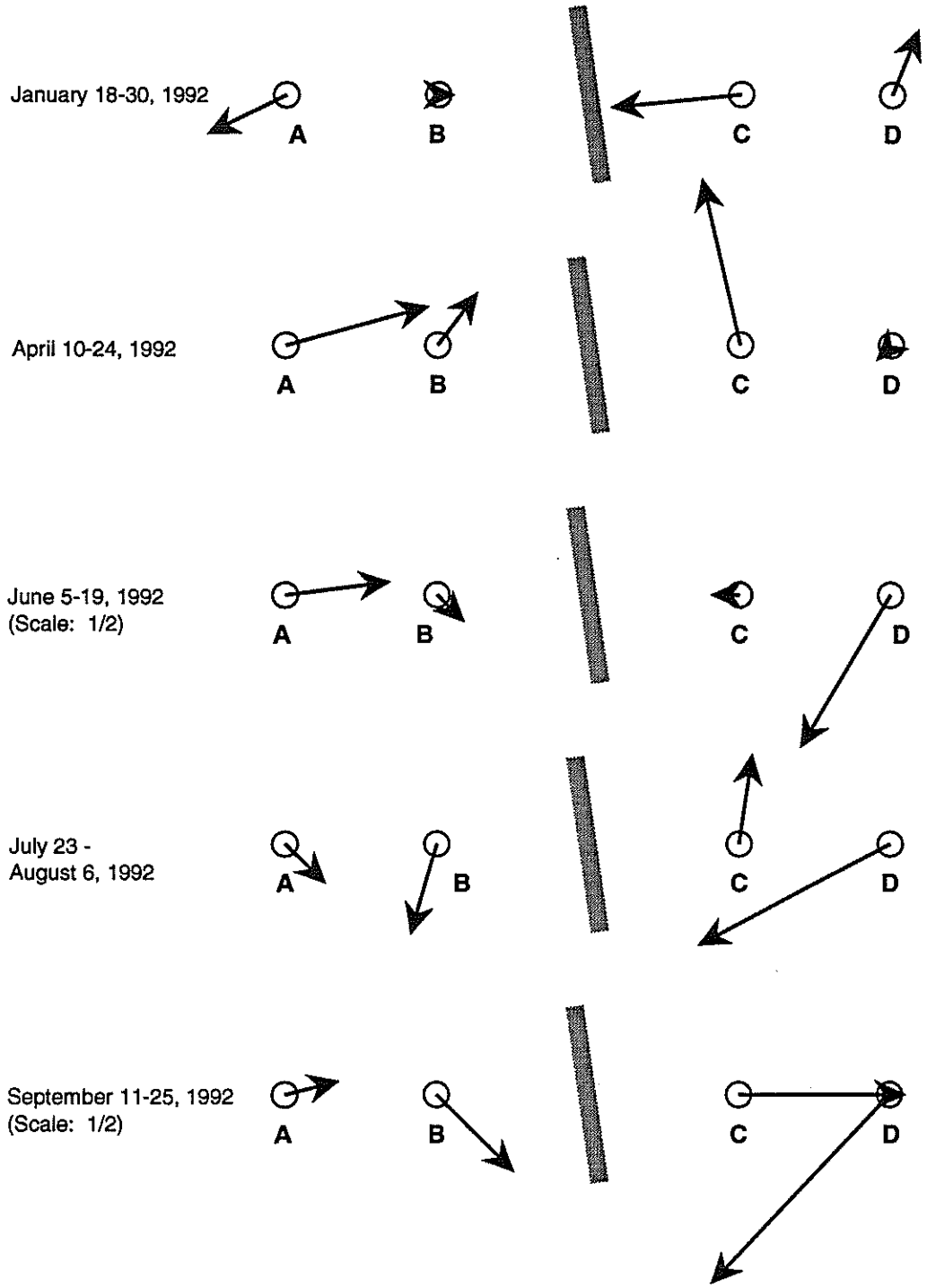

FIGURE 17. Schematic diagrams of tilt movements for five, two week data sets. Lengths of arrow denote magnitude of tilt (June and September records magnitudes are reduced by one-half). Gray strips represent fissure.

Overall, the April and June records suggest that the fissure is closing as the units tilt toward the fissure. These records correspond to the period of steepest water level decline (figure 10). The January record is somewhat inconclusive as T-A and T-D tilt away from the fissure while T-B and T-C tilt towards the fissure. During late July, T-B and T-C tilt away from the fissure while T-A and T-D tilt toward the fissure. It is interesting to note that the orientations of tilt for the outer units versus the inner units reversed between January, when the water table was more or less stable, and July, when heavy pumping of the aquifer was taking place. In September, the fissure also appears to be closing, however, the behavior of T-C and T-D, tilting in such different directions is somewhat puzzling.

SHORT-TERM RECORDS

Piezometer Records

Pressure transducers produce a good picture of groundwater fluctuations for data records of several days in length. All the data exhibit similar trends; therefore, a single five day record from September 14-18 (Julian days 258-262) was chosen to illustrate the changes observed (figure 18). The most striking feature of the water level records is a diurnal cycle with a high groundwater peak in the afternoon along with a smaller peak in the early morning. The magnitude of the fluctuations is on the order of 3 cm per day. Longer-term trends, such as declines due to extensive pumping, take considerable time to reach the magnitude of the daily fluctuations. An approximate drop of 15 cm over a period from April 24 to September 25 (150 days) gives an average drop of 1 cm per 10 days, while the daily fluctuations are 30 times as great.

Tiltmeter Records

Short-term records of the tilt channels exhibit similar patterns, although they vary in direction and magnitude of movement. Examples are shown from the data record used for short-term water level fluctuations, September 14-18 (figure 19). Daily fluctuations are apparent, but these fluctuations are superimposed upon stronger long-term trends. The magnitude of both the daily fluctuations and the span covered during the five day period, varies among the tiltmeters. The daily fluctuations range from 0.6 to 1.8 μrad while, over the five day record, the tilt change ranged from 1 to 11.5 μrad. Also of interest is the absence of an intermediate peak seen in the groundwater level records. Other tiltmeter records occasionally display an this peak, but it is usually less prominent than that seen in the piezometer records.

TILT-WATER LEVEL CORRELATION

Long-term tilt data obtained during this study do not correlate well with water level data. Scatter plots of tilt versus water level, which were produced as part of the data analysis process but not included in this report, did not indicate any unambiguous trends for periods when transducer data are available. This is probably because tilt data are dominated by long-term trends whereas groundwater records are dominated by larger daily fluctuations. Plots of tilt versus hand-measured water levels suggest a weak relationship between tilt and decreasing water level. As above, however, the relationship is ambiguous and further analyses are needed.

Short-term scatter plots of tilt versus water level indicate a weak correlation in some cases. Some tilt channels show a moderate trend while others display little or no trend at all. Additionally, examination of records from different periods during the study show channels that exhibit some correlation at one time may show no correlation, or an opposite sense of correlation, at other times. There is an association between short-term water level and tilt peaks. As seen in figure 20, the highest water level peak in a day commonly corresponds to a tiltmeter peak or trough. This is caused by the additive effects of various harmonic components within the signal that happen to be in phase once each day. The components are generally out of phase throughout the rest of the 24 hour period, resulting in a noisier signal and making it difficult to pick out any correlation during water level troughs. The data record displayed in figure 20 is one of the better examples of this association. Other records are not as well defined. These patterns seem to suggest that the fissure closes as the water level increases, which agrees with the simple draping model in a general sense.

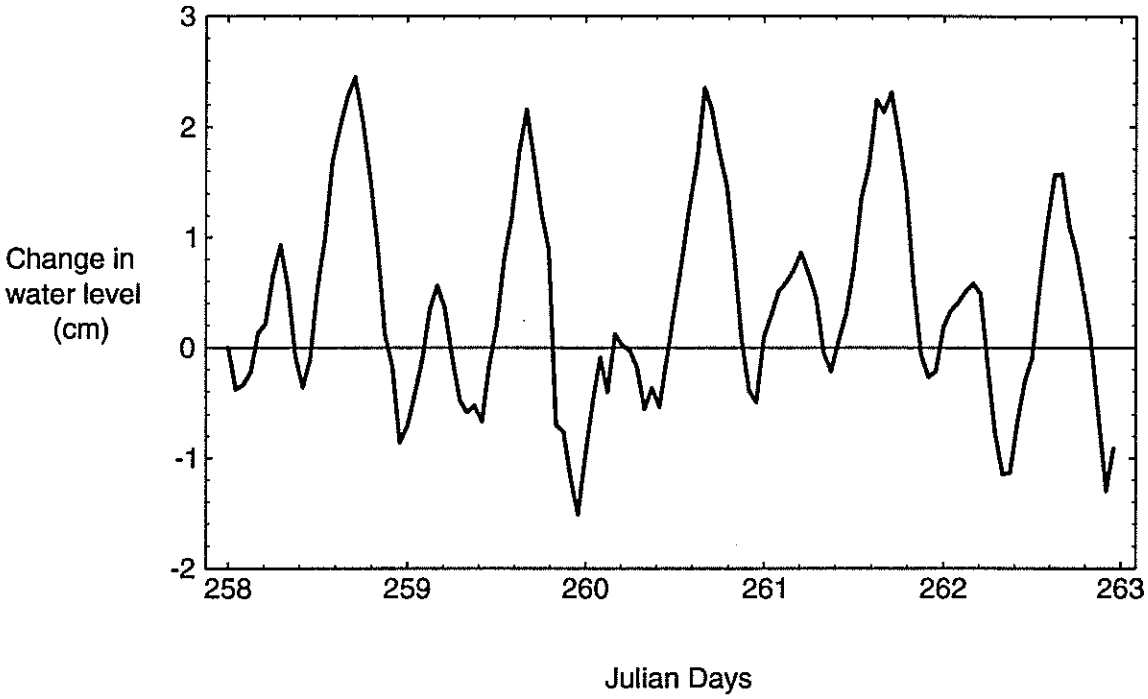

FIGURE 18. Short-term groundwater level fluctuations in piezometer P-1 (September 14-18, 1992).

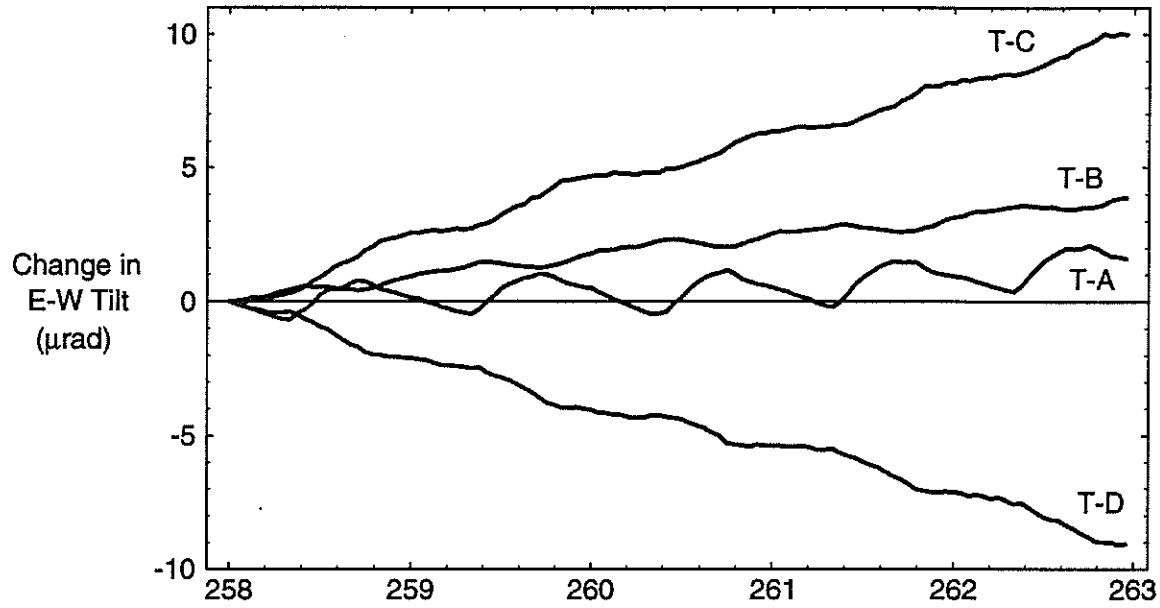

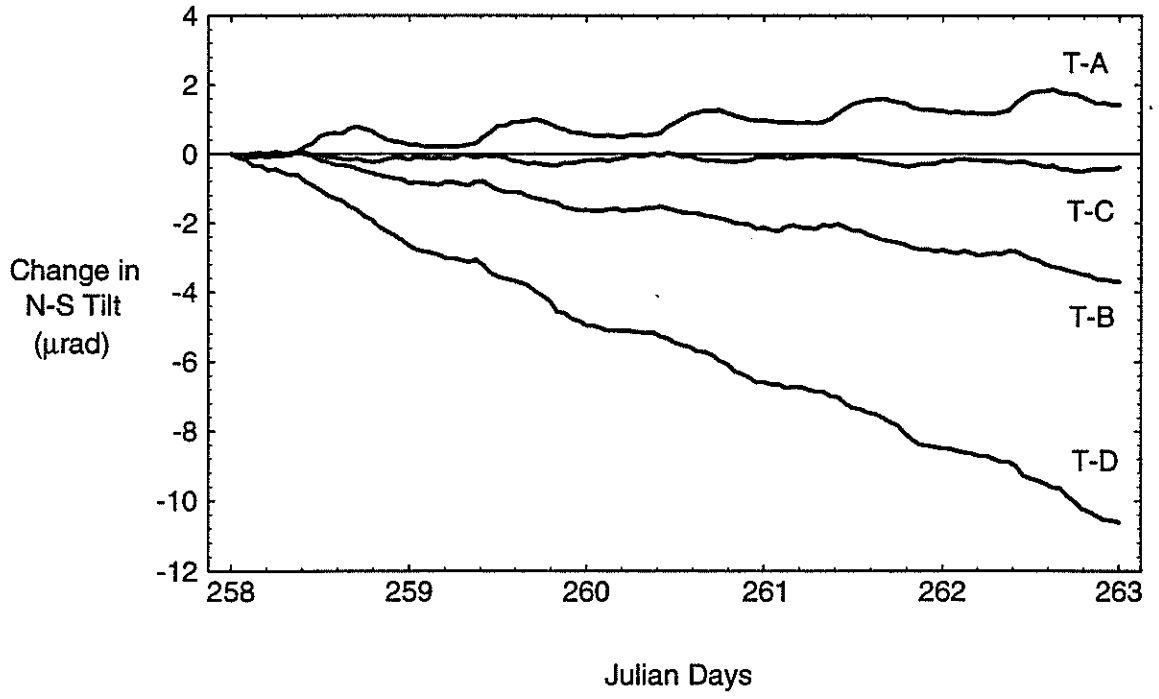

FIGURE 19. Short-term tiltmeter records (September 14-18, 1992).

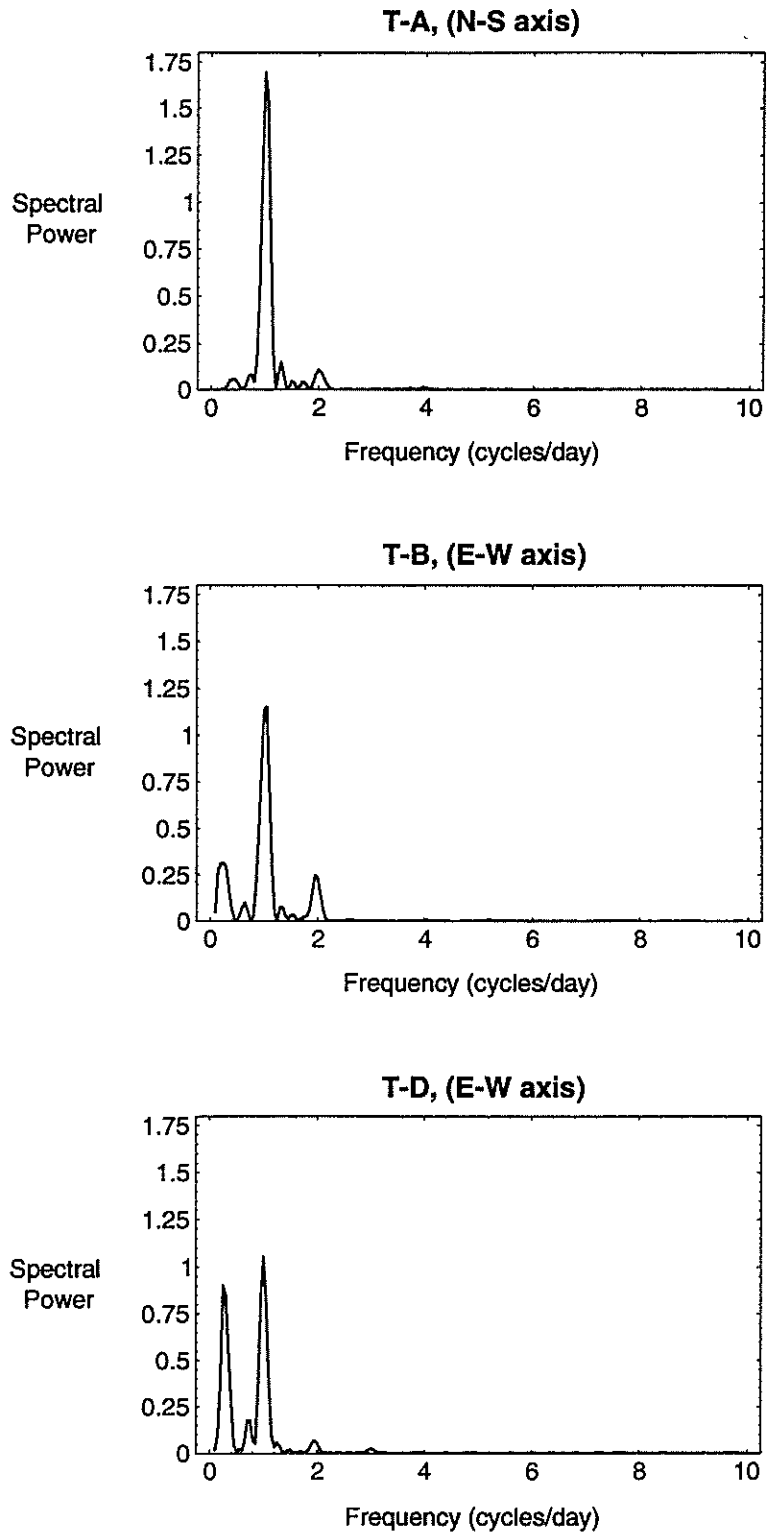

FIGURE 20. Spectral power analysis of three, short-term tiltmeter records (September 14-18, 1992).

HARMONIC ANALYSIS

In an attempt to more precisely determine periodicities present within the data, and to gain insight into the forces at work at the study site, an analysis of the harmonic components within the data was performed. This analysis consisted of two exercises: 1) examine the power spectra to establish the dominant periodicities that may be present in the data and, 2) utilize known, physically reasonable cycles in a fitting exercise to attempt to duplicate the data record.

Power Spectra

Computers make it possible to search a string of data using hundreds or thousands of frequencies in an attempt to find periodicities within data. The results are often displayed in the form of a plot of the strength or power of each periodic component versus the spectrum of trial periodicities. This type of analysis is often carried out with the application of Fast Fourier Transform (FFT) methods. However, FFT methods require that the data be sampled at evenly spaced intervals (Press and Teukolsky 1988). This is not the case in this study because of voltage drops, instrumentation malfunctions, and erroneous data points. FFT methods weights the data on a "per time interval" basis which, with unevenly sampled data, can lead to large errors such as a bulge of power at low frequencies (Press and Teukolsky, 1988).

An alternative method is to estimate the power spectra by use of periodogram analysis (Lomb, 1976; Scargle, 1982). Periodogram analysis weights the data on a per point basis that eliminates the errors associated with FFT methods (Press and Teukolsky 1988). Additionally, Lomb (1976) illustrates that periodogram analysis provides a good approximation to the power spectra by using linear least-squares methods to fit a series of sine and cosine curves to the data using the following model:

$$h(t) = A\sin(\omega t) + B\cos(\omega t) \qquad (1)$$

where $h(t)$ is the computed waveform, ω is the frequency and A and B are the least-squares fit coefficients (Press and Teukolsky, 1988). For each fitted frequency, the spectral power (s) is calculated by

$$s = A^2 + B^2 \qquad (2)$$

(Hamming, 1986). When the spectral power is plotted versus the range of fitted frequencies, a large peak indicates that the frequency may be present within the data. However, it is important to note that this method cannot definitively prove that a frequency is present in the data. It only indicates that the periodic component provides a good fit to the data.

Spectral analysis was performed on both tiltmeter and water level data. In order to look at short-term cycles (high frequency periodicities) several five day records were examined. Because tilt records are dominated by long-term trends, a best fit line was first calculated for the data to subtract out this bias. Failure to do this results in large powers in the low frequency range of the spectrum. A subroutine was created to fit sine and cosine curves for a range of frequencies, and to calculate the resulting power of each frequency.

Plots of the power spectra are shown for three tilt channels from the data record September 14-18 (figure 21). Evident in all three plots is the dominant peak corresponding to a 24 hour cycle. Additionally, another peak occurs with a cycle of about 4 days. This peak is quite strong in the T-D east-west record, much weaker in the T-B east-west record and nonexistent in the T-A north-south record. Finally, a weak 12 hour cycle can be detected in all three data sets. However, the 12 hour cycle is often more prominent in other data records as illustrated in the record from May 29-June 2 (figure 22).

The power spectra of short-term piezometer records reveals strong peaks corresponding to 12 and 24 hour cycles (figure 23). All data segments examined exhibit similar spectra.

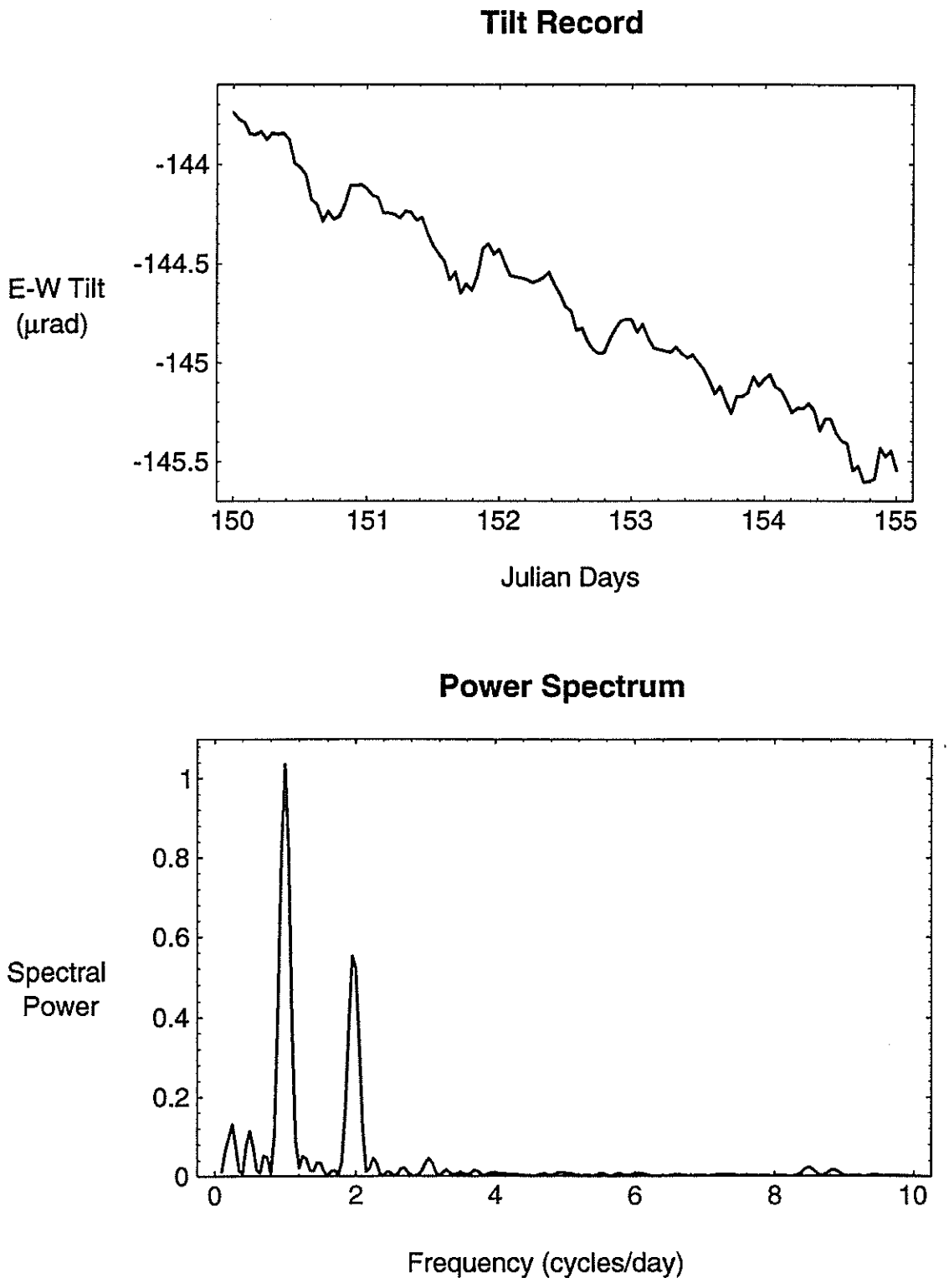

FIGURE 21. Tiltmeter C data and spectral power analysis from May 29 - June 2, 1992,to display power of 12-hour cycle.

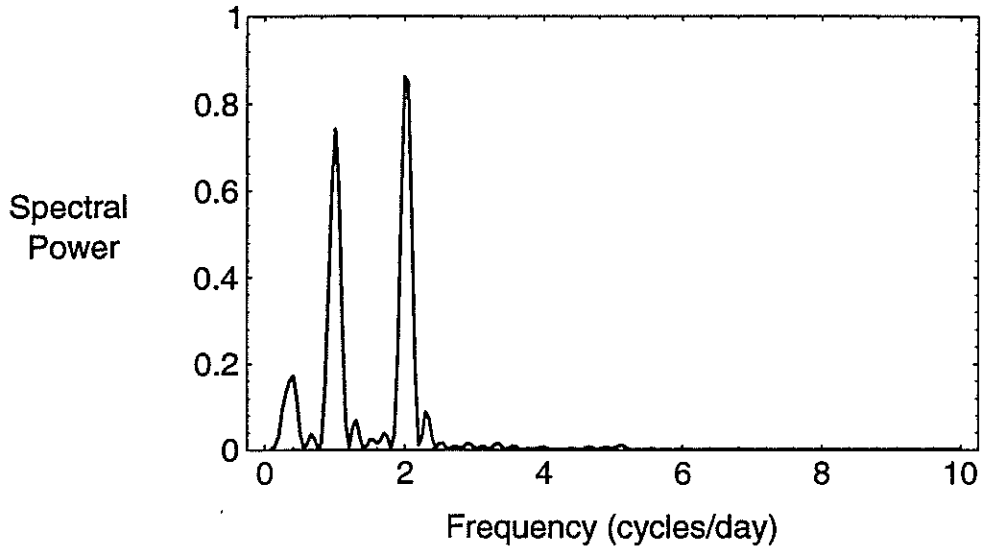

FIGURE 22. Spectral power analysis of P-1 short-term groundwater level fluctuations (September 14-18, 1992).

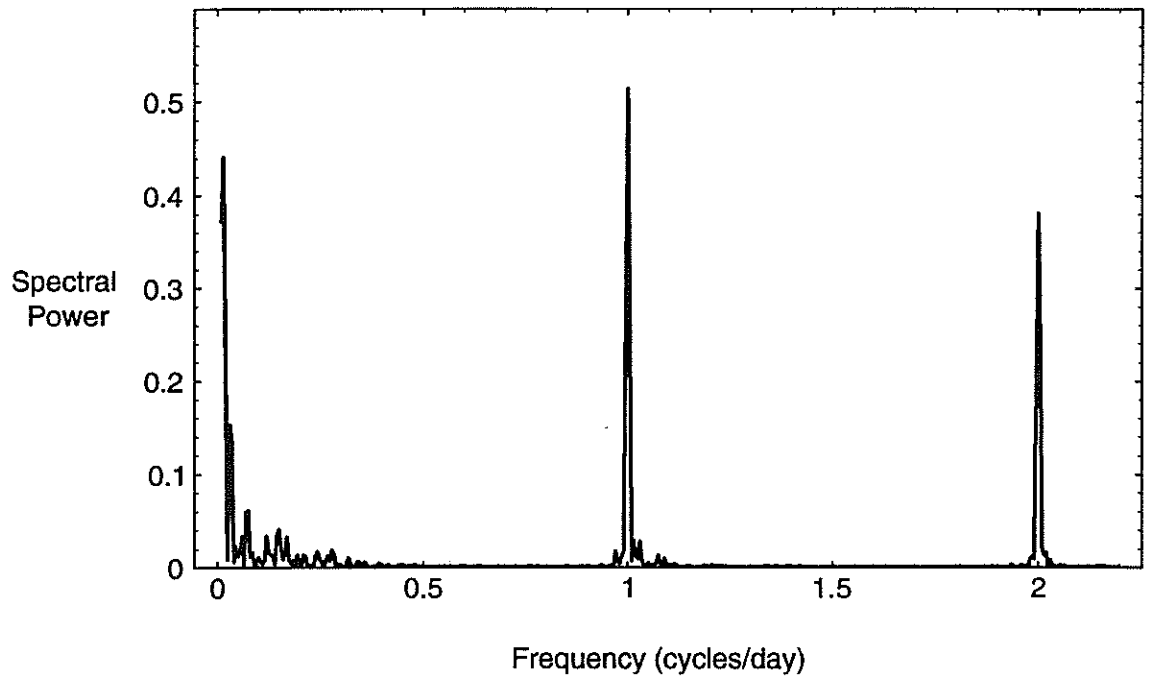

FIGURE 23. Spectral analysis of long-term groundwater level fluctuations measured in piezometer P-1 (July 4 - August 24, 1992).

Analysis of tilt records of more than a few days in length reveals little about the presence of longer-term periodicities. When the power spectrum is plotted, only one large peak, at the extreme low frequency end of the spectrum, is seen. This is believed to be a result of the dominance of long-term trends in the tiltmeter signal. This characteristic could also be the result of aliasing, a common condition in spectral analysis caused by a leakage of power from high frequencies to much lower frequencies (Scargle 1982). However, this condition is most severe when data are very evenly sampled, and it is diminished by uneven sampling (Scargle 1982). It is not known if aliasing is a factor in the predominance of low frequency peaks seen in the long-term analysis.

Long-term piezometer power spectra display a pattern similar to the short-term spectra which is caused by the dominance of diurnal fluctuations within the data (figure 24). However, there is also a peak with a period of about 66 days. The cause of this peak, which is seen regularly in long-term piezometer records, is unknown but may be the result of aliasing.

Selective Fitting of Known Frequencies

After examining portions of the data, a few harmonic components were selected to attempt to duplicate the observed data. These components were selected after considering both the cyclicity of the data and physically reasonable phenomenon that could affect such behavior.

A total of nine harmonics were used to formulate the curve to fit the data. The first term is a linear monotonic trend whose basis is the long-term drop in groundwater levels (Contaldo 1989). The remaining terms are sinusoidal cycles with a variety of periodicities. A 365 day period was used to account for yearly irrigation cycles. The possibility of earth tides prompted the use of periods spanning 27.321 days (lunar) and 13.66 days (half-lunar) (Melchior 1966). The remaining cycles are on the order of 12 and 24 hours and account for 95% of the earth tidal potential (Bredehoeft 1967). These are: 25h 49m 10s, lunar declinational wave; 23h 56m 4s, sidereal day; 12h 39m 30s, lunar wave (caused by the eccentricity of orbit); 12h 25m 14s, lunar wave; and 12h 00m 00s, solar day (Bredehoeft 1967). The components were incorporated into the equation:

$$
\begin{aligned}
y_{pred} = xt &+ A_1\sin(2\pi t/0.50) + B_1\cos(2\pi t / 0.50) + \\
&A_2\sin(2\pi t/0.517) + B_2\cos(2\pi t/0.517) + \\
&A_3\sin(2\pi t/0.527) + B_3\cos(2\pi t/0.527) + \\
&A_4\sin(2\pi t/0.997) + B_4\cos(2\pi t/0.997) + \\
&A_5\sin(2\pi t/1.076) + B_5\cos(2\pi t/1.076) + \\
&A_6\sin(2pt/13.66) + B_6\cos(2\pi t/13.66) + \\
&A_7\sin(2\pi t/27.321) + B_7\cos(2\pi t/27.321) + \\
&A_8\sin(2\pi t/365) + A_8\sin(2\pi t/365) \qquad (3)
\end{aligned}
$$

where y_{pred} is the equation of the calculated best fit curve, x represents the monotonic term, the denominators are the sinusoidal periodicities in days, and A and B are the coefficients for each term. The use of harmonics, with periodicities longer than the span of data, is an arguable procedure. However, the purpose of the curve fitting is not to predict future trends, but only to attempt to determine the various processes at work at the study site by utilizing cycles that have a physical justification.

Fitting equation 3 to short-term records of tilt and water level data produced a very close fit to the observed data (figures 25 and 26). The goodness of fit (r^2) is quite high for both tilt ($r^2 = 0.999$) and water level data ($r^2 = 0.941$). When the fitted curve is subtracted from the observed data, the resulting residual curve is normally distributed about zero with no other harmonic cycles apparent. Again, the high goodness of fit does not prove that the listed periodicities are present in the data; it only indicates that the curve produced by the fit is not very different from the data record.

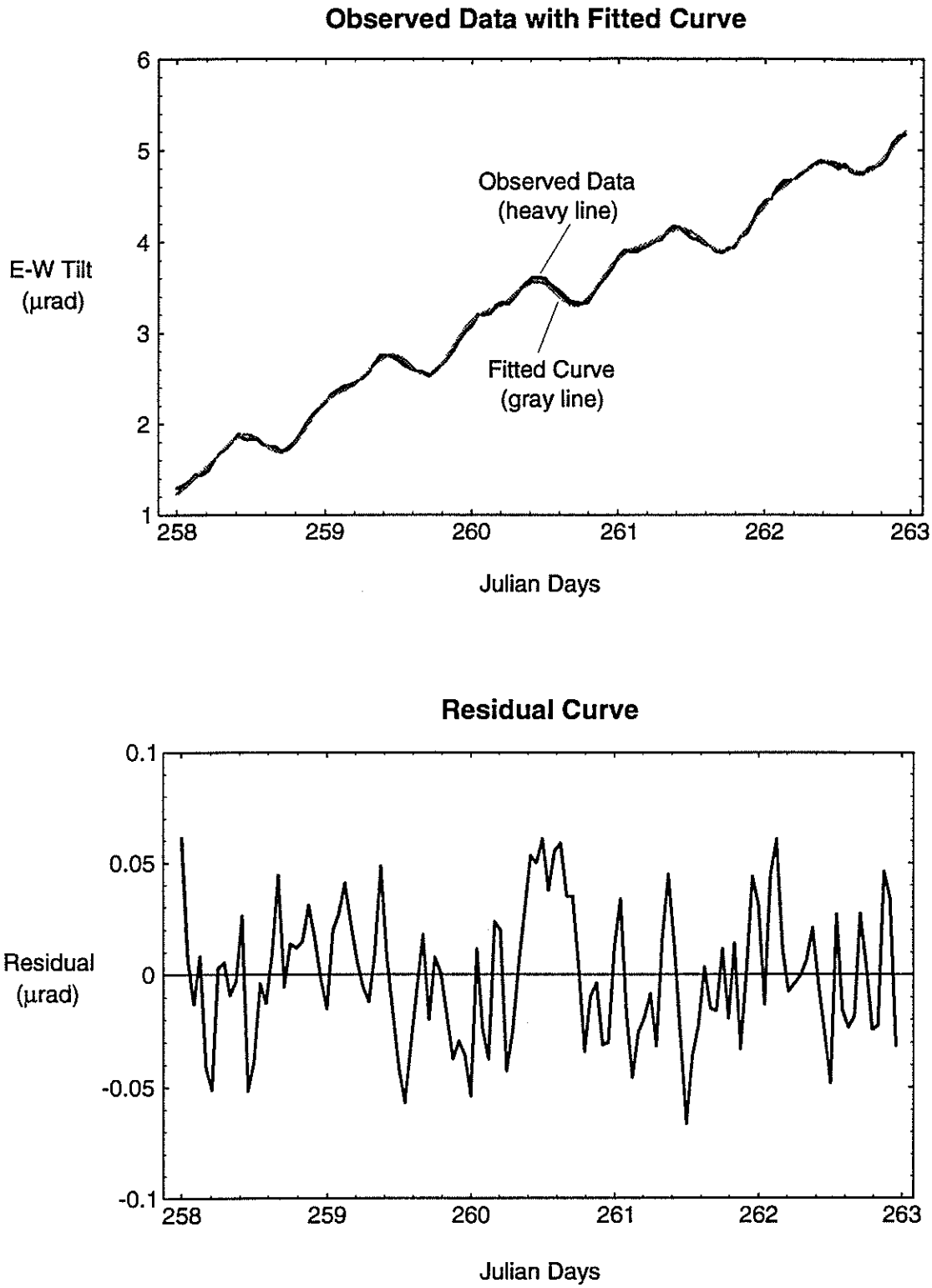

FIGURE 24. Tiltmeter B, east-west data, and best fit line for short-term record. Goodness of fit for this example is $r^2 = 0.999$ (September 14-18, 1992).

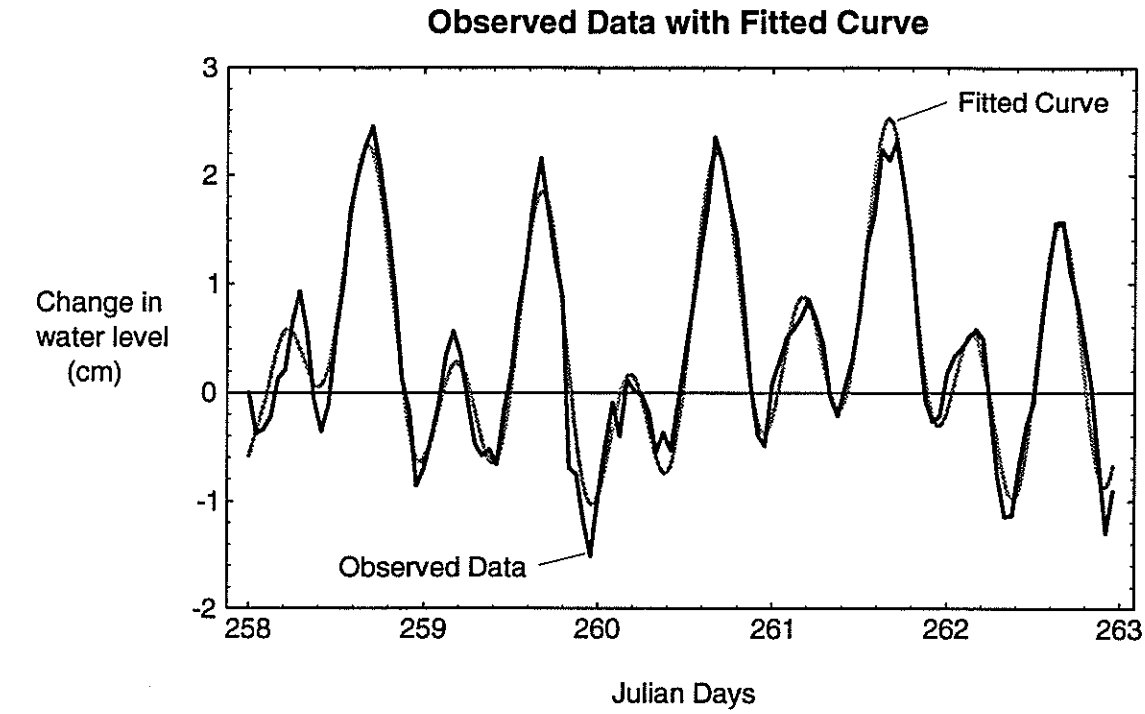

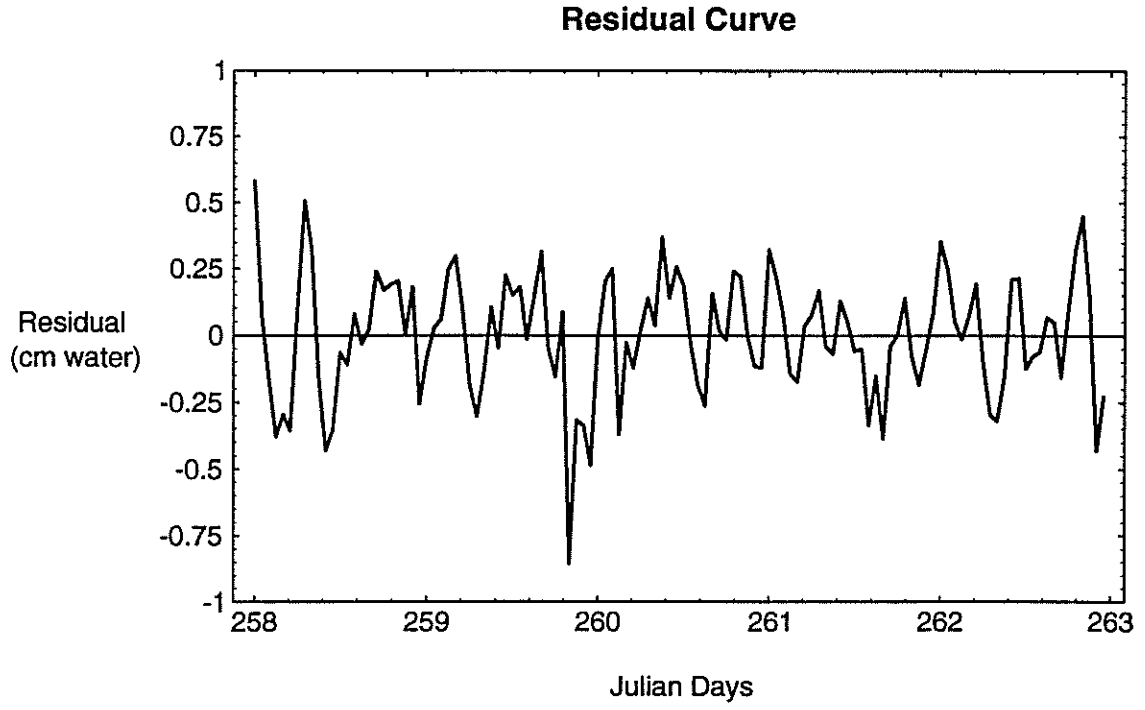

FIGURE 25. P-1 groundwater level fluctuations and best fit line for short-term record. Goodness of fit for this example is $r^2 = 0.941$ (September 14-18, 1992).

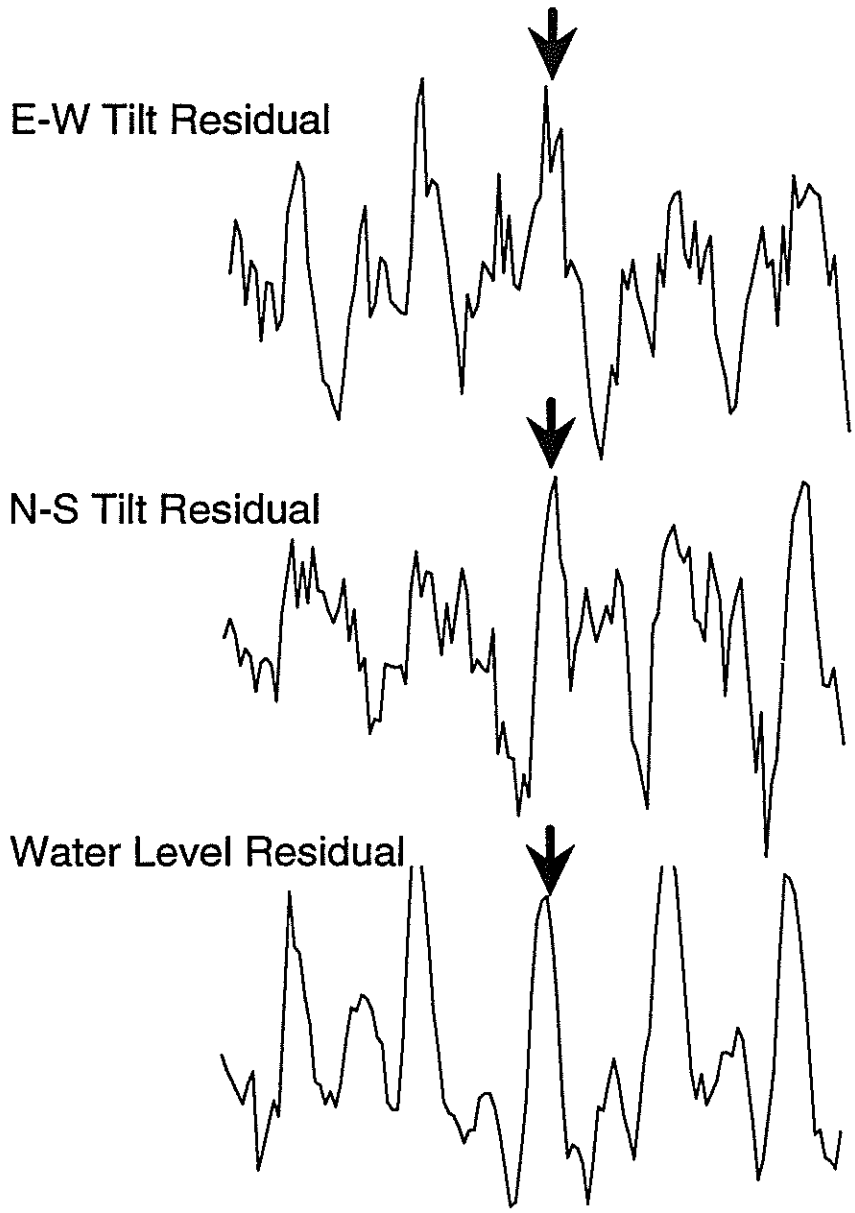

FIGURE 26. Comparison of tilt and water-level peaks for tiltmeter B, January 25-30, 1992. Scales have been removed to facilitate visual comparison of the waveforms, and linear trends have been subtracted from each record via linear regression. Daily water level peaks correspond closely to daily tilt peaks; however, both the relationships between secondary daily water level peaks and tilt and the relationship between water level troughs and tilt are unclear.

SURFACE DEFORMATION ABOVE A COMPACTING AQUIFER: INFERENCES FROM ELASTIC PLATE THEORY

BACKGROUND

Field observations described in previous sections suggest that plane strain models of elastic draping (e.g., Haneberg 1992, 1993) are inadequate representations of deformation around the earth fissure described in this report. The patterns of tilting described previously in this report suggest a more complicated pattern of deformation near the fissure, which may be more understandable when viewed in terms of basin-wide deformation. The clustering of earth fissures near the center of the Mimbres Basin poses a related enigma: classical models of earth fissure formation due to the effects of differential compaction (e.g., Holzer 1984) suggest that fissures should be concentrated along basin margins, where bedrock knobs and buried fault scarps are shallow and basin-fill cover is thin. Concave-downward draping over these irregularities has been inferred to give rise to tensile stresses at the Earth's surface and, consequently, fissuring in several locations (Holzer 1984). Conversely, one would expect to find few, if any, fissures near the basin center because on a basin-wide scale because the ground surface should be in compression and bedrock irregularities deeply buried. Fissure distribution in the Mimbres Basin is exactly the opposite of that predicted by such theories of fissure origin.

One explanation for the central clustering of Mimbres Basin fissures is that the cracks were formed by draping above deeply-buried basement structures, as proposed by Contaldo (1989). Whereas earth fissures in the Mimbres Basin tend to strike north-south (Contaldo and Mueller 1991), the Snake Hills fault zone beneath the most highly fissured area strikes northwest-southeast with movement down to the southwest. Even if a deeply-buried fault zone were favorably oriented, elastic solutions (Haneberg 1992a,b) show that displacments due to draping of basin-fill material over the fault would be strongly attenuated in a compressible sedimentary sequence. Faults within the basin fill sequence, such as those described in Haneberg et al. (1991) may also control earth fissure location; however, the single seismic reflection line across the fissure monitored during this study yields no information about the strike of these basin-fill faults. It is unlikely that the buried faults, which appear to be propagating upwards from deep within the basin fill sequence, were formed in response to groundwater overdraft; rather, the buried faults are more likely to be a near surface manifestation of the NW-SE striking Snake Hills fault zone. A third possibility is that fissure location can be controlled by small-scale heterogeneities such as buried channel deposits, which may be able to create localized zones of tension near the center of a subsiding groundwater basin.

The final section of this report contains preliminary models developed to investigate the effects of stratigraphic and structural irregularities on basin-wide subsidence patterns, using an analogy between surficial materials in a subsiding basin and a thin elastic plate. Although the development of new models was not included in the proposal for this study, the discrepancy between existing plane strain models and our field data compelled us to investigate models that might begin to explain our observations. These highly idealized models are not intended to mimmick conditions in the Mimbres Basin or any other subsiding groundwater basin, but rather to analyze the general effects of spatially variable loading on the deflection of a thin elastic layer.

The mechanical theory of simple elastic beams and plates is thoroughly documented in references such as Timoshenko (1940) and Timoshenko and Goodier (1970), and the use of simple beam and plate models to analyze geological phenomena has been summarized in a number of texts (Johnson 1970; Turcotte and Schubert 1982; Menke and Abbot 1990). Both simply supported beams (Dunrud 1984) and beams on elastic foundations (Kratzsch 1983) have been used to analyze subsidence over coal mines, but we have not found any published thin plate analyses related to the flexure of surficial strata overlying aquifers that are undergoing differential compaction. Limitations of elastic plate theory are that 1) the thickness of the plate is assumed to be small compared to its horizontal extent; 2) deformation of the plate occurs solely as vertical deflection of the neutral surface or mid-plane, and the neutral surface is neither stretched nor shortened; 3) the plate is composed of a linear elastic material; and 4) the plate is supported only along its edges, with no underlying substrate. A corollary of the second restriction is that both the magnitude of vertical deflection and its derivative, the slope of the plate, are small compared to the thickness and lateral extent. The fourth restriction further implies that the plate is weak, because deflections arising from any given load will be much greater than if the same load were applied to a plate resting on a continuous foundation. In practical terms, the use of a weak plate means that the applied loads will be much less than the

changes in effective stress, which presumably drive subsidence in real basins, developed during aquifer dewatering. Finally, the analysis presented below is restricted to plates of constant thickness; in general, however, elastic plate models can be formulated for plates of variable thickness.

Consider a relatively homogeneous surficial deposit underlain by a deforming basin-fill aquifer (figure 27A). On a basin-wide scale, the magnitude of subsidence will increase from the margins towards the center of the basin; however, we speculate that the effects of local stratigraphy and structure will produce irregularities in the subsidence profile. For example, one might find less subsidence in areas underlain by coarse-grained, relatively incompressible channel fill deposits than in areas underlain by finer-grained, more compressible alluvial deposits that consolidate over time as the aquifer is drained. In the Mimbres Basin, we have only indirect evidence— such as velocity changes on seismic reflection profiles and the general correspondence of channel-fill deposits to sinuous topographic highs with 1 to 2 m of relief— to support our supposition. Local topographic relief could be the result of processes unrelated to land subsidence, for example deflation of fine-grained deposits adjacent to coarser-grained channel fill deposits. Although a combination of detailed stratigraphic analysis and leveling will be required in order to test our assumption of localized differential compaction, we will tentatively accept the assumption of irregularity in order to proceed with the analysis. We also assume that the development of earth fissures is a two-stage process, in which the first-stage growth of a narrow opening mode crack is followed by second-stage piping and collapse, and restrict our analysis to modes of flexure that are ammenable to the formation of opening mode cracks.

ONE-DIMENSIONAL ANALYSIS

When an inhomogeneous aquifer is dewatered, transient pressure head gradients will develop because coarse-grained layers will drain more rapidly than fine-grained layers. The transient pressure head gradients, however, will dissipate over a period of time that is a function of layer thickness, layer compressibility, and permeability. In soil mechanics, this characteristic time is expressed as $\tau = H^2/C_v$, where H is the one-way drainage distance and C_v is the consolidation coefficient; in hydrology, the characteristic time is commonly written as $\tau = S_S H^2/K$, where S_S is the specific storage and K is the hydraulic conductivity of the clay. For a clay layer or lens surrounded by free-draining sand or gravel, H is one-half the thickness of the clay. As the pressure head gradient dissipates, the clay will consolidate whereas free-draining sand or gravel layers will remain essentially undeformed. The amount of subsidence occuring at any given location will thus be controlled by 1) the proportion of the dewatered interval that consists of compressible clays, and 2) the degree to which each clay layer has consolidated. After the pressure gradient has been completely dissipated, the total vertical compaction is given by the product of the change in effective stress, layer compressibility, and layer thickness. Assuming that the grains are incompressible, the maximum possible vertical strain is equal to the porosity of the clay layer.

In some cases, for example the use of surface deformation measurements to estimate stress or strain, then the relevant variable is clearly vertical displacement. In other cases, for example situations where the pressure gradient has not yet dissipated and consolidation of clays is minimal, it may be more appropriate to formulate problems in terms of changing effective stress along the base of the layer. In linear elastic problems, moreover, it is always possible, although not necessarily easy, to select a load distribution that will produce a particular deformed shape. This is because stress and strain are related by a single material constant for one-dimensional problems (Young's modulus) and two material constants for more complicated problems (Young's modulus and Poisson's ratio). Even in cases in which displacement seems to be the primary variable, therefore, mechanical problems can be formulated in terms of equivalent loads required to produce the desired final shape.

A surficial layer subjected to differential compaction can be compared to a simple beam under a combination of periodic and uniform loading (figure 27B). The periodic component of loading reflects changes in effective stress along the base of the beam due to the effects of inhomogeneity in the underlying, deforming aquifer. The uniform loading, in contrast, reflects a basin-wide increase in effective stress throughout the underlying aquifer. When added together, the the overall downward load on the layer is punctuated by smaller upward loads representing less compressible zones.

In this analysis, we will first consider an elastic beam of length L, thickness T, and breadth b. The load applied to the beam is given by some as-yet-unspecified function $q(x)$, which has units of force per unit length of beam. In

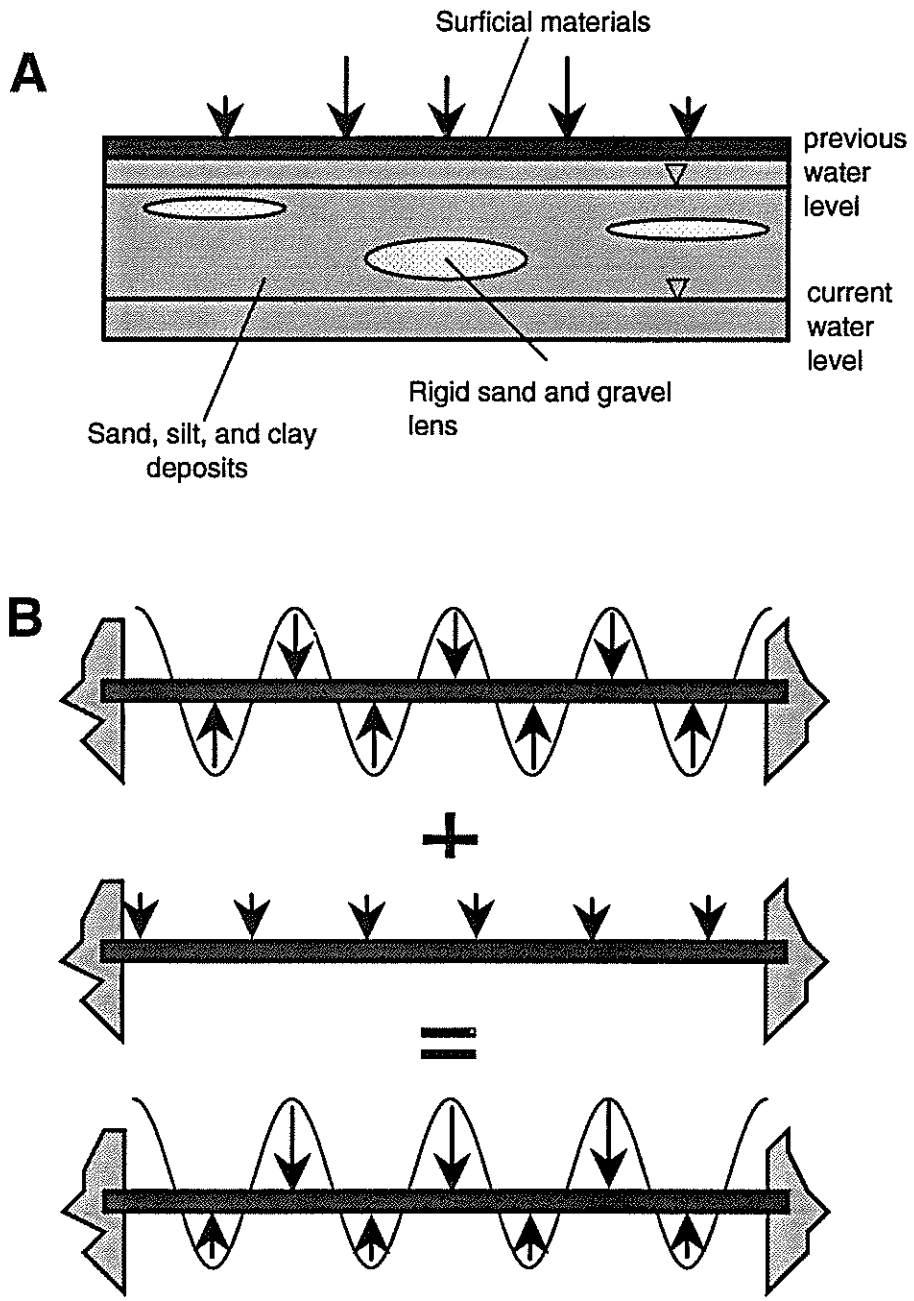

FIGURE 27. A) Idealization of a thin surficial layer subjected to variations in effective stress resulting from dewatering of an inhomogeneous aquifer. B) Mechanical model of the same surficial layer, subjected to a combination of periodic loading corresponding to the effects of stratigraphic and structural irregularities and uniform loading corresponding to basin-wide drawdown.

order to emphasize the highly idealized nature of this simple beam model, all results will be given in dimensionless form. Shearing force, Q, within the beam is the integral of the applied load, or

$$Q = \int q \, dx \tag{4}$$

The bending moment within the beam, M, is found by integrating the shearing force, or

$$M = \int Q \, dx \tag{5}$$

Positive bending moments correspond to concave-downward curvature (i.e., the upper surface of the beam is in tension) and negative bending moments correspond to concave-upward curvature (i.e., the upper surface of the beam is in compression). Finally, bending moment is approximately related to the vertical deflection of the beam, w, by

$$w(x) = (BI)^{-1} \iint M(x) \, dx dx \tag{6}$$

For a beam, B is equivalent to Young's modulus, E, and the moment of inertia is given by

$$I = bT^3/12 \tag{7}$$

We assume that the surficial layer is flat-lying and experiences no deflection at the basin margins. This corresponds to the boundary conditions $w = 0$ at $x = \pm L/2$ and $dw/dx = 0$ at $x = \pm L/2$; in the terminology of engineering mechanics, these would be refered to as built-in or clamped ends.

For our purposes, the loading term is a combination of both uniform and periodic components specified by

$$q(x) = -q_0 \, [(1/m) - \cos (n\pi x/L)] \tag{8}$$

The term $-q_0/m$, which has units of force per unit length of beam, represents a downward-directed force applied uniformly across the entire beam. (A negative sign indicates a downward directed load, and a positive sign indicates an upward directed load.) The term $q_0 \cos (n\pi x/L)$ represents a load with a periodically (in space) changing sign. When the two components are combined, the result is a sign curve shifted vertically according to the magnitude of m, as illustrated in figure 28. If $m = 1$, then there are no upward-directed forces acting on the beam and the total load is somewhat analogous to a series of downward-directed point loads. If $m > 1$, then the load alternates between upward- and downward-directed forces. Finally, as $m \rightarrow \infty$ the load is equally partitioned between upward- and downward-directed forces.

For the loading function and boundary conditions specified in the previous two paragraphs, the problem can be solved by integrating four times and solving for the resulting constants of integration. The results, presented in dimensionless form, for deflection of the neutral surface, bending moment, and shearing force for the built-in beam are:

$$\begin{aligned} wEbT^3(A_0L^4)^{-1} = (12/384) \, \{ & (n\pi) \, [1 - 8 \, (x/L)^2 + 16 \, (x/L)^4] \\ & + 384 \, m \, [\cos (n\pi/2) - \cos (n\pi x/L) \\ & - n\pi \, (x/L)^2 \sin (n\pi/2)] \end{aligned} \tag{9}$$

$$\begin{aligned} M \, (A_0L^2)^{-1} = - \{ & (1/m) \, [(1/24) - (1/2) \, (x/L)^2] - (n\pi)^{-2} \cos (n\pi x/L) \\ & + 2 \, (n\pi)^{-3} \sin (n\pi/2) \} \end{aligned} \tag{10}$$

$$Q \, (A_0L)^{-1} = (1/m) \, (x/L) - (n\pi)^{-1} \sin (n\pi x/L) \tag{11}$$

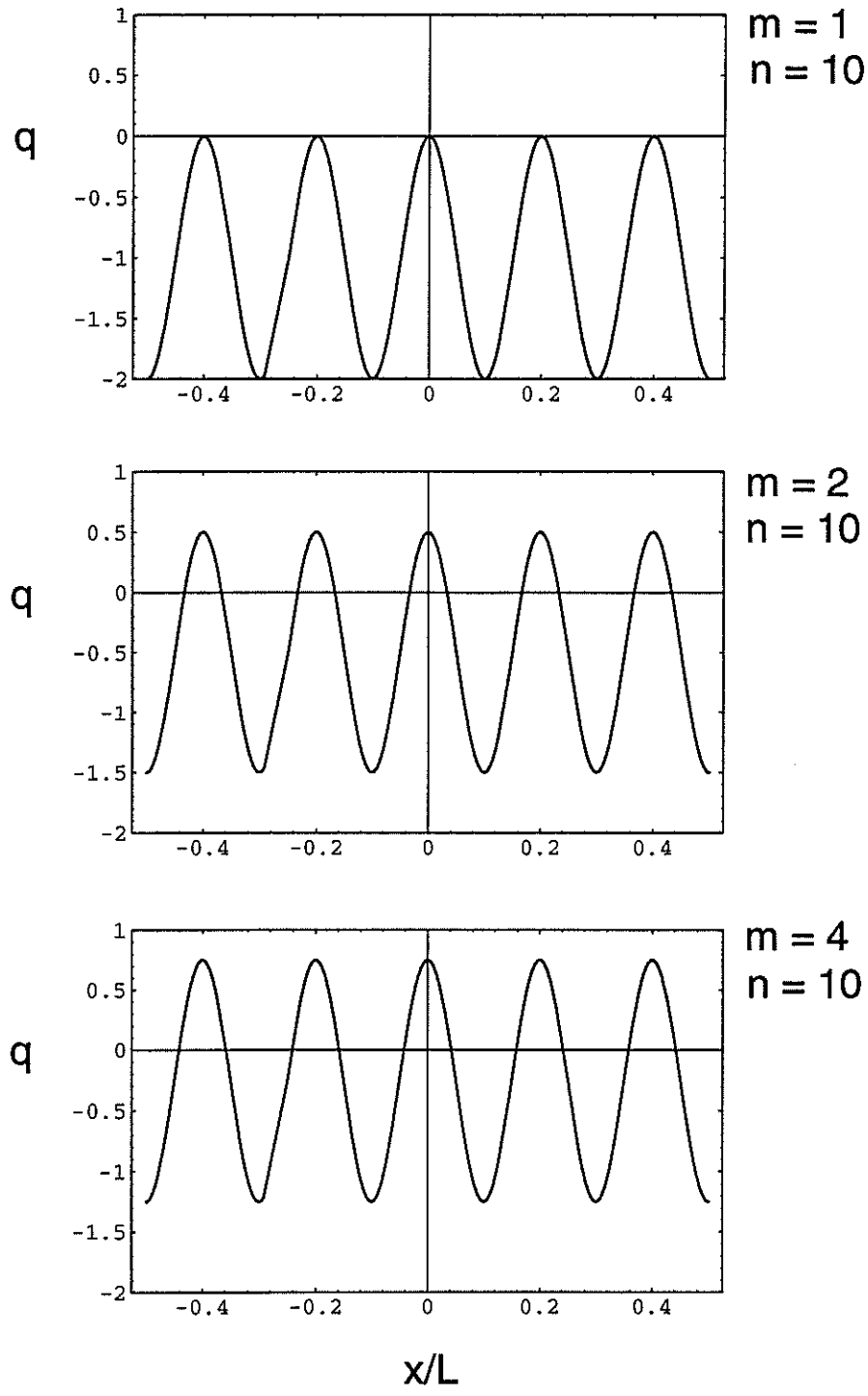

FIGURE 28. Plots of the loading function q for n = 10 and different values of m. The effect of increasing m is to shift the curve upward so that q approaches a pure cosine curve with an increasingly small component of uniform load.

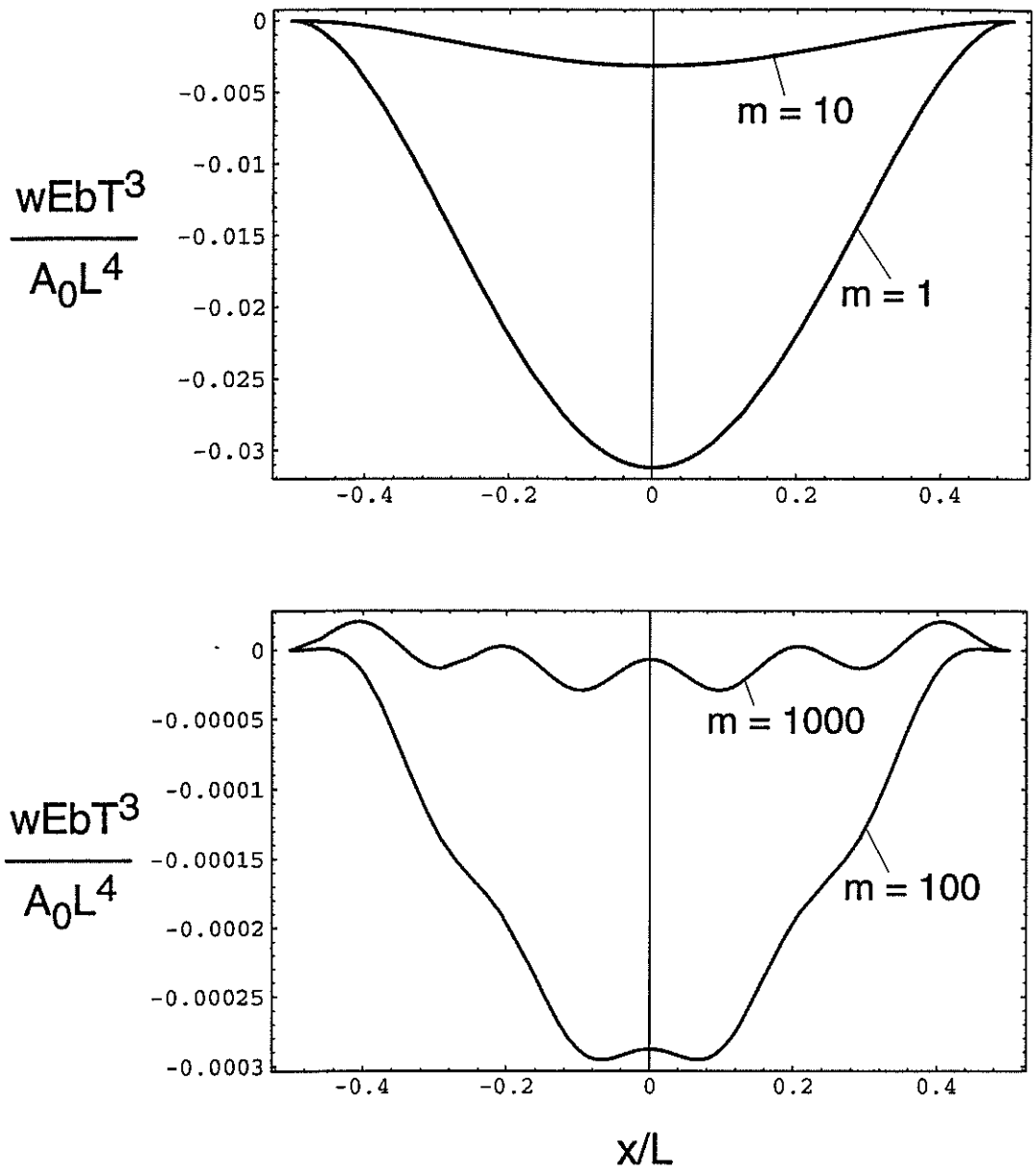

FIGURE 29. Dimensionless deflection of a one-dimensional simple elastic beam, as given by equation (6), for n = 10 and different values of m. Note that different vertical scales are used on the upper and lower graphs.

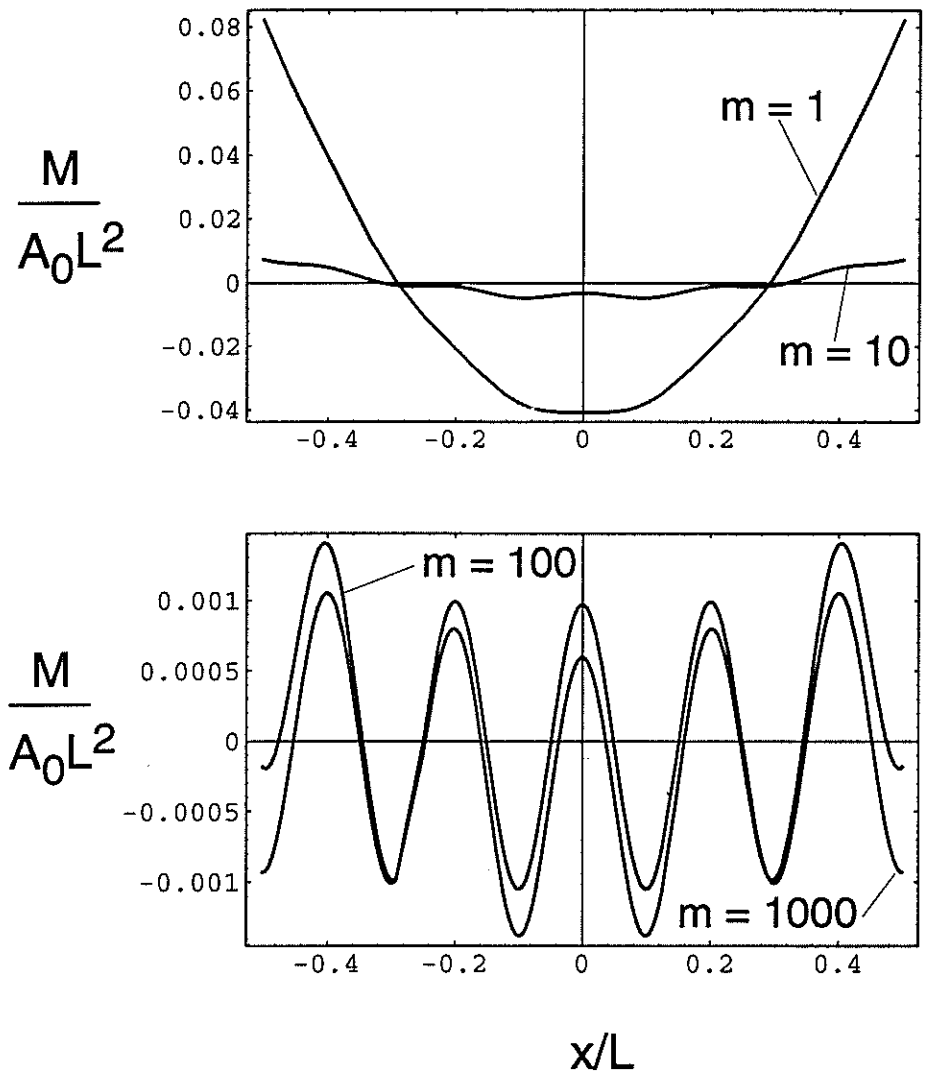

FIGURE 30. Dimensionless ending moments corresponding to the deflection curves shown in figure 25. Positive bending moments correspond to concave-downward curvature (i.e., tension along upper surface) whereas negative bending moments correspond to concave-upward curvature (i.e., compression along upper surface). Noe that different vertical scales are used on the upper and lower graphs.

In addition to reinforcing the simplified nature of the highly idealized model, a dimensionless format allows the general forms of the solutions to be examined without having to specify values for variables such as q_0, E, L, b, and h.

Results are illustrated below by plots of dimensionless deflection (figure 29) and dimensionless bending moment (figure 30) calculated for values of $n = 10$ and $m = 1$, 10, 100 and 1000. Dimensionless shearing force is not plotted because the primary focus of this analysis is the relationship between the subsidence profile and zones of tension in which earth fissures could be formed. Shearing force would become an important quantity if the analysis were concerned with the origin of small faults in surficial deposits. For each order of magnitude increase in m, there is a corresponding order of magnitude decrease in the dimensionless deflection. For small m, on the order of 1 or 10, the deflection curve is smooth and the only effect of the periodic loading component is to decrease the amount of deflection. As m is increased, however, the form of the deflection curve becomes more complicated and two distinct wavelengths of flexure are apparent as the influence of the periodic loading component increases relative to that of the uniform loading component. For $m = 1000$, the amplitudes of the short wavelength oscillations are very nearly equal to the amplitude of the longer wavelenth oscillation. For $m = 1$ and 10, the bending moment curve is simply flattened and less negative near the basin center. For $m = 100$ and 1000, however, the bending moment actually becomes positive, indicating tension along the upper edge of the beam.

TWO-DIMENSIONAL PLATES

The one-dimensional analysis described above can be easily extended to two-dimensions, although analytical solutions are available for only a few simple loading configurations. For the combined uniform and periodic loading used to simulate irregular subsidence, it will be necessary to resort to a numerical solution. The equation describing deflection of a thin rectangular plate of dimensions L_x by L_y and supported on all four sides is (Timoshenko 1940, p. 88)

$$(\partial^4 w/\partial x^4) + 2\,(\partial^4 w/\,\partial x^2 \partial y^2) + (\partial^4 w/\partial y^4) = q/D \qquad (12)$$

As in the one-dimensional case, w is the vertical deflection of the plate and q is a distributed load, but this time with units of pressure. The flexural rigidity of the plate is given by

$$D = (E\,T^3) / [12\,(1-\nu^2)] \qquad (13)$$

where E is Young's modulus, T is plate thickness, and ν is Poisson's ratio. We solved equation (12) by finite-differences, using a 13-point scheme based on the approximations (*cf.* Timoshenko and Goodier 1970, p. 539)

$$\partial^4 w/\partial x^4 \approx [w_{i,j-2} + w_{i,j+2} - 4\,(w_{i,j-1} + w_{i,j+1}) + 6\,w_{i,j}]\,(\delta x)^{-4} \qquad (14)$$

$$\partial^4 w/\partial x^4 \approx [w_{i-2,j} + w_{i+2,j} - 4\,(w_{i-1,j} + w_{i+1,j}) + 6\,w_{i,j}]\,(\delta x)^{-4} \qquad (15)$$

$$\partial^4 w/\partial x^2 \partial y^2 \approx [4\,w_{i,j} - 2(w_{i,j-1} + w_{i,j+1} + w_{i-1,j} + w_{i+1,j}) + w_{i+1,j-1} + w_{i-1,j-1} + w_{i+1,j+1} + w_{i-1,j+1}]\,(\delta x)^{-4} \qquad (16)$$

The equation in Timoshenko and Goodier (1970, p. 539) corresponding to our equation (16) is in error due to a misplaced square bracket; the correct expression can be easily derived and checked. The finite-difference grid used in this approximation is schematically illustrated in figure 31. Substituting these approximations into equation (12), solving for $w_{i,j}$, and dividing the result through by $L_x = 1$, we arrive at the normalized expression

$$\begin{aligned} w_{i,j} / L_x \approx (12/20)(1-\nu^2)\,(q/E)\,(dx/L_x)^4\,(T/L_x)^{-3} &+ (8/20)(w_{i+1,j} + w_{i-1,j} + w_{i,j+1} + w_{i,j-1}) \\ &- (2/20)(w_{i+1,j+1} + w_{i+1,j-1} + w_{i-1,j+1} + w_{i-1,j+1}+) \\ &- (1/20)(w_{i+2,j} + w_{i-2,j} + w_{i,j+2} + w_{i,j-2}) \end{aligned} \qquad (17)$$

The loading function used in this analysis is a two-dimensional equivalent of equation (8) for a square plate of dimension $L_x \times L_x$

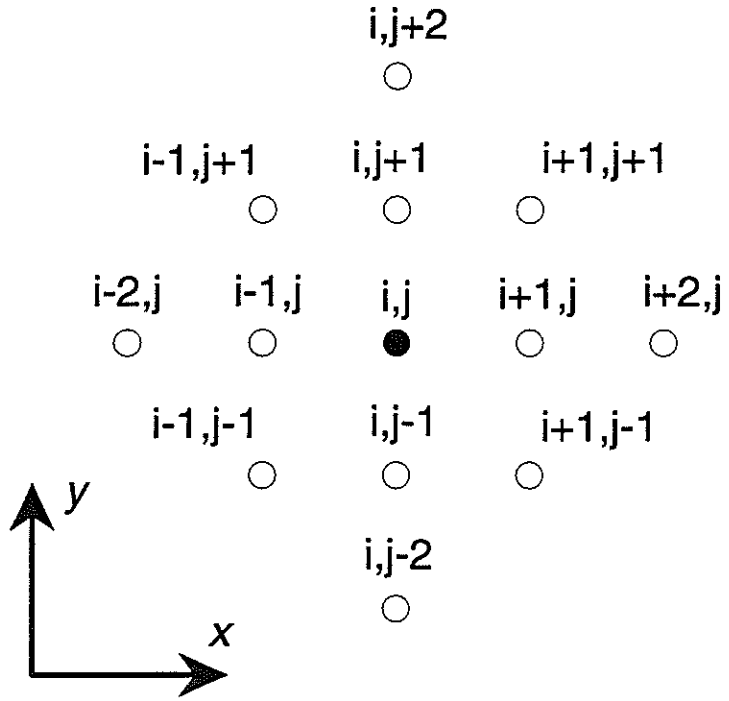

FIGURE 31. Illustration of the 13-node finite-difference grid used to calculate deflection at point i,j. Horizontal, dx, and vertical, dy , node spacing are equal.

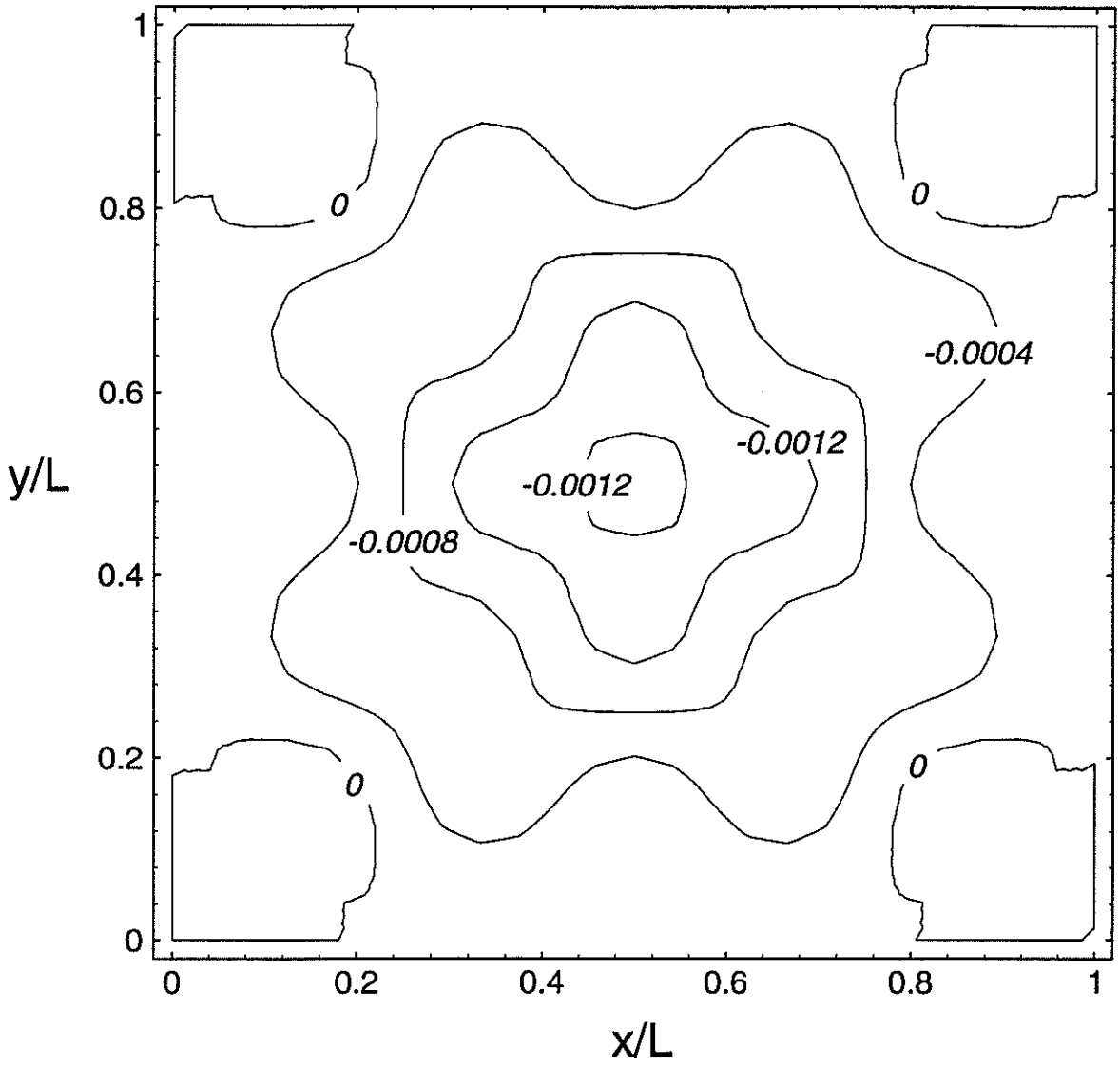

FIGURE 32. Contour plot of dimensionless deflection of the neutral surface of a square elastic plate with combined uniform and periodic loading, calculated on a 21 by 21 node finite difference grid. Parameters used in the calculations were $q/E = -1x10^{-9}$, $T/L = 0.001$, $\nu = 0.25$, $m = 100$, $n = 3$.

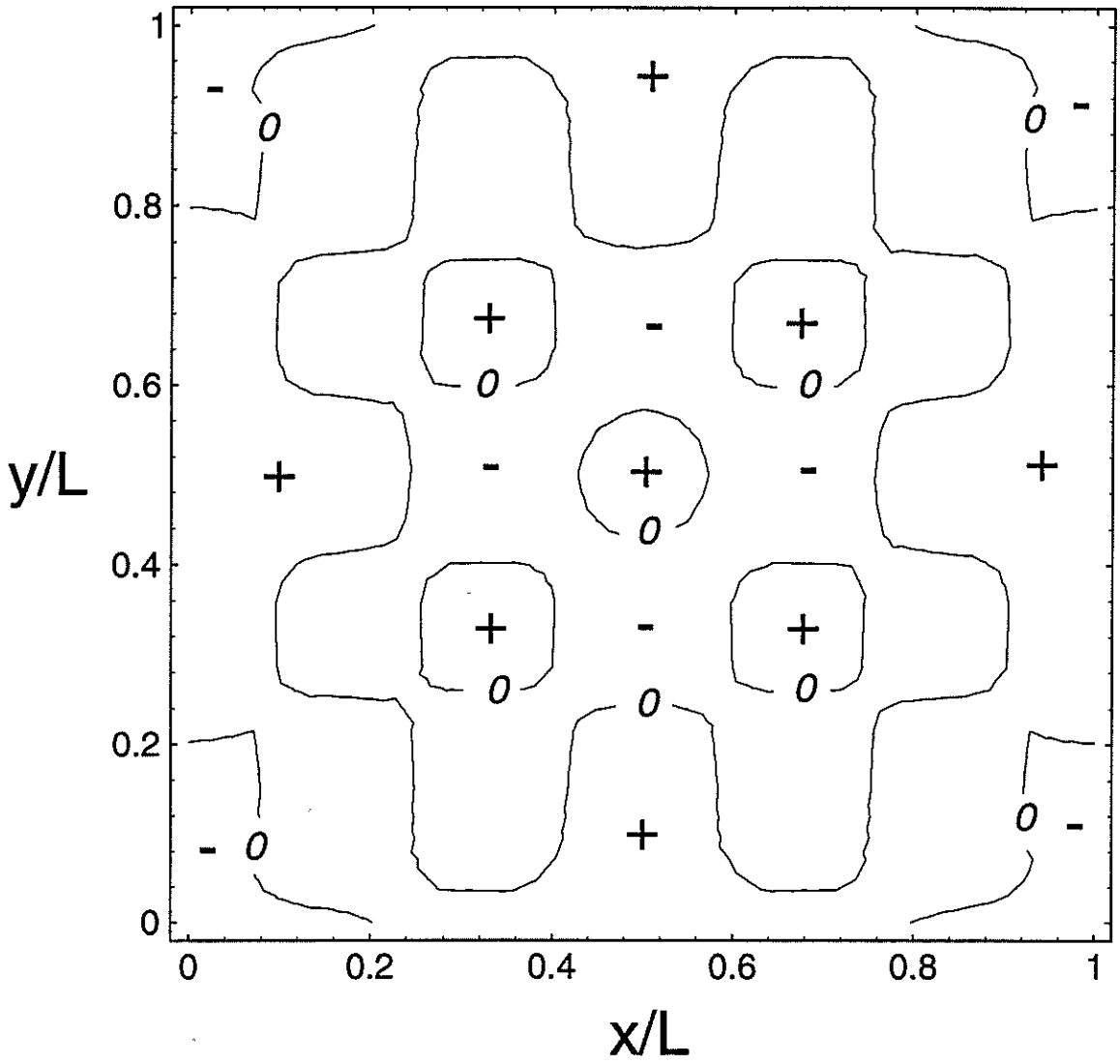

FIGURE 33. Contour plot of dimensionless bending moment, 12 M $(1-\nu^2)/[L^2 E (T/L)3]$, along the neutral surface of a thin elastic plate subjected to combined uniform and periodic loads. Only the zero contour is shown, in order to isolate areas of positive and negative bending moments, as indicated by the plus and minus signs. Areas of positive bending moments correspond to zones of tension, where opening mode cracks are predicted to occur, along the upper surface of the plate.

$$q(x,y) = -q_0 \left[1/m - \cos(2n\pi x/L_x)\cos(2n\pi y/L_x)\right] \quad (18)$$

which has both uniform and periodic components analogous to the one-dimensional loading function used in the previous section. The dimensionless bending moments per unit width in the x and y directions are (*cf.* Timoshenko and Goodier 1970, p. 288-289)

$$12\, M_x (1-\nu^2)/[L^2\, E\, (T/L)^3] = -(\partial^2 w/\partial x^2 + \nu\, \partial^2 w/\partial y^2) \quad (19)$$

and

$$12\, M_y (1-\nu^2)/[L^2\, E\, (T/L)^3] = -(\partial^2 w/\partial y^2 + \nu\, \partial^2 w/\partial x^2) \quad (20)$$

Boundary conditions are also analogous to those used in the one-dimensional analysis: $\partial w/\partial x = 0$ along $x/L_x = \pm 1/2$ and $\partial w/\partial y = 0$ along $y/L_x = \pm 1/2$, and $w/L_x = 0$ along $x/L_x = \pm 1/2$ and $y/L_x = \pm 1/2$.

A 23×23 node finite difference grid was used to calculate deflection, bending moment, and tilt values using the parameters listed in Table 1. The combination of uniform and two-dimensional periodic loading produces a convoluted pattern of deflection contours consisting of hummocky irregularities superimposed on a plate-wide pattern of downward deflection (figure 32). Bending moments were calculated from the deflection solution using a standard second-order accurate finite difference approximation. Because the plate is square and the periodic component of loading is isotropic, $M_x = M_y$ for this example; in general, however, $M_x \neq M_y$. As shown in figure 33, the sign of the dimensionless bending moment alternates in a checkerboard pattern, meaning that the location of opening mode cracks could be distributed across the entire plate instead of being restricted to its periphery. Finally, tilts were calculated using a simple finite difference approximation for the first derivative of the deflection (figure 34). The tilts were calculated on a 22×22 grid (one tilt value between each pair of calculated deflection values) but, to simplify the diagram, figure 34 shows every other tilt value. As with the deflection plot, highly variable local tilt perturbations are superimposed upon an overall pattern of tilting towards the center of the plate. In order to properly interpret figure 34, it is important to realize that the vectors represent directions and magnitudes of tilt angles, not displacements or velocities. In a thin plate with small deflections, the slope of the deformed plate is equal to the tangent of the tilt angle. Comparing adjacent sets of tilt arrows, it is possible to find zones of compression (two arrows pointed at each other), tension (two arrows pointed away from each other), and out-of-plane shear (two parallel arrows of different magnitude pointing in the same or two parallel arrows pointing in opposite directions). Two arrows pointing in the same direction indicate out-of-plane shear only if they are of different magnitude because the arrows represent downward tilt rather than displacement. To visualize this, imagine that each tilt arrow represents the tilt of a discrete blocks. Even if both blocks are rotated about the same axis and in the same direction, out-of-plane shear will result if the amount of rotation in the blocks is not identical.

Table 1. Dimensionless parameters used for the two-dimensional plate model

L_y/L_x	1.
T/L_x	0.001
$\delta(x/L_x)$	0.05
m	100
n	3
q_0/E	$-1.\times10^{-9}$
ν	0.25

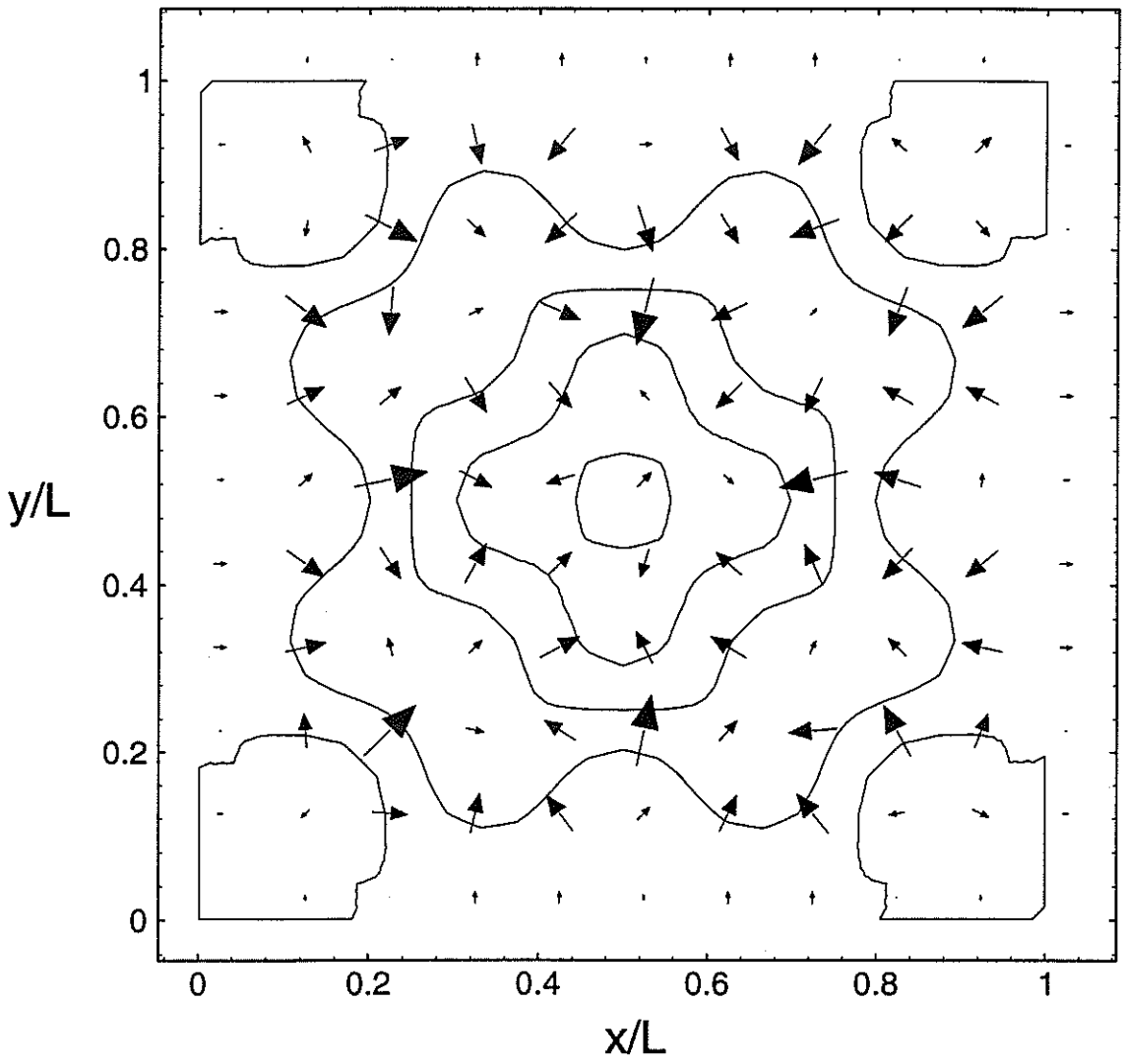

FIGURE 34. Vector plot of tilt angles for a thin elastic plate subjected to combined uniform and periodic loads. Arrows indicate the direction and relative magnitude of tilt of the neutral surface of the plate, and are superimposed upon the deflection contours illustrated in figure 32.

DISCUSSION

SUITABILITY AND RELIABILITY OF INSTRUMENTATION

The tiltmeters used in this study appear to have performed well. The units are able to measure both short- and long-term deformation near the fissure. All of the units have remained within their high-gain measurement range, except for the short period of time when initial settling caused T-B to tilt out of range. High gain yields information about daily variations that are indistinguishable on the low gain setting. Overall, the tiltmeters are simpler to install and operate than some other types of instrumentation, such as wire extensometers, require little to no maintenance, and appear to produce few spurious data.

Tiltmeters and the data they provide do have limitations. It is important to emphasize that tiltmeters do not measure displacement, only the direction and magnitude of tilt and, hence, rotation of the sediments in the area near the fissure. No inference can be made regarding information on translational movement of the units such as might occur due to in-plane shear. Since there is no information on translation, it is assumed that no horizontal displacement has occurred and that only rotational deformation has taken place. Additionally, long-term drift and/or physical settling of the tiltmeters could not be evaluated in this study. If deformation were perfectly elastic, yearly tiltmeter movements could be expected to close and any differences could be taken as instrument drift or settling. However, there is no reason to believe that the deformation is perfectly elastic, so effects such as drift or settling could not be studied. Independent measurement of strains and/or displacements would have also provided a means by which to evaluate the possibility of settling. Installation of the tiltmeters in steel casings means that the recorded values represent tilts averaged over the length of the casing. A more complete picture of total deformation near the fissure would require extensometers or survey monuments be installed in addition to tiltmeters.

The pressure transducers proved to be unreliable for extended monitoring periods. While the units give good short-term data regarding daily fluctuations, longer-term trends are difficult to record because of the unreliability of the units. The pressure range of the units appears to be well suited to fluctuations that occur within the aquifer.

The data logger and multiplexer performed well and proved to be the most reliable of the various components. Once the power supply was set up correctly, it operated without the need for much maintenance. The only component which required attention was the battery which provides −12 V to the tiltmeters. Regularly exchanging this battery during each trip to the field site proved successful in preventing voltage drops that cause erroneous readings.

COMPLEX DEFORMATION

Previous earth fissure studies have used various types of instrumentation to document deformation near fissures. Boling (1984) fitted a fissure with dial gauges and Pyrex tubes to measure horizontal strains. Carpenter (1988) used horizontal extensometers and transducers to measure movement perpendicular to a fissure along with groundwater levels and barometric pressure. Level lines and horizontal distance surveys have also been used to determine vertical and horizontal displacements across fissures (Holzer and Pampeyan 1981; Carpenter 1988; Larson and Pewe 1986). Because the data in these studies was collected along lines perpendicular to the fissures, the studies implied that fissuring could be analyzed as a plane-strain process. Measurements made during the course of this study have components of tilt both parallel and perpendicular to the fissure, suggesting that deformation at the Mimbres Basin site is more complicated than that implied by previous researchers.

TILT-WATER LEVEL CORRELATION

Physical settling, electrical drift, random noise, and the short length of record may complicate the interpretation of long term tiltmeter data. Physical drift, which is settling of the tiltmeter and sand within the casing, may have occurred. Settling is believed to be the cause of T-B tilting out of range during the initial weeks after installation. However, the units were all installed for approximately five weeks prior to any data collection due to power supply difficulties. During this period, the units undoubtedly settled somewhat and should have been stable by the time the

actual data collection began in mid-January. The actual effects of any possible settling would be extremely difficult to quantify. If the deformation at the site were perfectly elastic, one could expect closure of the tiltmeter record after one year of monitoring, and any differences could be attributed to drift. However, there is no reason to assume perfectly elastic conditions exist and it is not possible to determine the magnitude of any settling which may have occurred. It is possible to reduce settling by grouting or cementing the tiltmeter in the borehole, but this would make instrument recovery impossible. Electronic drift of the tiltmeters is believed to be on the order of 10 to 20 μrad per year (Gary Holzhausen, Applied Geomechanics, pers. comm., 1992), which is small compared to the variations observed in the data records for the tiltmeters. Random tilts may have been inadvertently incorporated into the data by installing the tiltmeters in cased boreholes, which means that the observed value is averaged over the length of the casing. Finally, data records that are several times the length of the longest wavelength present are preferred for harmonic analyses. These will become available as monitoring continues.

ORIGIN OF CYCLES

The cycles apparent in short-term tilt and water level records are believed to result from a combination of earth tide effects and barometric pressure fluctuations. The effects of these phenomenon upon aquifers have been widely documented. Robinson (1939) documented fluctuations that he determined to be caused by earth tides in wells tapping confined aquifers in New Mexico and Iowa. Bredehoeft (1967) expressed mathematically the various parameters that affect the response in both confined and unconfined aquifers and found that earth tides should be observed in most wells that penetrate well confined aquifers. He also determined that tidal effects are not as common in unconfined aquifers because of the extremely low porosities required. Weeks (1979) studied barometric fluctuations in wells tapping deep unconfined aquifers and found that fluctuations may be significant if the unsaturated zones are thick and/or have a low permeability to air. Responses of a porous formation with compressible grains to both earth tide and barometric effects were studied by van der Kamp and Gale (1983). They found that the manner in which an aquifer responds can give indications of both the hydraulic and elastic properties of the affected formation. Rojstaczer and Riley (1990) studied the water level responses in wells tapping unconfined aquifers to both earth tide and atmospheric loading conditions. They developed a variety of dimensionless flow parameters which control the response of unconfined aquifers. Further information on these subjects can be found in Turk (1975), Gieske (1986), Hsieh et al. (1988), Rojstaczer and Agnew (1989), and Ritzi et al. (1991).

Earth Tide Effects

Each point on the earth's surface is subjected to two forces: 1) the inward gravitational force resulting from the attraction of the earth's mass, and 2) the outward centrifugal force resulting from the rotation of the earth (Melchior 1966). The vectorial sum of these forces is directed toward the center of the earth and defines the vertical orientation. Gravitational attraction between the earth, moon, and sun, alters the vertical and imposes stresses upon the earth. This phenomenon causes ocean tides, as the free surface of the sea adapts itself to a level surface in equilibrium with the disturbed vertical (Melchior 1966). The solid earth is similarly deformed, but to a lesser degree, by the tidal forces.

Tidal forces have an inverse effect on groundwater levels. High tides, which generally occur when the moon is overhead, dilate the earth's crust. This dilation in turn causes expansion of the underlying aquifer and a reduction in the formation pressure at depth (Ritzi et al. 1991). The result is a decrease in the water level observed in a well (Melchior 1966). At low tide, the crust is compressed, which increases pressures, causing water levels to rise. The time lag that exists between tide passage and water level response, is caused by the time required for water to flow into or out of a well (Hsieh et al. 1988). Earth tides also impose very small horizontal strains on the earth's surface as the tidal bulge passes (van der Kamp and Gale 1983).

The type and magnitude of response to tidal deformation observed in wells is quite varied and depends on a number of factors. Of primary interest is whether the aquifer is confined or unconfined or lies somewhere between these two extremes. In a confined aquifer, dilatation caused by tidal forces results in a volume change in the pore water, assuming that the volume change of the aquifer matrix is small compared to that of the water (Bredehoeft 1967). The volume change is consequently accompanied by a change in pressure head that can then be readily noted as water flows into or out of an observation well.

For an unconfined aquifer, the situation is more complicated. First, it is important to note that a distinction can exist between water level fluctuations observed in a well and the response of the water table in unconfined aquifers (Rojstaczer and Riley 1990). This arises is cases where the vertical hydraulic diffusivity is low, such as when horizontal stratification exists with the aquifer (Bredehoeft 1967). This reduces the vertical conductivity of the formation and insulates the aquifer pressure head response from that of a fluctuating water table. A response in a well, screened only at some depth below the phreatic surface, will depend on not only on the flow of water into or out of the bore, but also on any vertical flow of water to and from the water table (Rojstaczer and Riley 1990). This effect means that responses in a well caused by rapid deformations will not be affected by water table fluctuations as would responses caused by slow deformations because of the time required for vertical flow from the water table to reach the well screen (Rojstaczer and Riley 1990). Consequently, a well, tapping a deeper portion of a thick, unconfined sequence, will be only slightly influenced by water table fluctuations. Rojstaczer and Riley (1990) liken this situation to that of a partially confined aquifer system.

It appears that the primary distinction between the behavior of confined and unconfined aquifers is that in confined aquifers, pressure head variations diffuse quite slowly as compared to loading fluctuations, resulting in flow into or out of the well bore to reestablish a pressure equilibrium (Domenico and Schwartz 1990). This is considered an undrained response. In unconfined aquifers, the response consists of vertical fluid flow that quickly dissipates the pressure change within the aquifer system which represents a drained aquifer response (Domenico and Schwartz 1990). Site specific aquifer properties can lead to exceptions of these generalizations.

The hydrologic factors affecting water level changes caused by earth tides include the hydraulic conductivity of a formation which controls the rate at which fluid moves into or out of a well bore. The specific storage, which is defined as the amount of water released from, or taken into storage per unit volume of aquifer under a unit change of hydraulic pressure head, determines the amount of water that will be available for flow as pressures fluctuate. Specific yield is a term usually applied to unconfined aquifers, which represents the volume of water that drains from pore spaces per unit surface area of aquifer as a result of a unit decline in the water table (Domenico and Schwartz 1990).

Elastic properties of an aquifer will also affect the response to tidal stresses. These parameters include the compressibility of water and the solids within the aquifer, along with the Poisson's ratio, porosity, and permeability of the aquifer (Rojstaczer and Riley 1990). An aquifer more sensitive to tidal forces will generally have low porosity (Rojstaczer and Agnew 1989). Additionally, sensitivity is also a strong function of matrix compressibility with a lower compressibility making an aquifer more sensitive to tidal stresses (Rojstaczer and Agnew 1989).

Well bore storage will also affect the earth tide response in aquifers. Throughout the analysis of tidal effects, an assumption is usually made that the bore is narrow so that little flow is required to change the level in the well (Rojstaczer and Riley 1990). However, the actual water level within the well may not reflect the pressure head in the aquifer because a period of time may be needed for sufficient water to flow into the well bore to bring the system to an equilibrium (Rojstaczer and Agnew 1989).

Rojstaczer and Riley (1990) point out that larger water table fluctuations are expected where aquifers have a high hydraulic conductivity, high specific storage, and a low specific yield. Such an aquifer will yield large quantities of water when deformed and will be able to transport this water to and from the water table very rapidly. The low specific yield will result in larger fluctuations in the water table for a given mass of water moved to or from the water table. However, large scale fluctuations cannot be expected unless the aquifer has a very high hydraulic conductivity and a low specific yield (Rojstaczer and Riley 1990). Additionally, Bredehoeft (1967) states that to observe a response in a well tapping an unconfined aquifer, the saturated thickness must be large and/or the porosity must be very low.

Generally, the response of wells to earth tide deformation in unconfined aquifers is thought to be small (Bredehoeft 1967; Rojstaczer and Riley 1990). The aquifer properties at the study site, such as the conductivity, specific storage, or specific yield are largely unknown. However, properties such as porosity or possible partial confinement, caused by the various clay rich zones, may be such that tidal effects contribute to the fluctuations observed in short-term water level records. There were no barometric pressure readings taken at the site, so the

effects of these two phenomenon can not be separated to determine true tidal effects. It is also unclear precisely how much of the observed tilt results from surface strain or from deformation of the underlying aquifer and the associated changes in water level and effective stress. Horizontal strains, suggested by van der Kemp and Gale (1983), are present in tiltmeter records when two tilt channels are plotted against each other (figure 27).

Barometric Pressure Effects

Barometric pressure fluctuations initiate changes in groundwater levels by the pressurization (or depressurization) of water in an open well and by diffusion of the pressure wave through the subsurface to the aquifer. The pressure changes are largely thermally driven with higher pressures occurring during the day with low pressures at night. Additionally, changes occur with the passage of weather fronts with periods of several days. However, the more prominent affects on groundwater records at the study site are those associated with temperature driven pressure fluctuations that occur with both diurnal and semi-diurnal periodicities.

In contrast to earth tide loading, atmospheric loading acts on the water in the well along with the aquifer matrix and pore water (Domenico and Schwartz 1990). When a barometric pressure change occurs, water in an open well is affected instantaneously while the aquifer itself is not affected until the pressure wave propagates through the unsaturated and any confining layers, if present, to reach the aquifer (Domenico and Schwartz 1990). This lag creates a pressure differential between the water in the well and the pressure head in the aquifer (Weeks 1979). A pressure gradient is formed which initiates fluid flow. Increasing barometric pressure creates a pressure gradient away from the well causing the water level to drop, while pressure reductions lead to a rise in water level in the well (Domenico and Schwartz 1990).

Again, aquifer properties, such as those listed previously in the discussion regarding earth tides, will affect the magnitude of water level fluctuations observed. Of primary importance is the confinement of an aquifer. An unconfined aquifer may have a diminished or delayed response as compared to a confined aquifer. In the unconfined case, air must move through the unsaturated zone in order to transmit the pressure change to the water table (Weeks 1979). The rate of propagation is controlled by the permeability of the unsaturated zone and by the capacity of the zone to store or release soil gas (Weeks 1979). An aspect of vertical flow arises in both unconfined and partially confined conditions as pressure fluctuations initiate flow between the water table and the aquifer (Rojstaczer 1988). With a confined aquifer, the pressure change is transmitted almost instantaneously through the confining layer, with little attenuation, where the pressure changes are supported primarily by the pore water in the aquifer (Weeks 1979).

Another aspect of atmospheric pressure fluctuations that can affect water levels involves the transfer of water to and from the capillary fringe. Turk (1975) investigated the nature of shallow water table fluctuations as a result of thermally driven air pressure changes. Hydrographs from shallow (< 2 m) observation wells illustrate similar water level behavior to short-term records obtained during this study. He determined that air entrapped within the capillary fringe naturally occupies varying amounts of space dependent on atmospheric pressure fluctuations. As pressures increase, the entrapped air occupies less space, thereby leaving more space for capillary water. Water from below the phreatic surface moves upward to fill the capillary fringe causing a drop in the water table. Conversely, as pressure decreases, the entrapped air expands, forcing the capillary water back down into the water table causing it to rise. This effect was observed in very shallow unconfined aquifers and it is uncertain that this mechanism is at work at this study site because of the much greater depth of the phreatic surface and the uncertain presence of soil gas in the deep subsurface.

Again, the properties of the aquifer and unsaturated zone at the study site are not precisely known. Because the primary goal of the study was to observe the relationship, if any, between tilts and water level fluctuations, a barometer was not installed at the site. However, the depth to water (42 m) is believed to be sufficient to cause a lag in pressure wave propagation that can initiate the formation of pressure gradients around the well bore which contribute to the cycles observed in water level data at the study site.

Other Possible Causes

Another possible explanation for tiltmeter movement involves topographically driven soil creep. The tiltmeters are positioned on a topographic high that slopes downward to a shallow depression to the north (figure 4). However,

this explanation seems unlikely because of two factors. First, the relief at the site is only about 2 m while the tiltmeters are all emplaced at depths greater than 2 m. As such, the units should be below the zone of any possible creep effects. Secondly, if creep were a factor, the tiltmeters should display a definite trend towards the topographic depression. Again, this is generally not the case as the units display a variety of trends with none consistently oriented toward the depression (figures 15 and 16).

THIN-PLATE MODELS OF SURFACE DEFORMATION

The mathematical models developed in this report are intended to analyze the behavior of a highly idealized, thin elastic layer subjected to spatially variable changes in vertical effective stress. The loading pattern is intended to reflect the combination of hydraulic head decrease and aquifer compressibility that controls the magnitdue of subsidence above a dewatered aquifer. No attempt was made to reproduce field observations or predict future movements near the Mimbres Basin fissure monitored during this study. As very generalized analogs, the thin plate models appear to have some interesting implications for the deformation of near-surface strata in a subsiding basin.

Tilt arrows located along topographic highs in figure 34, which might be analogous to the location of the fissure studied during this project, suggest that it should not have been surprising to have observed a variety of tilts in response to basin-wide drawdown. Tilt azimuths range over 90°, and tilt magnitudes range over a factor of five, in response to a simple periodic loading pattern. If the loading were to vary with time as well, which clearly would be the case in a subsiding groundwater basin, then we would expect even more complicated patterns of deflection and tilt. This superposition of local and regional components of flexure suggests that care must be taken when attempting to infer the nature of basin-wide processes from localized observations.

Complicated tilt patterns, such as those observed in the field and calculated using the thin plate model, have important implications for the design and interpretation of results from fissure monitoring studies. Previous researchers have measured horizontal or vertical movement along traverses perpendicular to the fissure; these traverses will, of course, provide evidence only of movement perpendicular to the fissure. Thus, it is impossible for the data to be inconsistent with the hypothesis of plane strain perpendicular to the fissure simply because no attempt was made to collect contradictory data. Likewise, a single vertical slice through the elastic plate represented in figure 34 will show only components of tilt parallel to the slice, regardless of the orientation of the slice. Measurement of tilts or displacement in two (preferably orthogonal) directions is necessary in order to truly determine whether or not deformation occurs in a plane. Therefore, future earth fissure monitoring programs must be designed to measure displacement or tilt both perpendicular and parallel to the fissure. This might be accomplished by using tiltmeters, as in this study, or two-dimensional arrays of surface monuments and/or extensometers arranged in quadrilaterals. One possibility might be an approach similar to that of Baum and others (1988), who developed a method that uses quadrilateral networks of surface monuments to measure strain and tilt at the surface of a landslide and displacement across the boundaries of a landslide.

Both the one-dimensional beam and two-dimensional plate models require large values of m (or, conversely, small values of $1/m$) in order for the localized effects of periodic loading to become evident. For small values of m, the subsidence profile is a smooth curve with little indication of localized irregularities. In other words, the amplitude of the periodic component of loading must be much larger than the uniform downward component of loading in order to produce a hummocky deflection pattern in a thin elastic plate. Extending the analogy, we speculate that near-surface stratigraphic details may control whether or not earth fissures develop in response to a given amount of subsidence. If the near-surface strata are strongly inhomogeneous and the effective stress changes associated with groundwater overdraft are highly variable from place to place, then it may be possible for fissures to form in response to relatively small amounts of subsidence. If, on the other hand, the near-surface strata are homogeneous and there is little spatial variation in effective stress, then it may be possible for a relatively large amount of subsidence to occur without producing fissures. At this stage, we are not able to quantify "large" and "small".

Our assumption of constant plate thickness means that the magnitudes of bending moment highs and lows will be relatively uniform, decreasing only a little towards the center of the plate. Therefore, one would expect to find opening mode cracks (or fissures in the subsiding basin) distributed over the upper surface of the plate in a checkerboard fashion, mirroring the bending moment distribution. In the Mimbres Basin, however, fissures first

appeared near the center of the basin and have slowly moved outward in pace with the groundwater cone of depression. There are at least two factors that may contribute to this discrepancy. First, the increase in effective stress in a real subsiding basin will be proportional to the change in hydraulic head (in addition to the compressibility of the dewatered aquifer material) which would tend to concentrate stresses towards the center of the basin. Second, vadose zone geometry enters the expression for flexural rigidity as the cube of the plate thickness. For a given amount of deflection, therefore, bending moments in a thicker plate will be much greater than those in a thinner plate and, conversely, a thicker plate will be much more resistant to bending than will a thinner plate. The equation governing the deflection of a plate with variable thickness are substantially more complicated than that for a plate of constant thickness and, as a result, the interrelationship between changing plate thickness and effective stress could not be addressed within the time limitations of this study. This may be a fruitful line of inquiry for future analyses.

CONCLUSIONS

1) The tiltmeters successfully documented deformation near the fissure. Tiltmeters are relatively inexpensive for the data received and are easier to install and maintain than some other types of deformation instrumentation. However, they are limited, in that tiltmeters only measure rotation and give no indication of actual displacement.

2) Short-term cyclic variations seen in the tiltmeter and water level data result from a combination of both earth tide and barometric fluctuation effects.

3) The signals of both tiltmeters and the piezometers contain both diurnal and semi-diurnal cycles. Spectral analysis of short-term tiltmeter records clearly reveals the presence of 12 and 24 hour cycles. Both short- and long-term piezometers records are also dominated by the same 12 and 24 hour cycles. At the time this report was prepared, not enough data had been collected to properly analyze longer-term harmonics with wavelengths of months to years.

4) The signal from short-term tiltmeter and piezometer records can be explained by a combination of physically reasonable harmonics that include the effects of solid earth tides, barometric fluctuations, and both seasonal and long-term groundwater level decrease. Residual signals reveal no obvious remaining harmonic components. Because the site instrumentation did not include a barometer, further deconvolution of barometric and tidal cycles appears to be impossible.

5) Long-term tiltmeter behavior is dominated by tilt patterns that are not yet fully understood. Long-term groundwater level fluctuations should have some effect on the fissure, but the data suggests that additional effects, for example stress concentrations around local structural and stratigraphic irregularities or basin-wide flexure, may be partly responsible for complicated long-term tilt patterns. Installation of tiltmeters in shallow cased boreholes may have also contributed to the problem, by averaging tilt values over the length of the casing and possibly incorporating surface noise into the tiltmeter records. Complexities in the long-term records may become understandable as additional data are collected.

6) Plane strain caused by draping of sediments over irregularities does not provide a straightforward explanation of the long-term tilts observed at the Mimbres Basin earth fissure. Some aspects of short-term records can, however, be interpreted in terms of draping of alluvial materials caused by differential compaction.

7) The in-line tiltmeter array used in this study was designed specifically to measure plane-strain deformation perpendicular to the fissure, and is poorly configured to measure deformation with components both parallel and perpendicular to the fissure. Future fissure monitoring studies must be designed to measure both components of deformation both perpendicular and parallel to the trace of the fissure. If plane-strain is an *a priori* assumptionand movement is recorded in only one direction, for example using only extensometers installed perpendicular to a fissure, then it will be impossible to infer that anything other than plane-strain deformation

occurred. Techniques such as the use of quadrilateral arrays of surface monuments may be useful.

8) Tilts in a thin elastic plate subjected to complicated loading patterns, which may be analogous to surface deformation above a compacting aquifer containing local structural and stratigraphic irregularities, are highly variable and not unlike those observed in the field. Thus, there may be a qualitative mechanical explanation for the complicated tilt patterns observed at the Mimbres Basin site. Additional work, however, will be required before a quantitative understanding is possible.

REFERENCES

Applied Geomechanics. 1991. *User's Manual, Model 722 Borehole Tiltmeters.* Santa Cruz, California: Applied Geomechanics, Inc.

Baum, R.L., Johnson, A.M., and Fleming, R.W. 1988. *Measurement of slope deformation using quadrilaterals.* U.S. Geol. Survey Bulletin 1842-B.

Boling, J.K. 1984. Earth-fissure movements in south-central Arizona, U.S.A. In *Land Subsidence.* Edited by A. I. Johnson, 757-766. Wallingford, Oxforshire, U.K.: IAHS Press.

Bredehoeft, J.D. 1967. Response of well-aquifer systems to earth tides. *J. Geophys. Res.* 72:3075-3087.

Carpenter, M.C., 1986, *Water-level declines, land subsidence, and specific compaction near Apache Junction, South-Central Arizona*: U.S. Geol. Survey Water-Resources Investigations Report 86-4071.

_____.1988. *Land-surface deformation near the Picacho earth fissure, south-central Arizona, 1980-1984.* U.S. Geol. Survey Open-file Report 88-97.

Clemons, R.E. 1985. *Geology of South Peak quadrangle, Luna County, New Mexico.* New Mexico Bureau of Mines and Mineral Resources, Geologic Map 59, 1:24,000.

_____. 1986. Petrography and stratigraphy of the Seville-Trident exploration wells near Deming, New Mexico. *New Mexico Geol.* 8:5-11.

_____. 1992. *Geology of the Florida Mountains, southwestern New Mexico.* New Mexico Bureau of Mines and Mineral Resources, Memoir 43. In press.

_____, and G.H. Mack. 1988. Geology of southwestern New Mexico. In *Cretaceous and Laramide Tectonic Evolution of Southwestern New Mexico.* Edited by G.H. Mack,T.F. Lawton, and S.G. Lucas, 45-57. Socorro, New Mexico: New Mexico Geological Society 39th Annual Field Conference Guidebook.

Conover, C.S., and D.P. Akin. 1942. Progress report on the ground-water supply of Mimbres Valley, New Mexico, 1938-1941. In *14th and 15th Biennial Reports of the State Engineer of New Mexico.* 235-282.

Contaldo, G.J. 1989. *Earth fissures and land subsidence near Deming, New Mexico.* M.S. thesis, Department of Earth Sciences, New Mexico State University, Las Cruces, New Mexico.

_____, and J.E. Mueller. 1991. Earth fissures of the Mimbres Basin, southwestern New Mexico. *New Mexico Geol.* 13:69-74.

Darton, N.H. 1914. *Underground Water of Luna County, New Mexico.* U.S. Geol. Survey, Water Supply Paper 345-C, 25-40.

_____. 1916. *Geology and Underground Water of Luna County, New Mexico.* U.S. Geol. Survey, Bulletin 618.

Das, B.M. 1983. *Advanced Soil Mechanics.* Washington, D.C.: Hemisphere Publishing.

Domenico, P.A., and F.W. Schwartz. 1990. *Physical and Chemical Hydrology.* New York: John Wiley and Sons.

Epstein, V.J. 1987. *Hydrologic and geologic factors affecting land subsidence near Eloy, Arizona.* U.S. Geol. Survey Water-Resources Investigations Report 87-4143.

Fiedler, A.G. 1927. Report on a reconnaissance of the ground-water area of the Mimbres Valley, Luna County, New Mexico. *Eighth Biennial Report of the State Engineer of New Mexico.* 159-171.

Friesen, R.L. 1992. *Cyclic flexure of surficial strata near an earth fissure in the Mimbres basin, southern New Mexico.* M.S. thesis, Department of Mineral and Environmental Engineering, New Mexico Institute of Mining and Technology, Socorro.

Gieske, A. 1986. On phase shifts in periodic well fluctuations. *Geophys. J. R. Astron. Soc.* 86:789-799.

Gile, L.H., J.W. Hawley, and R.B. Grossman. 1981. *Soils and geomorphology in the Basin and Range area of southern New Mexico - Guidebook to the Desert Project.* New Mexico Bureau of Mines and Mineral Resources, Memoir 39.

Hamming, R.W. 1986. *Numerical Methods for Scientists and Engineers.* New York: Dover Publications, Inc.

Haneberg, W.C. 1992. Drape folding of compressible elastic layers— I. Analytical solutions for vertical uplift. *Jour. Struct. Geol.* 14: 713-721.

Haneberg, W.C. 1993. Drape folding of compressible elastic layers— II. Matrix solution for two-layer folds. *Jour. Struct. Geol.* 15. In press.

_____, C.B. Reynolds, and I.B. Reyolds. 1991. Geophysical characterization of soil deformation associated with earth fissures near San Marcial and Deming, New Mexico. In *Land Subsidence.* Edited by A.I. Johnson, 271-280. Wallingford, Oxforshire, U.K.: IAHS Press.

_____, and R.L. Friesen. 1992. Diurnal groundwater level and deformation cycles near an earth fissure in the subsiding Mimbres Basin, New Mexico. In *Proceedings of the 35th Annual Meeting of the Association of Engineering Geologists.* Edited by M.L. Stout, 46-52. Assoc. of Engr. Geol.

Helm, D.C. 1992. Hydraulic forces that play a role in generating fissures at depth. In *Proceedings of the 35th Annual Meeting of the Association of Engineering Geologists.* Edited by M.L. Stout, 7-16. Assoc. of Engr. Geol.

Holzer, T.L. 1984. Ground failure induced by ground-water withdrawal from unconsolidated sediment. In *Man-Induced Land Subsidence.* Edited by T.L. Holzer, 67-105. Boulder, Colorado: Geological Society of America, Reviews in Engineering Geology VI.

_____, and E.H. Pampeyan. 1981. Earth fissures and localized differential subsidence. *Water Resour. Res.* 17: 223-227.

Hsieh, P.A., J.D. Bredehoeft, and S.A. Rojstaczer. 1988. Response of well aquifer systems to earth tides: problem revisited. *Water Resour. Res.* 24:468-472.

Jachens, R.C., and T.L. Holzer. 1979. Geophysical investigations of ground failure related to ground-water withdrawal - Picacho Basin, Arizona. *Ground Water.* 17:574-585.

_____, and T.L. Holzer. 1982. Differential compaction mechanism for earth fissures near Casa Grande, Arizona. *Geol. Soc. Am. Bull.* 93:998-1012.

Keaton, J.R., and J.J. Miller. 1992. Dry Lake Valley earth fissure system, Clark County, Nevada. In *Proceedings of the 35th Annual Meeting of the Association of Engineering Geologists.* Edited by M.L. Stout, 129-133. Assoc. of Engr. Geol.

Keaton, J.R., and R.J. Shlemon. 1991. The Fort Hancock earth fissure system, Hudspeth County, Texas: uncertainties and implications. In *Land Subsidence.* Edited by A.I. Johnson, 281-290. Wallingford, Oxforshire, U.K.: IAHS Press.

Larson, Michael L., and T.L. Pewe. 1986. Origin of land subsidence and earth fissuring, northeast Phoenix, Arizona. *Bull. Assoc. Eng. Geol.* 23:139-165.

Lofgren, B.E. 1971. Significant role of seepage stresses in compressible aquifer systems. *EOS, Trans. Am. Geophys. Union.* 52:832.

_____, 1975. *Land subsidence and tectonism, Raft River Valley, Idaho.* U.S. Geol. Survey Open-file Report 75-585.

_____, 1976. *Land subsidence and aquifer-system compaction in the San Jacinto Valley, Riverside County, California - a progress report.* U.S. Geol. Survey Jour. Res. 4:9-18.

Lomb, N.R. 1976. Least-squares frequency analysis of unequally spaced data. *Astrophys. Space Sci.* 39:447-462.

McLean, J.S. 1977. *Hydrologic maps and data in the Mimbres Basin.* U.S. Geol. Survey Open-file Report 77-314.

Melchior, P. 1966. *The Earth Tides*. New York: Pergamon Press.

Menke, W., and D. Abbot. 1990. *Geophysical Theory*. New York: Columbia University Press.

Mueller, J.E. 1988. Climate of southwestern New Mexico. In *Cretaceous and Laramide Tectonic Evolution of Southwestern New Mexico*. Edited by G.H. Mack, T.F. Lawton, and S.G. Lucas, 28-29. Socorro, New Mexico: New Mexico Geological Society 39th Annual Field Conference Guidebook.

Neal, J.T., A.M. Langer, and P.F. Kerr. 1968. Giant desiccation polygons of Great Basin Playas. *Geol. Soc. Am. Bull.* 79: 67-90.

Neher, R.E., and W.A. Buchanan. 1980. *Soil Survey of Luna County, New Mexico*. U.S. Dept. of Agriculture, Soil Conservation Service.

New Mexico Interstate Stream Commission, and New Mexico State Engineer Office. 1974. *County Profile, Luna County, Water Resources Assessment for Planning Purposes.*

Peterson, D.E. 1962. Earth fissuring in the Picacho area, Pinal County, Arizona. M.S. thesis, University of Arizona, Tucson, Arizona.

Pewe, T.L. 1990. Land subsidence and earth-fissure formation caused by groundwater withdrawal in Arizona; A review. In *Groundwater Geomorphology: The Role of Subsurface Water in Earth-Surface Processes and Landforms.* Edited by C.G. Higgins, and D.R. Coates, 219-233. Geol. Soc. Am. Special Paper 252.

Press, W.H., and S.A. Teukolsky. 1988. Search algorithm for weak periodic signals in unevenly spaced data. *Computers in Physics.* 2:77-82.

Poland, J.F. 1984. *Guidebook to Studies of Land Subsidence Due to Ground-Water Withdrawal.* UNESCO Studies and Reports in Hydrology 40.

Ritzi, R.W., S. Sorooshian, and P.A. Hsieh. 1991. The estimation of fluid flow properties from the response of water levels in wells to the combined atmospheric and earth tide forces. *Water Resour. Res.* 27:883-893.

Robinson, T.W. 1939. Earth-tides shown by fluctuations of water-levels in wells in New Mexico and Iowa. *Trans. Am. Geophys. Union.* 20:656-666.

Rojstaczer, S. 1988. Determination of fluid flow properties from the response of water levels in wells to atmospheric loading. *Water Resour. Res.* 24:1927-1938.

_____, and D.C. Agnew. 1989. The influence of formation material properties on the response of water levels in wells to earth tides and atmospheric loading. *J. Geophys. Res.* 94:12,403-12,411.

_____, and F.S. Riley. 1990. Response of the water level in a well to earth tides and atmospheric loading under unconfined conditions. *Water Resour. Res.* 26:1803-1817.

Sandoval, J.P., and S.R. Bartlett. 1991. Land subsidence and earth fissuring on the Central Arizona Project, Arizona. In *Land Subsidence.* Edited by A.I. Johnson, 249-260. Wallingford, Oxforshire, U.K.: IAHS Press.

Sato, T., K. Daito, and K. Ueshita. 1984. Analysis of land subsidence due to withdrawal of groundwater in the Nobi Plain. In *Land Subsidence.* Edited by A.I. Johnson, 89-99. Wallingford, Oxforshire, U.K.: IAHS Press.

Scargle, J.D. 1982. Studies in astronomical time series analysis II. Statistical aspects of spectral analysis of unevenly spaced data. *Astrophys. J.* 263:835-853.

Schumann, H.H., L.S. Cripe, and R.L. Laney. 1984. Land subsidence and earth fissures caused by groundwater depletion in southern Arizona, U.S.A. In *Land Subsidence*. Edited by A.I. Johnson, 841-851. Wallingford, Oxforshire, U.K.: IAHS Press.

Seager, W.R. 1983. Laramide wrench faults, basement-cored uplifts and complementary basins in southern New Mexico. *New Mexico Geol.* 5:69-76.

_____. 1992. *Geologic map of the southwest quarter of the Las Cruces and northwest part of the El Paso $1^0 \times 2^0$ sheets.* New Mexico Bureau of Mines and Mineral Resources, Geologic Map 60, 1:125,000. In press.

Theis, C.V. 1939. Progress report on the ground-water supply of the Mimbres Valley, New Mexico. In *12th and 13th Biennial Report of the State Engineer of New Mexico.* 131-152.

Turk, L.J., 1975. Diurnal fluctuations of water tables induced by atmospheric pressure changes. *J. of Hydrology.* 26:1-16.

van der Kamp, G., and J.E. Gale. 1983. Theory of earth tide and barometric effects in porous formations with compressible grains. *Water Resour. Res.* 19:538-544.

Weeks, E.P. 1979. Barometric fluctuations in wells tapping deep unconfined aquifers. *Water Resour. Res.* 15: 1167-1176.

White, W.N. 1929. Preliminary report on the ground-water supply of Mimbres Valley, New Mexico. *Ninth Biennial Report of the State Engineer of New Mexico.* 131-152.

Wilson, B. 1986. *Water Use in New Mexico in 1985.* New Mexico State Engineer Office Technical Report 46.

_____. 1992. *Water Use by Categories in New Mexico Counties and River Basins, and Irrigated Acreage in 1990.* New Mexico State Engineer Office Technical Report 47.

APPENDIX A

Haneberg, W.C. and Friesen, R.L. 1992. Diurnal groundwater level and deformation cycles near an earth fissure in the subsiding Mimbres Basin, New Mexico. In *Proc. 35th Ann. Mtg. Assoc. Engrg. Geol., Long Beach, California, Oct. 2-9, 1992.* Edited by M.L. Stout, 46-52.

DIURNAL GROUNDWATER LEVEL AND DEFORMATION CYCLES NEAR AN EARTH FISSURE IN THE SUBSIDING MIMBRES BASIN, NEW MEXICO

William C. Haneberg and Robert L. Friesen
New Mexico Bureau of Mines and Mineral Resources,
New Mexico Institute of Mining and Technology, Socorro NM 87801

Abstract

Short-term records from four 0.1 μrad borehole tiltmeters and two piezometers installed near an earth fissure in the Mimbres Basin of southern New Mexico contain evidence of distinct diurnal deformation and groundwater level cycles with dilation of $\Delta \approx 7.8\times10^{-8}$. Longer-term components are apparent in the data as well. Fourier regression analysis using selected harmonics shows that up to 99.7% of the variability in short-term tiltmeter records can be explained using a combination of 12 hr 25 min, 24 hr, 14 day, and 365 day components. Comparison of the short-term data with well hydrographs from other parts of the basin suggests that the 365 day component is a reflection of seasonal irrigation pumping cycles. The three shorter harmonics, however, are most easily interpreted as the effects of earth tides and barometric fluctuations. Although more data are needed to properly quantify long-term trends, preliminary results suggest that displacement vectors on either side of the fissure are consistent with a model of localized symmetric draping over a buried channel deposit and regional basinward flexure.

Introduction

Large earth fissures, related both in space and time to groundwater overdraft, have been documented throughout the Mimbres Basin of southern New Mexico. Interpretation of previous gravity and shallow seismic reflection profiles suggested that one of these fissures is underlain by both a relatively incompressible coarse-grained channel fill deposit and a set of three down-to-basin buried normal faults. In order to better understand the stresses and displacements associated with fissuring in a subsiding groundwater basin, we installed sensitive biaxial borehole tiltmeters and piezometers on either side of one Mimbres Basin earth fissure. In this paper, we describe and begin to analyze both short (days) and long (tens and hundreds of days) deformation and water level cycles. Future papers will document long term fluctuations in some detail, and also compare the observed deformation with that calculated for an elastic layer draped over a rigid elliptical body.

Geologic Setting

The Mimbres Basin lies within the Basin and Range physiographic province (Gile, et al., 1981). The basin lies within a down-thrown block created by movements associated with mid-Miocene and younger extensional faulting, which is also responsible for the uplift of the Florida Mountains that border the basin on the east (Clemons and Mack, 1988). The subsiding basin was initially filled with Eocene to Miocene volcanic rocks, which also comprise the basin's bedrock floor (Clemons, 1986). Overlying this material are upper Tertiary to Holocene alluvial sediments that can be divided into two units: the lower unit is finer grained and contains primarily reddish clays indicative of alluvial fan and playa deposits of mid-Pleistocene age and older whereas the upper unit consists of interbedded lenses of gravels, sands, silts and clays that are representative of delta deposits derived from the Mimbres River (Contaldo and Mueller, 1991). The total thickness of sediments within the basin is approximately 1000 m (Clemons, 1986).

Previous Fissure and Subsidence Studies

Contaldo (1989) and Contaldo and Mueller (1991a,b) have documented the existence of earth fissures at 13 locations throughout the Mimbres Basin, most of which lie above a cone of drawdown 10 to 20 km south of Deming, New Mexico (Fig. 1). Although a steady drop in groundwater levels, which have been recorded and mapped periodically since the pioneering work of Darton (1917), is the obvious driving mechanism, the location of the fissures is problematic.

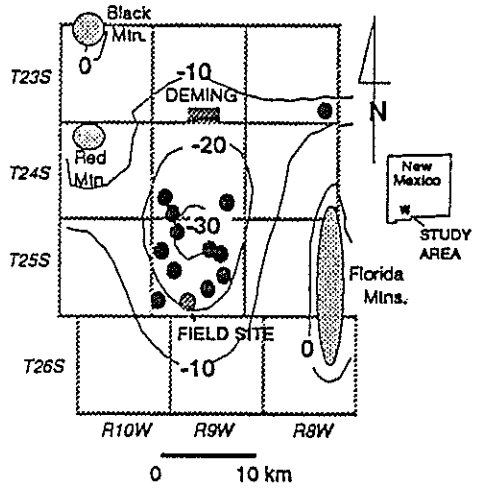

Figure 1.– Water level drawdown between 1910 and 1987 and fissure locations in the Mimbres Basin, New Mexico. Drawdown contours are in meters, and the fissure discussed in this paper is denoted by the gray circle. Data for this figure are from Contaldo and Mueller (1991b).

The Mimbres Basin fissures are morphologically similar to those reported in many other parts of the western United States (e.g., Holzer, 1984), which are typically associated with differential compaction of sediments over shallow bedrock irregularities along basin margins. However, the concentration of fissures near the center of the basin, where the thickness of unconsolidated fill probably exceeds 1000 m (Clemons, 1986), and compaction over bedrock structures is unlikely. In an attempt to better understand this paradox, Haneberg et al. (1991) conducted shallow seismic reflection and gravity surveys across a Mimbres Basin fissure located in NE/4, NE/4, Sec. 32, T25S, R9W. They inferred the presence of both a shallow stratigraphic irregularity– more than likely a buried channel fill deposit– and several down-to-basin normal faults beneath a 75 m deep angular unconformity. Although these faults have no surface expression and are not identifiable on the reflection profile, refraction processing and velocity contouring of the seismic data showed that low velocity anomalies extend upwards from the faults to within 10 m of the ground surface.

Instrumentation

Near-surface deformation is being monitored using four Applied Geomechanics model 722 biaxial borehole tiltmeters, which were installed on each side of the fissure in December 1991 (Fig. 2). Each tiltmeter has selectable high and low gains, with a high gain sensitivity of 0.1 µrad and range of ±250 µrad. Temperature sensors, with a sensitivity of 0.1° C, are also built into the tiltmeters. However, the temperature sensors are intended primarily to verify that the tiltmeters remain within their operation range, rather than to monitor soil temperatures. The surrounding steel casings, in particular, have a high thermal conductivity and no doubt have an effect on tiltmeter temperatures. Each tiltmeter was sanded into place at the bottom of a 20.3 cm steel casing, which had been driven into a pre-drilled air rotary borehole (Fig. 3). Following the manufacturer's instructions, each tiltmeter was suspended from a rope while sand was poured in and tamped with a tapered probe until the instrument was close to vertical. Azimuths of the two tilt axes were recorded for later use in rotating the data.

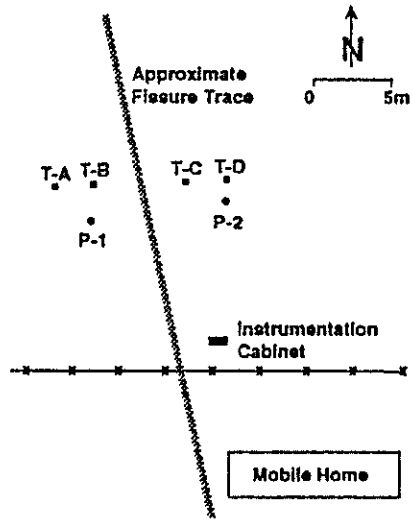

Figure 2.– Schematic site map showing the earth fissure trace, instrument locations, and a nearby mobile home and fence line. The fissure appears as a series of isolated holes south of the instruments, and as a highly eroded gully up to 2 m deep immediately north of the instruments. T-A, T-B, T-C, and T-D represent the four tiltmeters, whereas P-1 and P-2 are the two piezometers. The outer tiltmeters, A and D, are shallow (≈2 m) and the inner tiltmeters, B and C, are deep (≈5 m).

One piezometer was installed on each side of the fissure, using 10 cm PVC casing with a 6.1 m screened interval, pea gravel pack, and bentonite seal. Rotary rig circulation was lost during the drilling of both holes, but was regained after the mud was thickened with bentonite. Although fluid levels fell when circulation was lost, the boreholes were never completely drained.

Both piezometer holes are about 49 m deep, with a static water level at approximately 42.4 m beneath the ground surface. Coarse sand and gravel cuttings were recovered at about 15 m, confirming the presence of the coarse-grained, relatively incompressible buried channel deposit inferred from earlier seismic profiles.

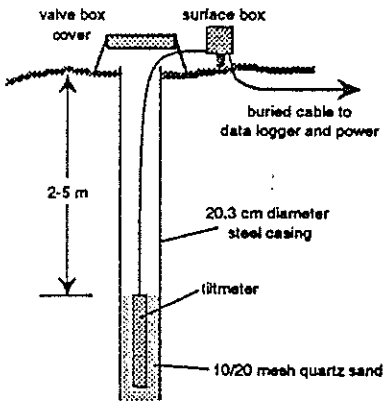

Figure 3.– Schematic diagram of typical tiltmeter installation. The steel casing was jacked into an air-rotary borehole. Each tiltmeter was suspended from a rope while 10/20 mesh sand was poured into the borehole and tamped to center each instrument so that tiltmeter output was near the middle of the ±2500 mV (±250 μrad) data logger input range.

Each piezometer was fitted with a Druck PDCR 830 water level transducer with a range of 0 to 210 kPa (0 to 21.41 m water), and static water levels in the two piezometers and a nearby domestic well are checked manually during visits to the field site.

Data are collected hourly by a battery-powered Campbell CR-10 data logger with solar recharging, which can store up to five weeks of data. The data logger has only 12 analog inputs, so a multiplexer was added to accommodate the 14 data channels required for four tiltmeters (each with 2 tilt and 1 temperature output channel) and two transducers (each with 1 pressure output channel). Data are transferred from the data logger to an MS-DOS portable personal computer using an RS-232 interface, written to a floppy disk, and then read into a UNIX workstation hard disk for analysis and plotting. An in-house C language program is used to transform the data logger file by removing channel numbers, converting millivolt outputs to tilt, temperature, and water pressure, and rotating the tilt values onto and east-west and north-south coordinate system. The result is an ASCII file containing values that can be read into any number of commercially available scientific data analysis programs.

Observations

When this paper was written, about 52 days of data had been collected in discontinuous increments between January 13 and March 21, 1992. Gaps in the data are due primarily to electrical problems in the solar recharging loop, which have since been corrected. Although the tiltmeters performed well, with only occasional spurious data points, the two pressure transducers began to malfunction several weeks after installation. In order to remain within the page limitations of this volume, we will illustrate our observations using tilt and water level data collected between January 25 and 30, 1992. Although longer strings of continuous data are available, we have chosen a five day period because diurnal fluctuations tend to be obscured by longer term trends if longer records are examined. In order to eliminate the effects of initial tilt, which was different for each instrument, we elected to plot differential curves showing the change in tilt between January 25 and 30.

Tilts.– Changes in east-west tilt and north-south tilt for tiltmeter A are plotted, respectively, in Figures 4 and 5. In both cases, short-term (12 and 24 hr) fluctuations are superimposed upon nearly linear, long term changes in tilt. Over the five day period of record, the two shallow (A and D) instruments tilted away from each other and the two deep (B and C) instruments tilted towards each other in an east-west plane nearly perpendicular to the fissure (Fig. 6). In a north-south plane during the same time period, tiltmeter A moved to the north, tiltmeter B remained very nearly stationary, and tiltmeters C and D both moved towards the north. Whereas the accumulated tilt over a five day period is on the order of several μrad, daily cycles are on the order of ±0.1 μrad. Although the amount of strain data that can be gleaned from tiltmeter records is limited, we can recast the tilt angles in terms of differential horizontal displacement between the top and the bottom of a tiltmeter. For a 0.78 m long tiltmeter, 0.1 μrad tilt corresponds to a displacement gradient of $\delta u/\delta y \approx 7.8\times10^{-8}$ between the top and the bottom of the tiltmeter. If we further assume that $\delta v/\delta x = 0$ (primarily because this cannot be recorded using tiltmeters) the average shear strain (e.g., Jaeger and Cook, 1969, p. 38) along the length of the tiltmeter is about $\Gamma_{xy} = 0.5(\delta u/\delta y + \delta v/\delta x) \approx 3.9\times10^{-8}$. Extending this analogy to the second horizontal direction, we estimate diurnal dilation due solely to differential horizontal displacement to be on the order of $\Delta \approx 7.8\times10^{-8}$.

Groundwater Levels.– Daily groundwater level fluctuations during the period of observation were on the order of 3 cm, and are superimposed upon a long-term decrease of approximately 1 cm between January 25 and 30 (Fig. 7). Unlike the tiltmeter records described above, the daily harmonic water level changes components are larger than the combined long term harmonic and monotonic components. Water level fluctuation waveforms during this period consist of repeated doublets, with a smaller peak in the early morning and a larger peak in the early afternoon.

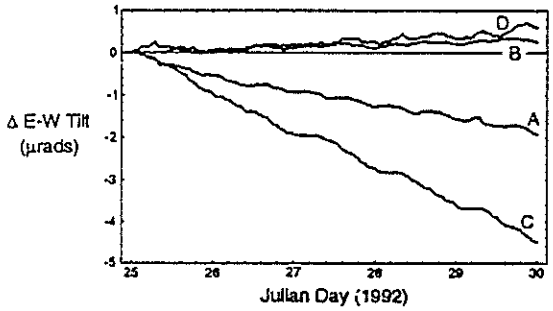

Figure 4.– Hourly changes in east-west tilt of tiltmeters A, B, C, and D, recorded between January 25 and 30, 1992. Positive values indicated tilting towards the east, and negative values indicate tilting towards the west. All tiltmeters were set to high gain during this period. Daily fluctuations are typically less than long-term trends for record lengths of several days.

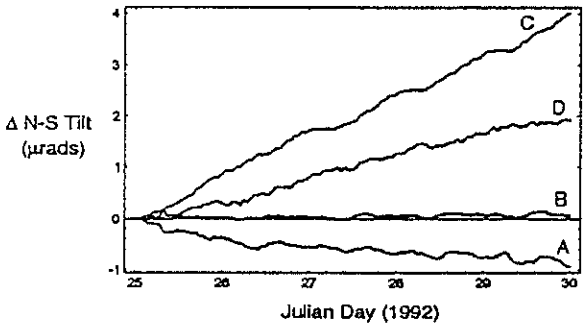

Figure 5.– Hourly changes in north-south tilt of tiltmeters A, B, C, and D, recorded between January 25 and 30, 1992. Positive values indicated tilting towards the north, and negative values indicate tilting towards the south. All tiltmeters were set to high gain during this period. As in Figure 4, daily fluctuations are typically less than long-term trends for record lengths of several days.

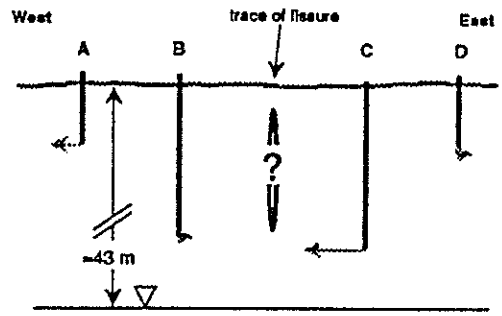

Figure 6.– Schematic diagram illustrating net east-west tilts between January 25 and 30. Subsurface fissure geometry is unknown, and the static water table is approximately 43 m deep. The two shallow outer tiltmeters tilted away from the fissure, whereas the two deep inner tiltmeters tilted towards the fissure (as projected downward from its surface trace). The localized tilt component, which is centered around the fissure, appears to be superimposed upon a nearly constant westward component.

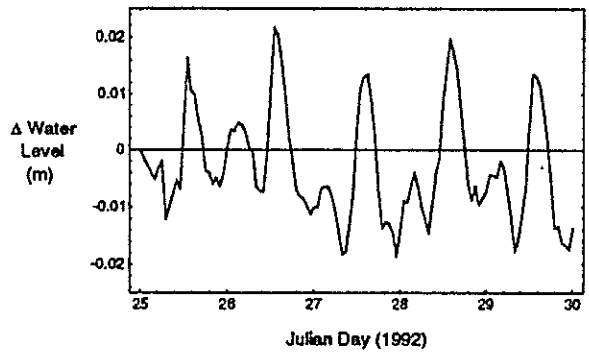

Figure 7.– Hourly changes in piezometer P-1 water levels recorded between January 25 and 30, 1992. Daily fluctuations are typically much greater than long-term trends for record lengths of several days.

Harmonic Analysis.– In conventional Fourier analysis, the power spectrum for a large number of harmonics is calculated in hope of discovering periodic components hidden in time series data. Fast algorithms (e.g., Press et al., 1988) have been developed for certain special situations, but they are generally restricted to unbroken strings of data that are equally spaced in time. Because our tiltmeter records contain a few obviously erroneous data that were removed prior to analysis, creating gaps in otherwise continuous records, these methods are not directly applicable to the problem at hand. The amplitudes of diurnal tilt cycles are small compared to to the long-term changes when data for

more than a few days are compared, which presents problems for standard Fourier transform methods as well. Therefore, we have adopted an alternative method of selective harmonic analysis. Instead of exhaustively analyzing many wavelengths or frequencies in hope of discovering some hidden periodicity, a limited number of physically reasonable wavelengths are specified *a priori* and harmonic coefficients are calculated using standard least-squares methods. Neither this nor other forms of harmonic analysis can prove, in a rigorous sense, the reality of any calculated periodicity, no matter how strong its spectral power. The best that can be done is to fail to reject the null hypothesis, which is that the waveform created by the selected harmonics is not substantially different from the observed waveform.

After plotting and visually inspecting several days' worth of data, we selected 12 and 24 hr wavelengths for analysis. Mimbres Basin well hydrographs, described above, contain distinct annual cycles and a long-term monotonic component, so we also included a 365 day harmonic and linear monotonic terms. The possibility of earth tide cycles prompted the addition of a 14 day lunar component, and the 12 hr component was changed to a 12 hr 25 min component. We fitted the observed tiltmeter data, less the spurious data points, using a target function of the form

$$\begin{aligned} y_{pred} = {} & m\,t + A_{0.52}\cos(2\pi t/0.52) \\ & + B_{0.52}\sin(2\pi t/0.52) \\ & + A_1\cos(2\pi t/1) \\ & + B_1\sin(2\pi t/1) \\ & + A_{14}\cos(2\pi t/14) \\ & + B_{14}\sin(2\pi t/14) \\ & + A_{365}\cos(2\pi t/365) \\ & + A_{365}\sin(2\pi t/365) \end{aligned} \qquad (1)$$

in which y_{pred} is the equation of the best-fit line and the denominators in the trigonometric terms are the four selected wavelengths expressed in days. The eight A and B coefficients and m were estimated by standard least-squares methods, using the computer program Mathematica (Wolfram, 1991). The spectral power of each wavelength is given by $A^2 + B^2$, and the slope of the long-term monotonic component is given by m.

Observed data and best-fit lines for the east-west component of tiltmeter A data and P-1 water level data are plotted for comparison in Figs. 8 and 9. These are the actual values, and not differential values as used in Figs. 4, 5, and 7. The goodness-of-fit for the tiltmeter curve, $r^2 = 0.997$, is exceptionally high, whereas the goodness-of-fit for the piezometer curve, $r^2 = 0.683$, is barely acceptable. Residual values for both curves appear to be stationary and normally distributed about zero (Figs. 10 and 11), suggesting that no strong harmonics have been excluded from eqn. 1.

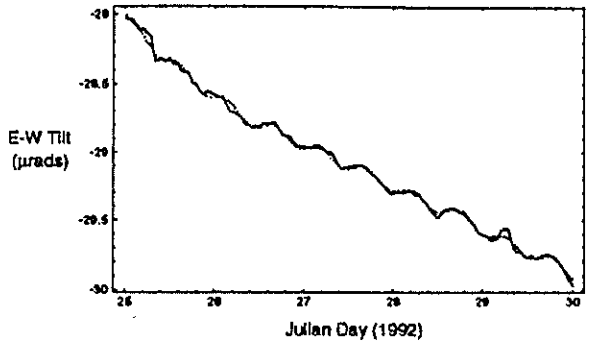

Figure 8.– Observed hourly east-west tilt and best fit line (eqn. 1). Observed values are shown in black, and the best fit line is shown in gray. Goodness-of-fit for this example is $r^2 = 0.997$.

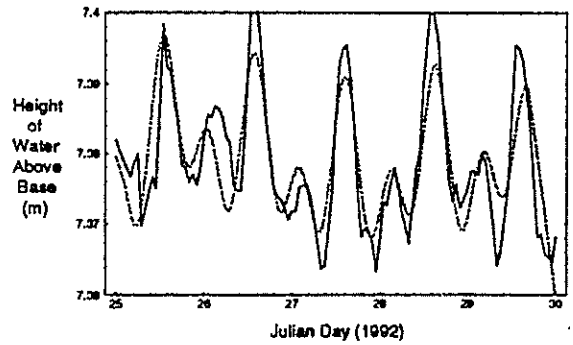

Figure 9.– Observed P-1 hourly water level changes and best fit line calculated using eqn. 1. Observed values are shown in black, and the best fit line is shown in gray. Goodness-of-fit for this example is $r^2 = 0.683$.

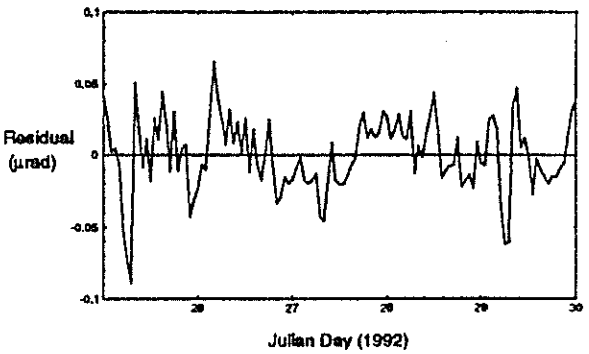

Figure 10.– Residual curve showing differences between the observed and best-fit T-A east-west tilt curves shown in Fig. 8.

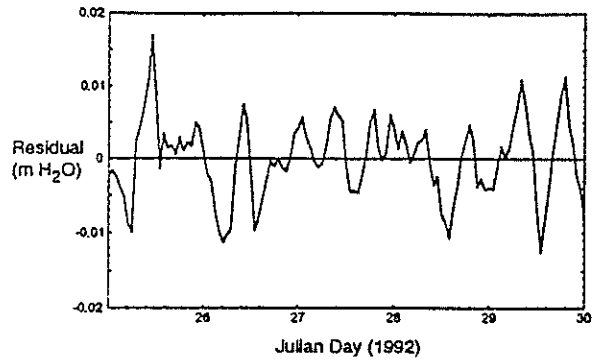

Figure 11.– Residual curve showing differences between the observed and best-fit P-1 water level curves shown in Fig. 9.

Discussion

High-resolution biaxial borehole tiltmeters, installed primarily to monitor seasonal groundwater level and deformation cycles, also provide evidence of micrometer-scale diurnal movements near an earth fissure in the subsiding Mimbres Basin. Both tilt and water level records exhibit diurnal and semi-diurnal cyclicity. Long term components, however, dominate the tiltmeter records whereas short term components dominate the piezometer records. The results of this localized study also suggest that basin-wide tiltmeter networks may provide a relatively inexpensive and extremely accurate means of regional land subsidence monitoring, especially in cases where surface deformation is the primary concern. In cases where documentation of vertical compaction, especially over specified stratigraphic intervals, is of concern, traditional vertical borehole extensometers may be preferred.

There is correspondence between daily groundwater level maxima and eastward (towards the fissure for tiltmeter A) tilt maxima, and well as groundwater level minima and westward (away from the fissure for tiltmeter A) maxima. Likewise, there is a systematic pattern of net (long-term) tilts in the January 25-30 data described in this paper. Both the long and short term patterns are qualitatively similar to the displacement of an elastic beam draped over a rounded protrusion, such as the buried channel inferred during previous geophysical work and confirmed during drilling at the study site. It would appear, then, that the observed near-surface tilts are the result of periodically changing vertical effective stress at depth.

Harmonic analysis, performed by least-squares fitting of selected waveforms to several days' worth of data, shows that an extremely high percentage (up to 99.7%) of the variability in tiltmeter records can be explained by a combination of 12 hr 25 min, 24 hr, 14 day, and 365 day harmonics superimposed upon a monotonic linear component. Although the similar cycles are obvious in water level fluctuation curves, goodness-of-fit values were lower when the same set of harmonics was fitted to piezometer data. The legitimacy of fitting long-term harmonics to short-term data is addressed further on in this discussion.

The most obvious cause of diurnal and semi-diurnal cycles is a combination of earth tides and barometric fluctuations, which have been observed and analyzed in both confined and unconfined aquifers (e.g., Bredehoeft, 1967; van der Kamp and Gale, 1983; Rojstaczer and Agnew, 1989). Rojstaczer and Riley (1990), in particular, analyzed tidally and barometrically induced water level fluctuations in unconfined aquifers. They presented data from a shallow (18 m depth to water) well in fractured rock near Parkfield, California, that contained distinct 2-4 cm semi-diurnal water level doublets, as well as cuspate diurnal fluctuations attributed to barometric cycles. We have no detailed barometric data for comparison with our short-term tilt and water level records, and therefore cannot isolate the effects of meteorological variability. Our estimated dilation of 7.8×10^{-8} has the same order of magnitude as the theoretical value of 10^{-8} usually attributed to earth tides (e.g., Rojstaczer and Riley, 1990).

The fitting of harmonics with wavelengths longer than the time of observation presents some problems. On one hand, the long-term components present in the tiltmeter data must somehow be quantified in order to isolate the much weaker diurnal components. One might arbitrarily subtract out a linear trend from the field data in order to analyze the details of short term cyclicity, but the *a priori* specification of annual and fortnightly water cycles has more physical justification than a simple linear trend. The resulting regression lines, especially for tiltmeter data, have both extremely high goodness-of-fit values and randomly distributed, apparently stationary residuals. When extrapolated beyond the period of record, however, the best-fit curve illustrated in Figure 9 predicts annual water level cycles of ± 500 m and a long term water level decrease of about 3 km/yr. For comparison, Contaldo (1989) documented annual cycles with amplitudes on the order of a meter and long term monotonic decreases on the order of several tens of centimeters per year. If the linear monotonic term is excluded from the regression model, the annual water level fluctuations decrease to a

more reasonable (but still incorrect) estimate of ±7.4 m. Ironically, the short term goodness-of-fit estimate is also *decreased* by several percent when the monotonic term is removed. Although long-wavelength harmonics can be used to fit curves to non-stationary short term data, our example clearly shows that it is inappropriate to extrapolate the best fit curves into the future.

Monitoring at the Mimbres Basin site is expected to continue through at least December 1992. This will allow the effects of annual cyclicity to be properly documented. Additional work will include the modification of previously developed mathematical models (e.g., Haneberg, 1992a) to account for draping of compressible elastic layers over rounded irregularities and asymmetric steps, analysis of fissure locations within the context of regional basin subsidence (Haneberg, 1992b), and further consideration of the earth tide issue.

Acknowledgments.– The research described in this paper was supported by the U.S. Geological Survey through New Mexico Water Resources Research Institute contracts 01423954 and 01345696. Matching funds were provided by the New Mexico Bureau of Mines and Mineral Resources. We also wish to thank June Cox for allowing continued access to her land over the years.

References Cited

Bredehoeft, J.D., 1967, Response of well-aquifer systems to earth tides: Journal of Geophysical Research, v. 72, p. 3075-3087.

Clemons, R.E., 1986, Petrography and stratigraphy of the Seville-Trident exploration wells near Deming, New Mexico: New Mexico Geology, v. 8, p. 5-11.

Clemons, R.E., and Mack, G.H., 1988, Geology of Southwestern New Mexico: New Mexico Geological Society, 39th Field Conference Guidebook, p. 45-57.

Contaldo, G.J., 1989,Earth fissures and land subsidence near Deming, New Mexico: unpublished M.S. thesis, New Mexico State University, Las Cruces, 106 p.

Contaldo, G.J. and Mueller, J.E., 1991a, Earth fissures and land subsidence of the Mimbres Basin, southwestern New Mexico, U.S.A., *in* Johnson, A.I., (ed.), Land Subsidence (Proceedings, Fourth International Symposium on Land Subsidence, Houston, Texas, May 12-17, 1991): International Association of Hydrological Sciences Publication No. 200, p. 301-310.

Contaldo, G.J., and Mueller, J.E., 1991b, Earth fissures of the Mimbres Basin, southwestern New Mexico: New Mexico Geology, v. 13, p. 69-74.

Darton, N.H., 1917, Description of the Deming quadrangle: U.S. Geological Survey, Geologic Atlas, Deming Folio, No. 207, 15 pp.

Gile, L.H., Hawley, J.W., and Grossman, R.B., 1981, Soils and geomorphology in the Basin and Range area of Southern New Mexico - Guidebook to the Desert Project: New Mexico Bureau of Mines and Mineral Resources, Memoir 39, 222 p.

Haneberg, W.C., 1992a, Drape folding of compressible elastic layers– I. Analytical solutions for vertical uplift: Journal of Structural Geology, in press.

Haneberg, W.C., 1992b, Thin-plate analysis of land subsidence and fissuring in the Mimbres Basin, southern New Mexico (abstract): Geological Society of America, Abstracts with Programs, v. 24, no. 5, p. A30.

Haneberg, W.C., Reynolds, C.B., and Reynolds, I.B., 1991, Geophysical characterization of soil deformation associated with earth fissures near San Marcial and Deming, New Mexico, *in* Johnson, A.I., (ed.), Land Subsidence (Procedings, Fourth International Symposium on Land Subsidence, Houston, Texas, May 12-17, 1991): International Association of Hydrological Sciences Publication No. 200, p. 271-280.

Holzer, T.L., 1984, Ground failure induced by groundwater withdrawal from unconsolidated sediments, *in* Holzer, T.L., (ed.), Man-Induced Land Subsidence: Geological Society of America, Reviews in Engineering Geology VI, p. 67-105.

Jaeger, J.C. and Cook, N.G.W., 1969, Fundamentals of Rock Mechanics: Chapman and Hall, 515 pp.

Press, W.H., Flannery, B.P., Tuekolsky, S.A., and Vetterling, W.T., 1988, Numerical Recipes in C: Cambridge, University Press, 735 pp.

Rojstaczer, S. and Agnew, D.C., 1989, The influence of formation material properties on the response of water levels in wells to earth tides and atmospheric loading: Journal of Geophysical Research, v. 94, p. 12,403-12,411.

Rojstaczer, S. and Riley, F.S., 1990, Response of the water level in a well to earth tides and atmospheric

loading under unconfined conditions: Water Resources Research, v. 26, p. 1803-1817.

van der Kamp, G. and Gale, J.E., 1983, Theory of earth tide and barometric effects in porous formations with compressible grains: Water Resources Research, v. 19, p. 538-544.

Wolfram, S., 1991, Mathematica– A System for Doing Mathematics by Computer (2d edn.): Redwood City, California, Addison-Wesley, 961 pp.

APPENDIX B

Haneberg, W.C. 1993. Drape folding of compressible elastic layers— II. Matrix solution for two-layer folds. *J. Struct. Geol.* In press.

Journal of Structural Geology, Vol. xx, No. xx, pp. xxx to xxx, 1993 (Ms. 169)
Printed in Great Britain

0191-8141/93 $05.00+0.00

Drape folding of compressible elastic layers—II. Matrix solution for two-layer folds

WILLIAM C. HANEBERG

New Mexico Bureau of Mines and Mineral Resources, New Mexico Institute of Mining and Technology, Socorro, NM 87801, U.S.A.

(*Received* 10 *February* 1992; *accepted in revised form* 7 *September* 1992)

Abstract—A matrix solution for two-layer drape folds in compressible elastic media is used to examine the relative importance of layer compressibility, layer stiffness, and the presence or absence of lower boundary shear on fold form, principal stress direction, and maximum shear stress distribution. The most obvious effect of decreasing the shear modulus of the lower layer is a change in principal stress orientation, accompanied by a decrease in maximum shear stress. Principal stress orientation, and to a lesser degree fold shape, can be further altered by changing the compressibility of an easily sheared basal layer. Characteristics of drape folds with welded and non-welded basal contacts, as observed in the field and predicted by a single layer model of drape folding, are also further explored with the two layer model.

INTRODUCTION

A PREVIOUS paper (Haneberg 1992), hereafter referred to as Part I, presented analytical solutions for two types of compressible elastic drape folding, which corresponded to the welded and non-welded end-members of Stearns (1978). The geologic significance of these two lower boundary conditions was discussed at some length, and will not be repeated here. An important conclusion of Part I was that details of drape fold geometry at depth, as well as the orientation of minor structures throughout the draped layer, should be controlled by the presence or absence of shear along the lower boundary. Compressibility also affected fold form to a small, but perceptible, degree. The Part I models, however, were limited to single-layer drape folds with an infinitesimally thin lower boundary. This paper extends the Part I analysis by developing a matrix solution for two-layer drape folds in compressible elastic media, so that the effects of lower boundary shear can be examined using a basal layer of finite thickness. In particular, it will be shown that the effects of variable shear across a basal layer of finite thickness are less obvious than in the single-layer folds of Part I, although the same basic patterns persist from one model to the other.

There has not been much previous work on the mechanics of multilayered drape folds. Reches & Johnson (1978) explained how to formulate the compressible elastic problem analyzed in this paper, and in general how to formulate matrix solutions to folding problems, but gave examples only for incompressible multilayers. Koch *et al.* (1981) investigated the effects of contact strength on monoclinal flexure of sedimentary sequences above laccolithic intrusions, which is a problem mechanically indistinguishable from draping over a buried fault. Their analysis was limited to stacks of simple elastic plates. Withjack *et al.* (1990) conducted a series of laboratory experiments, which subjected single and multiple clay layers to both extension and vertical displacement. However, they do not appear to have systematically evaluated the effects of an easily-sheared basal layer or contact.

TWO-LAYER MECHANICAL MODEL

General solution

The solution of plane-strain, multilayered folding problems in which axial shortening is the primary mechanism of folding has been discussed by a number of previous authors (e.g. Reches & Johnson 1978, Johnson & Pfaff 1989, Cruikshank & Johnson in press). Each fold is assumed to be part of an infinitely long, periodic train of folds and biharmonic solutions of the type developed in Part I are written for each layer. Then, boundary conditions are matched across each interface between layers to insure that both stresses and displacements are consistent in adjoining layers. For drape folds formed solely by vertical uplift, however, it is not necessary to include axial shortening terms, which simplifies the analysis considerably (Reches & Johnson 1978). Variables used in this analysis (Fig. 1) are the same as those

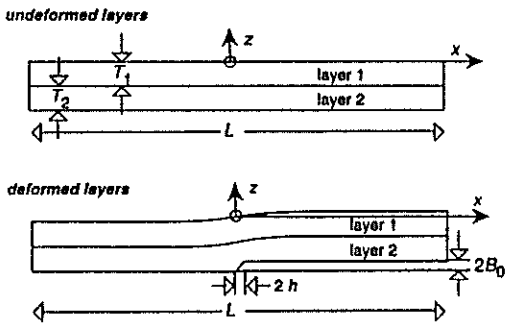

Fig. 1. Illustration of geometric parameters used in the two-layer drape fold model. With the exception of two separate layer thickness values, these parameters are identical to those in Part I.

in Part I, except that the total thickness of the fold is the sum of two individual layer thicknesses. $T_1 + T_2$. Vertical displacement along the lower boundary is specified using a Fourier sine series, which is analogous to throw of $2B_0$ across a buried vertical fault zone of width $2h$. Neither horizontal slip along the lower boundary nor layer-parallel extension are allowed in this model. The symbolic manipulation capabilities of the computer program *Mathematica* (Wolfram 1988) were used extensively during derivation of the two-layer solution.

By analogy with Part I, the horizontal (u) and vertical (v) components of displacement within layer 1, normalized relative to the fold wavelength, L, are

$$\frac{u_1}{L} = \left[\left(\frac{c_{11}}{L} + c_{12}\frac{z}{L}\right)e^{lz} + \left(\frac{c_{13}}{L} + c_{14}\frac{z}{L}\right)e^{-lz}\right]\cos lx \quad (1)$$

$$\frac{v_1}{L} = \left\{\left[\frac{(3c_{12} - c_{11}l) + \frac{\lambda_1}{G_1}(c_{12} - c_{11}l)}{n\pi\left(1 + \frac{\lambda_1}{G_1}\right)} - c_{12}\frac{z}{L}\right]e^{lz} + \left[\frac{(3c_{14} + c_{13}l) + \frac{\lambda_1}{G_1}(c_{14} + c_{13}l)}{n\pi\left(1 + \frac{\lambda_1}{G_1}\right)} + c_{14}\frac{z}{L}\right]e^{-lz}\right\}\sin lx \quad (2)$$

and the analogous normalized components of displacement within layer 2 are

$$\frac{u_2}{L} = \left[\left(\frac{c_{21}}{L} + c_{22}\frac{z}{L}\right)e^{lz} + \left(\frac{c_{23}}{L} + c_{24}\frac{z}{L}\right)e^{-lz}\right]\cos lx \quad (3)$$

$$\frac{v_2}{L} = \left\{\left[\frac{(3c_{22} - c_{21}l) + \frac{\lambda_2}{G_2}(c_{22} - c_{21}l)}{n\pi\left(1 + \frac{\lambda_2}{G_2}\right)} - c_{12}\frac{z}{L}\right]e^{lz} + \left[\frac{(3c_{24} + c_{23}l) + \frac{\lambda_2}{G_2}(c_{24} + c_{23}l)}{n\pi\left(1 + \frac{\lambda_2}{G_2}\right)} + c_{24}\frac{z}{L}\right]e^{-lz}\right\}\sin lx. \quad (4)$$

Single subscripts represent the layer number, whereas double subscripts represent both the layer number (first subscript) and the number of the variable within that layer (second subscript). For example, c_{23} would be the third constant of integration for the second layer. The z-axis is positive upwards, and the wave number is

$$l = n\pi/L, \quad (5)$$

where n is any integer and L is the wavelength of the fold.

The layer 1 and displacement components have been multiplied throughout by $G_1/G_1 = 1$ and the layer 2 displacement components by $G_2/G_2 = 1$, which allows the four material constants of the two-layer system to be expressed in terms of three dimensionless numbers: G_2/G_1, λ_1/G_1 and λ_2/G_2. The second layer is the lowermost of the two, so values of $G_2/G_1 < 1$ mean that the lower layer is more easily sheared than is the upper layer. In terms of Young's modulus (E) and Poisson's ratio (ν), the shear modulus ratio is

$$\frac{G_2}{G_1} = \frac{E_2}{E_1}\left(\frac{1 + \nu_1}{1 + \nu_2}\right). \quad (6)$$

As in Part I, λ_1/G_1 reflects the compressibility of layer 1, or

$$\frac{\lambda_1}{G_1} = \frac{2\nu_1}{1 - 2\nu_1} \quad (7)$$

and the third material constant reflects the compressibility of layer 2, or

$$\frac{\lambda_2}{G_2} = \frac{2\nu_2}{1 - 2\nu_2}. \quad (8)$$

As before, the single subscripts denote the layer number. In practice, layer compressibilities can be specified in terms of Poisson's ratio, from which λ_1/G_1 and λ_2/G_2 can be easily calculated.

Multiplying equations (1)–(4) by L and differentiating once each with respect to x or z, as appropriate, yields the dimensionless displacement gradients

$$\frac{\partial u_1}{\partial x} = -l[(c_{11} + c_{12}z)e^{lz} + (c_{13} + c_{14}z)^{-lz}]\sin lx \quad (9)$$

$$\frac{\partial u_1}{\partial z} = \{[lc_{11} + (1 + lz)c_{12}]e^{lz} - [lc_{13} - (1 - lz)c_{14}]e^{-lz}\}\cos lx \quad (10)$$

$$\frac{\partial v_1}{\partial x} = \left\{\left[\frac{3c_{12} - c_{11}l + \frac{\lambda_1}{G_1}(c_{12} - c_{11}l)}{1 + \frac{\lambda_1}{G_1}} - c_{12}lz\right]e^{lz} + \left[\frac{3c_{14} + c_{13}l + \frac{\lambda_1}{G_1}(c_{14} + c_{13}l)}{1 + \frac{\lambda_1}{G_1}} + c_{14}lz\right]e^{-lz}\right\}\cos lx \quad (11)$$

$$\frac{\partial v_1}{\partial z} = \left\{\left[\frac{3c_{12} - c_{11}l + \frac{\lambda_1}{G_1}(c_{12} - c^{11}l)}{1 + \frac{\lambda_1}{G_1}} - (lz + 1)c_{12}\right]e^{lz}\right.$$

$$-\left[\frac{3c_{14} + c_{13}l + \frac{\lambda_1}{G_1}(c_{14} + c_{13}l)}{1 + \frac{\lambda_1}{G_1}}\right.$$

$$\left.\left. + (lz - 1)c_{14}\right]e^{-lz}\right\}\sin lz \quad (12)$$

$$\frac{\partial u_2}{\partial x} = -l[(c_{21} + c_{22}z)e^{lz} + (c_{23} + c_{24}z)e^{-lz}]\sin lx \quad (13)$$

$$\frac{\partial v_2}{\partial x} = \left\{\left[\frac{(3c_{22} - c_{21}l) + \frac{\lambda_2}{G_2}(c_{22} - c_{21}l)}{1 + \frac{\lambda_1}{G_2}} - c_{22}lz\right]e^{lz}\right.$$

$$+\left[\frac{(3c_{24} + c_{23}l) + \frac{\lambda_2}{G_2}(c_{24} + c_{23}l)}{1 + \frac{\lambda_2}{G_2}}\right.$$

$$\left.\left. + c_{24}lz\right]e^{-lz}\right\}\cos lx \quad (14)$$

$$\frac{\partial u_2}{\partial z} = \{[c_{21}l + c_{22}(1 + lz)]e^{lz}$$

$$-[c_{23}l - c_{24} - (1 - lz)]e^{-lz}\}\cos lx \quad (15)$$

$$\frac{\partial v_2}{\partial z} = \left\{\left[\frac{(3c_{22} - c_{21}l) + \frac{\lambda_2}{G_2}(c_{22} - c_{21}l)}{1 + \frac{\lambda_2}{G_2}}\right.\right.$$

$$\left.\left. - (1 + lz)c_{22}\right]e^{lz}\right.$$

$$-\left[\frac{l(3c_{24} + c_{23}l) + \frac{\lambda_2}{G_2}(c_{24} + c_{23}l)}{1 + \frac{\lambda_2}{G_2}}\right.$$

$$\left.\left. + (1 - lz)c_{24}\right]e^{-lz}\right\}\sin lx. \quad (16)$$

These gradients are identical in form to those in Part I.

Once the eight displacement gradients have been evaluated, normalized stresses in each of the layers can be calculated using

$$\frac{\sigma_{xx,1}}{G_1} = \left(\frac{\lambda_1}{G_1} + 2\right)\frac{\partial u_1}{\partial x} + \frac{\lambda_1}{G_1}\frac{\partial v_1}{\partial z} \quad (17)$$

$$\frac{\sigma_{zz,1}}{G_1} = \left(\frac{\lambda_1}{G_1} + 2\right)\frac{\partial v_1}{\partial z} + \frac{\lambda_1}{G_1}\frac{\partial u_1}{\partial x} \quad (18)$$

$$\frac{\sigma_{xz,1}}{G_1} = 2\left(\frac{\partial u_1}{\partial z} + \frac{\partial v_1}{\partial x}\right) \quad (19)$$

$$\frac{\sigma_{xx,2}}{G_1} = \frac{G_2}{G_1}\left[\left(\frac{\lambda_2}{G_2} + 2\right)\frac{\partial u_2}{\partial x} + \frac{\lambda_2}{G_2}\frac{\partial v_2}{\partial z}\right] \quad (20)$$

$$\frac{\sigma_{zz,2}}{G_1} = \frac{G_2}{G_1}\left[\left(\frac{\lambda_2}{G_2} + 2\right)\frac{\partial v_2}{\partial z} + \frac{\lambda_2}{G_2}\frac{\partial u_2}{\partial x}\right] \quad (21)$$

$$\frac{\sigma_{xz,1}}{G_1} = 2\frac{G_2}{G_1}\left(\frac{\partial u_2}{\partial z} + \frac{\partial v_2}{\partial x}\right). \quad (22)$$

Tensile normal stresses are considered positive. Lithostatic normal stresses (Hafner 1951) are ignored in this analysis in order to focus attention on the perturbed stress and displacement fields that arise during folding. If desired, however, lithostatic terms can be included by simply adding them to equations (17), (18), (20) and (21).

Particular solution

In Part I, the particular solutions were found by algebraically solving four linear equations in order to determine the four constants of integration. In the two-layer model, however, there are twice as many constants of integration. Although it is possible to solve algebraically a system of eight linear equations, it is extremely impractical for folding problems. An algebraic solution to the two-layer problem was obtained using *Mathematica* (Wolfram 1988). However, the resulting expressions were several hundreds of lines long and computer limitations slowed the algebraic simplification algorithm to a crawl. In order to circumvent this difficulty, previous workers (e.g. Reches & Johnson 1978) used matrix methods to solve the equations simultaneously. This paper uses an analogous method for two compressible elastic layers, which can be expanded to model an arbitrary number of layers.

Because both layers are originally flat, the vertical normal (σ_{zz}) and horizontal shear (σ_{xz}) stresses can be used as a first-order approximation of the normal and shear stresses acting along each layer boundary. As the slopes of interfaces between drape-folded layers increase beyond about 15°, however, this approximation becomes increasingly erroneous. Similar problems are encountered in compressional or extensional folding problems, in which the interfaces separating mechanically distinct layers must have some original perturbation in order for dynamic instabilities to grow. Accuracy of the boundary stress approximations can be

increased either through higher-order algebraic approximations for slopes up to about 30° (Johnson & Pfaff 1989) or least-squares interface matching methods for high-amplitude folds (Fletcher 1974, Cruikshank & Johnson in press).

The upper boundary of the drape fold is assumed to be traction free, subjected to neither shear nor normal forces. This corresponds to the Earth's surface. Mathematically, the first two boundary conditions are:

$$\sigma_{xz,1} = 0 \tag{23}$$

$$\sigma_{zz,1} = 0 \tag{24}$$

evaluated at $z = 0$. In order that the contact between the two elastic layers does not separate during folding, layer-parallel and layer-perpendicular displacements and stresses must be equal in both layers. This gives the four internal boundary conditions

$$\sigma_{xz,1} = \sigma_{xz,2} \tag{25}$$

$$\sigma_{zz,1} = \sigma_{zz,2} \tag{26}$$

$$u_1 = u_2 \tag{27}$$

$$v_1 = v_2 \tag{28}$$

evaluated along the undeformed contact, which is given by the Lagrangian co-ordinate $z = -T_1$.

Boundary condition (25) implies that the contact between the two compressible layers is strongly bonded, so that no slip can occur along the interface between the two layers. Instead, layer-parallel displacement with the lower portion of the two-layer fold can be simulated by reducing the shear modulus of layer 2. This combination of a no-slip boundary condition and an easily sheared lower layer distributes shear throughout layer 2, which has finite thickness, rather than along an infinitesimally thin contact as in Part I. In this manner, conclusions about the importance of basal shear on fold form and minor structures can be more fully examined. If free slip between the two layers were desired, however, equation (25) could be re-written as $\sigma_{xz,1} = 0$ and $\sigma_{xz,2} = 0$. Finally, the base of layer 2 is subjected to the same displacement conditions as in Case 1 of Part I

$$u_2 = 0 \tag{29}$$

$$\frac{v_2}{L} = b_n \sin lx \tag{30}$$

evaluated at $z = -(T_1 + T_2)$. Thus, there is no slip allowed along the base of layer 2. The Fourier coefficients in (30) are given by

$$b_n = \frac{2B_0/L}{n\pi - 4n^3\pi(h/L)^2}\left[\cos\left(n\pi\frac{h}{L}\right) - \left(\left[1 - 4n^2\left(\frac{h}{L}\right)^2 \times \left[1 - \cos\left(\frac{\pi}{2}\frac{L}{h}\right)\right]\right]\cos\left(n\pi\frac{h}{L}\right) - \left[4n^2\left(\frac{h}{L}\right)^2 - 2n\left(\frac{h}{L}\right)\sin\left(n\pi\frac{h}{L}\right)\right]\sin\left(\frac{\pi}{2}\frac{L}{h}\right)\right)(-1)^n\right] \tag{31}$$

which is identical to that used in Part I. As before, any Fourier sine series could have been used to specify vertical displacement along the base of layer 2.

Each of the boundary conditions is evaluated by substituting the appropriate stress or displacement equation(s) into equations (23)–(30), and setting z equal to 0, $-T_1$, or $-(T_1 + T_2)$ as appropriate. This will give rise to eight linear equations that can be rearranged and put into the matrix form

$$\mathbf{Mc} = \mathbf{f}$$

or, expanding the boundary condition equations,

$$\begin{bmatrix} 0 & m_{12} & 0 & m_{14} & 0 & 0 & 0 & 0 \\ m_{21} & m_{22} & m_{23} & m_{24} & 0 & 0 & 0 & 0 \\ 0 & m_{32} & 0 & m_{34} & 0 & m_{36} & 0 & m_{38} \\ m_{41} & m_{42} & m_{43} & m_{44} & m_{45} & m_{46} & m_{47} & m_{48} \\ m_{51} & m_{52} & m_{53} & m_{54} & m_{55} & m_{56} & m_{57} & m_{58} \\ m_{61} & m_{62} & m_{63} & m_{64} & m_{65} & m_{66} & m_{67} & m_{68} \\ 0 & 0 & 0 & 0 & m_{75} & m_{76} & m_{77} & m_{78} \\ 0 & 0 & 0 & 0 & m_{85} & m_{86} & m_{87} & m_{88} \end{bmatrix} \begin{Bmatrix} c_{11} \\ c_{12} \\ c_{13} \\ c_{14} \\ c_{21} \\ c_{22} \\ c_{23} \\ c_{24} \end{Bmatrix} = \begin{Bmatrix} 0 \\ 0 \\ 0 \\ 0 \\ 0 \\ 0 \\ 0 \\ b_n \end{Bmatrix}. \tag{32}$$

This system of eight equations must be solved repeatedly for many values of n (in this paper $n = 1 \ldots 100$), and the results added together to arrive at an adequate approximation of the desired boundary displacement. The 42 non-zero elements of M are listed in the Appendix.

Drawing an analogy from the vocabulary of structural engineering, M is the stiffness matrix, which takes into account the material properties and thicknesses of the layers. Likewise, f is the driving vector, which characterizes the width of and throw across a buried vertical fault. In this problem, vertical uplift along the base of layer 2 is the sole component of the driving vector.

The coefficient vector c can be calculated using one of the linear equation solvers available in most mathematical subroutine packages. There are, however, two caveats. First, the method of solution must employ some form of pivoting because, as the problem is formulated in this paper, the diagonal elements m_{11} and m_{33} are zero. Second, the stiffness matrix M tends to be highly ill-conditioned. This means that small changes in the driving vector f will produce large changes in the coefficient vector c. In order to circumvent potential conditioning problems, the examples presented in this paper were solved using L–U decomposition and back-substitution with iterative improvement (Press *et al.* 1988).

RESULTS

The effects of contrasting layer stiffness and layer compressibility can be illustrated using the series of four examples summarized in Table 1. The objective of these numerical experiments is to investigate the transition from a welded to a non-welded contact (Stearns 1978) by varying the stiffness and compressibility along the base of a theoretical drape fold. In Part I, Case 1 corresponded to a welded contact along which no layer-

Table 1. Geometry and material constants for Examples 1–4

Example	T_1/L	T_2/L	B_0/L	h/L	G_2/G_1	ν_1	ν_2
1	0.05	0.05	0.01	0.01	1.00	0.10	0.10
2	0.05	0.05	0.01	0.01	0.10	0.10	0.10
3	0.05	0.05	0.01	0.01	0.10	0.10	0.25
4	0.05	0.05	0.01	0.01	0.10	0.10	0.49

parallel slip was allowed and Case 2 corresponded to a non-welded contact with no shear strength. Example 1, in which neither stiffness or rigidity vary between the two layers, is identical to a Case 1 fold of thickness $T/L = 0.10$ in Part I. In the other three examples, the stiffness and compressibility contrast between the two layers is varied. Layer thickness, fault zone width and vertical displacement along the lower boundary are held constant in all four examples. The model results are presented in four ways: fold form; displacement field; principal stress trajectory field; and maximum shear stress field. The first three categories are familiar to geologists; however, because tensile stresses are defined as positive, the greatest principal stress (σ_1) is the most tensile or least compressive principal stress. Likewise, σ_3 is the most compressive or least tensile principal stress.

For the examples given below, maximum shear stress (e.g. Pollard & Segall 1987) values were calculated on a grid of 21 rows × 201 columns, and the values from four grid points were used to calculated an average value for each of 4000 quadrilaterals. Average values mask both the highest and lowest point values associated with each quadrilateral; however, the maximum and minimum calculated values are given along the scale bar beneath each shear stress plot. The displacement solutions derived above were used to transform each originally square element into its deformed shape, allowing the average maximum shear stress within each deformed quadrilateral to be plotted as part of a gray-scale diagram.

When there is no stiffness or compressibility contrast between layers, the two-layer solution (Fig. 2) produces results identical to the Case 1 single layer solution (Part I).

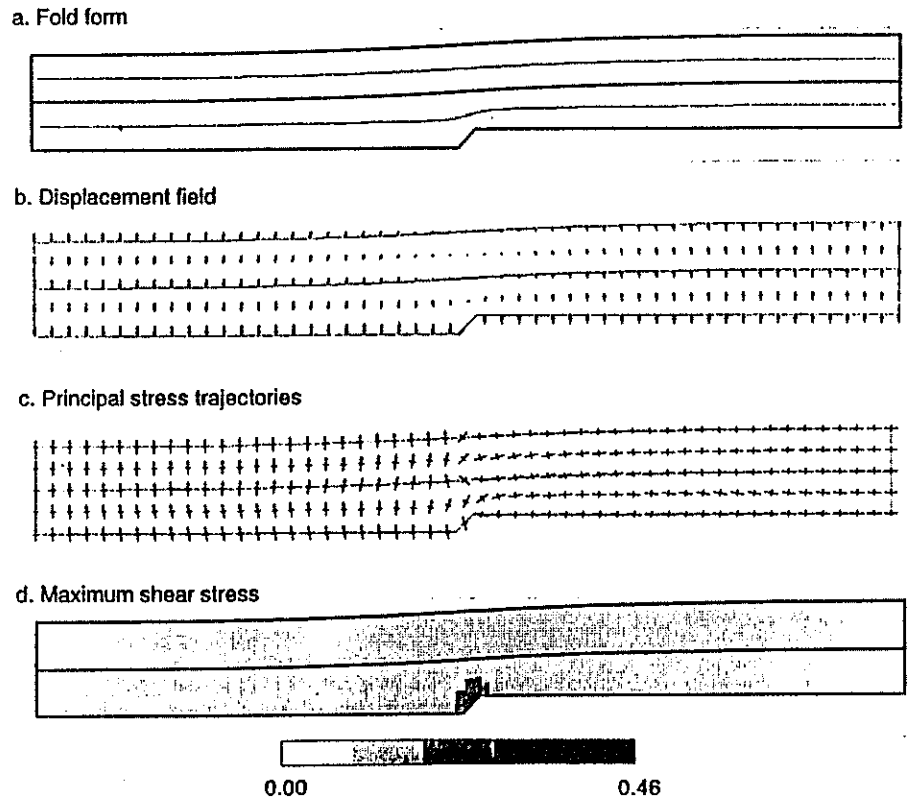

Fig. 2. Results of Example 1, which is identical to a Case 1 (welded base) fold of thickness $T/L = 0.1$ in Part I. (a) Fold form, with black lines used to denote the two layers, and gray lines used to denote passive markers within each of the layers. The passive markers are kinematic indicators that deform with the layer, but have no mechanical effect. (b) Displacement field, showing resultant vectors ($\sqrt{u^2 + v^2}$). Outlines of the two layers are shown in the background. (c) Principal stress trajectory field. Long axes represent the most tensile principal stress (σ_1), whereas short axes represent the most compressive principal stress (σ_3). Outlines of the two layers are shown in the background. (d) Averaged maximum shear stress intensity, with minimum and maximum values indicated on the scale bar. No horizontal or vertical exaggeration in any of the figures.

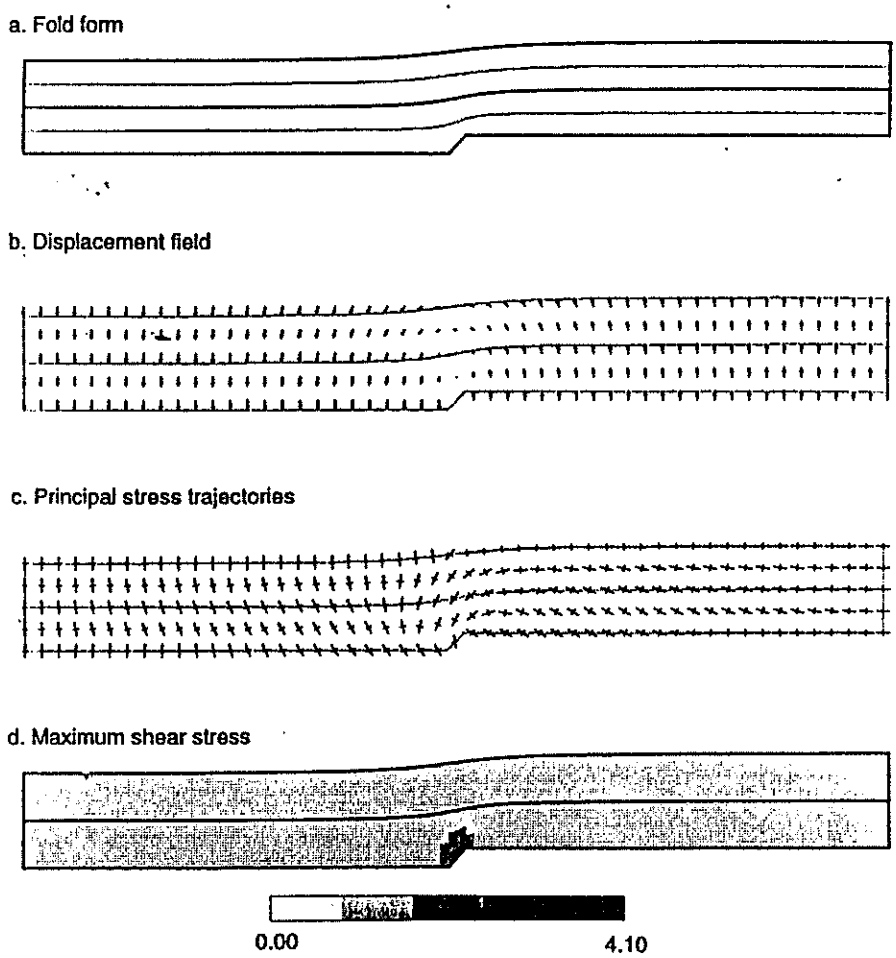

Fig. 3. Results of Example 2, illustrating the effects of an easily-sheared lower layer with no compressibility contrast. Explanations for parts (a)–(d) are the same as in Fig. 2, and material constants shown in Table 1.

When the stiffness of the lower layer is reduced by an order of magnitude, however, subtle changes begin to occur (Fig. 3). There is essentially no difference in the forms of Example 1 and Example 2 folds; however, the resultant displacement vectors in layer 2 of Fig. 3 are directed slightly inward. For comparison with the two end-members developed in Part I, this is the beginning of a transformation from the distinctly concave-downward, ∩-shaped displacement field characteristic of Case I folds to the concave-upward, U-shaped displacement characteristic of Case II folds. Stress trajectories are more nearly parallel to the interface between layers 1 and 2 than in Example 1 (Fig. 2) stress trajectories, because shear stresses along the interface are approaching zero. The maximum shear stress also drops nearly an order of magnitude, from $4.10G_1$ to $0.46G_1$, between Example 1 and Example 2. In both cases, however, elevated shear stresses are concentrated directly above the fault scarp.

Example 3 (Fig. 4) is an intermediate case included to illustrate the relative insensitivity of the model to small changes in layer compressibility. The stiffness contrast between the two layers remains at $G_2/G_1 = 0.1$, but the Poisson's ratio of layer 2 is increased from $\nu_2 = 0.10$ to $\nu_2 = 0.25$. There are two effects. First, there is a barely perceptible tilting of principal stress axes within and along the boundaries of layer 2. This tilting is best observed by overlaying enlargements of Figs. 3(c) and 4(c) on a light table or computer screen. Again recalling the definition of principal stress planes, the small degree of rotation from horizontal and vertical means that layer-parallel shear stress is increasing within layer 2, and is also being transferred to layer 1. The second effect is a small increase in maximum shear stress from $0.46G_1$ in Example 2 to $0.58G_1$ in Example 3.

Much more noticeable changes occur if the lower layer is given a Poisson's ratio of $\nu_2 = 0.49$, making it essentially incompressible (Fig. 5). First, the drape fold becomes tighter, particularly through the upper layer. Second, the U-shaped displacement vector field becomes even more strongly developed. Third, principal stress axes along the boundaries of layer 2 are rotated

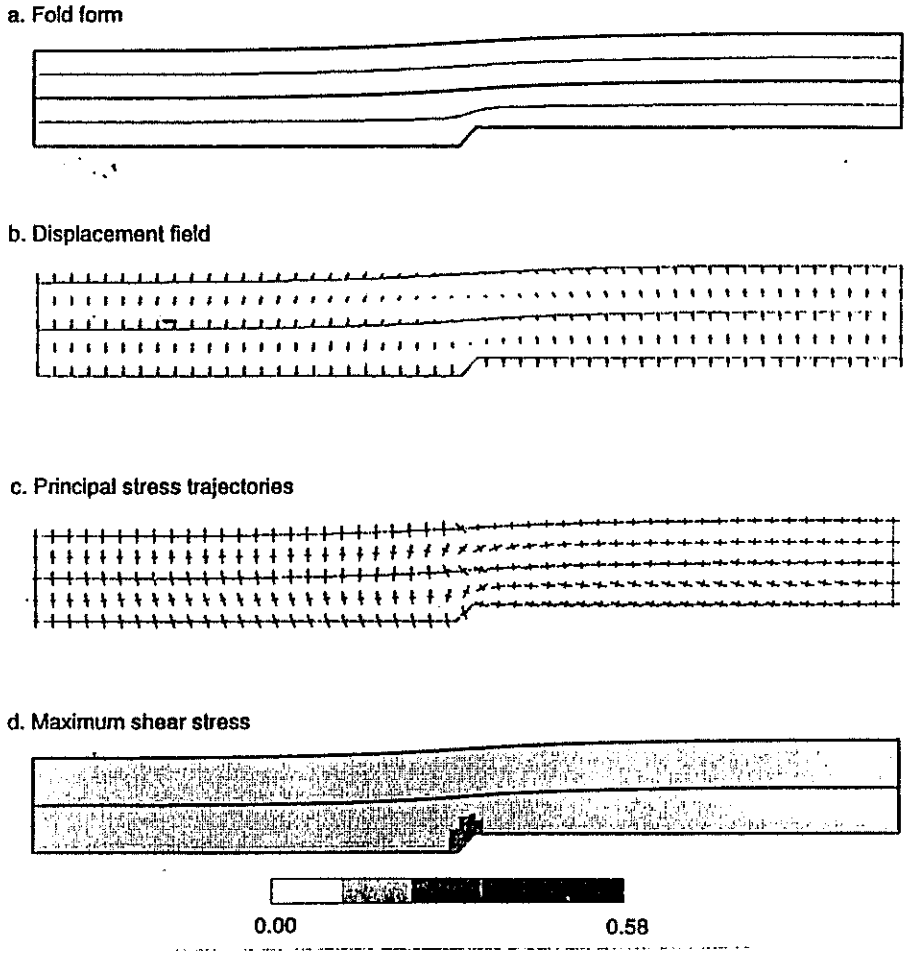

Fig. 4. Results of Example 3, illustrating the effects of an easily-sheared lower layer with a moderate compressibility contrast. Explanations for parts (a)–(d) are the same as in Fig. 2, and material constants shown in Table 1.

approximately 45° from horizontal and vertical. Principal stress orientation within layer 2 is also highly variable. Notice that, on the left-hand side of Fig. 5(c), the state of stress within layer 2 changes from layer-parallel deviatoric compression near the underlying fault to layer-parallel deviatoric tension away from the underlying fault. The reverse is true on the right-hand side of Fig. 5(c). Fourth, the maximum shear stress increases slightly, from $0.58G_1$ in Example 3 to $0.72G_1$ in Example 4, and a small zone of elevated shear stress begins to develop near the base of layer 1.

One of the major conclusions of Part I was that non-welded (Case II) lower boundaries should become asymmetric during draping, and that the inflection point of the lower boundary should shift slightly towards the upthrown side of the fault. The gradual development of concave-upward, or U-shaped displacement fields in Examples 2–4 shows that the same asymmetry develops, albeit much more weakly, in two-layer drape folds with easily sheared lower layers. The asymmetry is emphasized by a plot showing the curvature, or second derivative, of the height of the deformed interface ($z + v$) with respect to the final horizontal co-ordinates ($x + u$), of the passive marker within layer 2 (Fig. 6). Large absolute values indicate tight folds, whereas small absolute values indicate open folds; positive values reflect concave-upward curvature, whereas negative values indicate concave-downward curvature. In Example 1, both the positive and negative peaks have approximately the same width and amplitude. This means that the deformed passive marker developed sinusoidal symmetry during deformation. In Example 4, however, the concave-upward portion of the drape fold is wider and more open than the concave-downward portion, just as in Case II of Part I. In addition, the entire Example 4 curve is shifted slightly to the right.

DISCUSSION

A series of numerical experiments shows that the distinctive end-member characteristics of drape folds

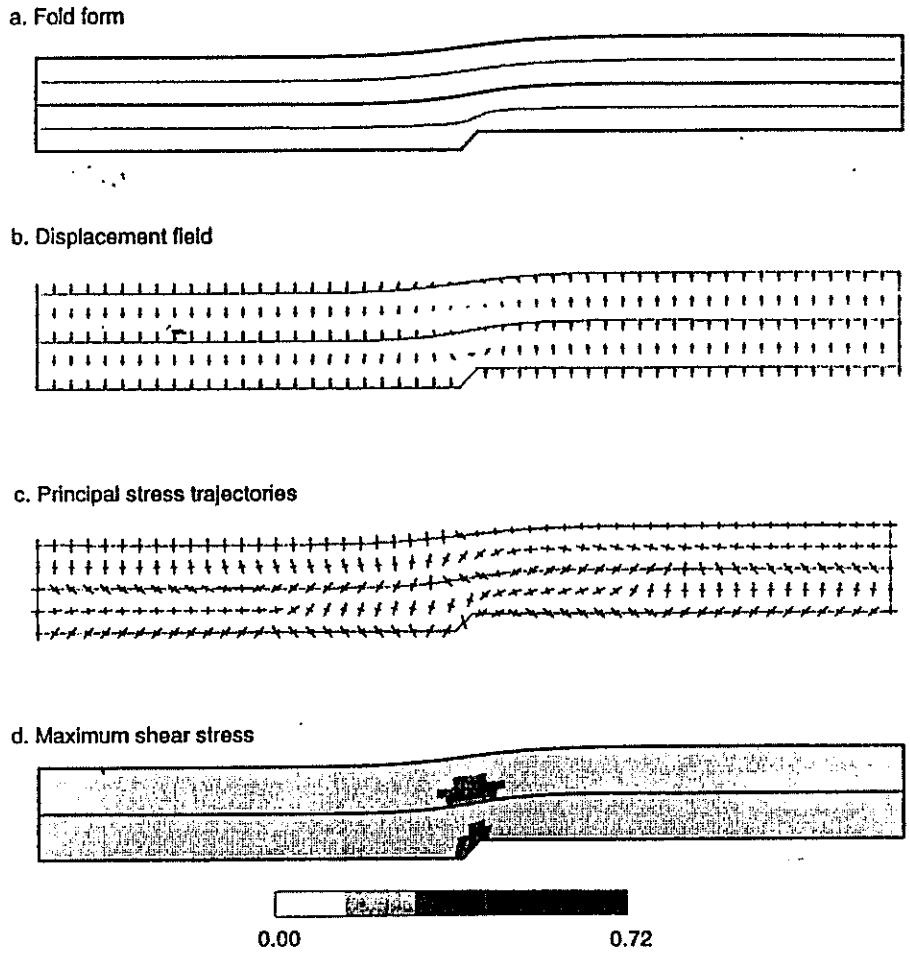

Fig. 5. Results of Example 4, illustrating the effects of an easily-sheared lower layer with a strong compressibility contrast. Explanations for parts (a)–(d) are the same as in Fig. 2, and material constants shown in Table 1.

with welded and non-welded bases, described previously in Part I, can be qualitatively reproduced using a two-layer mechanical model with an easily sheared, nearly incompressible base. These characteristics, however, are not as strongly developed as in Part I. This may be because the basal contact in Case II of Part I was infinitesimally thin, perfectly frictionless and perfectly incompressible. The present analysis, in contrast, treats a basal layer of finite thickness with a finite shear modulus and some compressibility. The effects of large vertical displacement and layer parallel extension, which have been investigated in the laboratory by others (e.g. Withjack *et al.* 1990), remain uncertain.

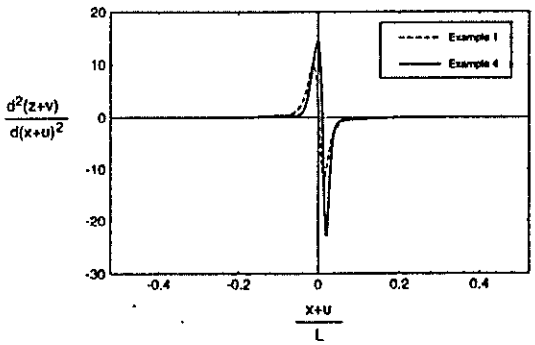

Fig. 6. Curvature of passive markers from Examples 1 and 4. Both markers were originally straight lines at a depth of $z/L = -0.075$. The asymmetry of the drape-folded markers is indicated by the markedly asymetric curvature of the Example 4 marker.

Whereas the effects of a weak basal layer could have been predicted to some degree from the results of Part I, the effects of a compressibility contrast were not evident in the single layer solution. At the very least, this analysis shows that compressibility contrasts can produce noticeable changes in stress orientation and magnitude, as well as small changes in fold form (cf. Reches & Johnson 1978). Geologically, then, it might be important to distinguish between slow and rapid deformation of a saturated clay or shale. If deformation were slow, excess pore pressures might be quickly dissipated and the hypothetical saturated layer would become effectively very compressible. If the deformation were rapid,

on the other hand, then the saturated layer would become very nearly incompressible. In the parlance of soil mechanics and modern poroelastic theory (e.g Rice & Cleary 1976), these two modes of deformation correspond to drained and undrained loading.

The four examples given here suggest that one might, in principle, be able to infer both stiffness and compressibility contrasts by careful mapping of minor structures or strain distributions in real folds. To wit, the only difference between Examples 2, 3 and 4 is the compressibility of the lower layer. Although there is little perceptible difference between the idealized elastic layers in Examples 2 and 3, there is a noticeable difference between either of these two and Example 4. Whether or not the differences will be significant enough to be discernable in rocks is another matter, although it has been shown that careful analysis of mechanical stratigraphy can be used to successfully model the general forms of real folds (Johnson & Pfaff 1989, Cruikshank & Johnson in press). The complicated inter-relationships among geometry, stiffness and compressibility, however, suggest that oversimplified attempts to infer details of subsurface structure from the surface expression of a fold may be prone to failure. Each additional layer confounds the problem of subsurface prediction, which was first raised with regard to single-layer drape folds in Part I.

Acknowledgements—This work was supported primarily by the New Mexico Bureau of Mines and Mineral Resources, with additional funding from the United States Geological Survey through the New Mexico Water Resources Research Institute (grant 01423954). Discussions with K. M. Cruikshank help to clarify some mechanical issues, and comments by A. M. Johnson and an anonymous reviewer improved the manuscript. An unpublished manuscript by A. M. Johnson and R. C. Flecther, "Theories of Folding and Density Instability", was also invaluable during this work.

REFERENCES

Cruikshank, K. M. & Johnson, A. M. In press. High-amplitude folding of linear-viscous multilayers. *J. Struct. Geol.*

Fletcher, R. C. 1974. Wavelength selection in the folding of a single layer with power-law rheology. *Am. J. Sci.* 274, 1029–1043.

Hafner, W. 1951. Stress distributions and faulting. *Bull. geol. Soc. Am.* 62, 373–398.

Haneberg, W. C. 1992. Drape folding of compressible elastic layers—I. Analytical solutions for vertical uplift. *J. Struct. Geol.* 14, 713–721.

Johnson, A. M. & Pfaff, V. J. 1989. Parallel, similar and constrained folds. In: Richard H. Jahns Memorial Volume (edited by Johnson A. M., Burnham, C. W., Allen, C. R., & Muehlberger, W. *Engng. Geol.* 27, 115–180.

Koch, F. G., Johnson, A. M. & Pollard, D., D. 1981. Monoclinal bending of strata over laccolithic intrusions. *Tectonophysics* 74, T21–T31.

Pollard, D. D. & Segall, P. 1987. Theoretical displacements and stresses near fractures in rock: with applications to faults, joints, veins, dikes, and solution surfaces. In: *Fracture Mechanics of Rock* (edited by Atkinson, B. K.). Academic Press, London, 277–349.

Press, W. H., Flannery, B. P., Teukolsky, S. A. & Vetterling, W. T. 1988. *Numerial Recipes in C.* Cambridge University Press, Cambridge.

Reches, Z. & Johnson, A. M. 1978. Development of monoclines: Part II. Theoretical analysis of monoclines. In: *Laramide Folding Associated with Basement Block Faulting in the Western United States* (edited by Matthews, V. III). *Mem. geol. Soc. Am.* 151, 273–312.

Rice, J. R. & Cleary, M. P. 1976. Some basic stress solutions for fluid-saturated porous media with compressible constitutents. *Rev. Geophys. & Space Phys.* 14, 227–241.

Stearns, D. W. 1978. Faulting and forced folding in the Rocky Mountains foreland. In: *Laramide Folding Associated with Basement Block Faulting in the Western United States* (edited by Matthews, V. III). *Mem. geol. Soc. Am.* 151, 1–37.

Withjack, M. O., Olson, J. & Peterson, E. 1990. Experimental models of extensional forced folds. *Bull. Am. Ass. Petrol. Geol.* 74, 1038–1054.

Wolfram, S. 1988. *Mathematica.* Addison-Wesley, Redwood City, California.

APPENDIX

Elements of the stiffness matrix M are found by evalutating the two upper, four internal, and two lower boundary conditions at $z/L = 0$, $z/L = -T_1$ and $z/L = -(T_1 + T_2)$, respectively. Terms in each of the eight boundary condition equations are then grouped in order to isolate the coefficients of $c_{11} \ldots c_{24}$. The 42 non-zero elements of M are:

$$m_{12} = 4\left(\frac{2 + \frac{\lambda_1}{G_1}}{1 + \frac{\lambda_1}{G_1}}\right) \tag{A1}$$

$$m_{14} = m_{12} \tag{A2}$$

$$m_{21} = 2l\left(1 + \frac{\lambda_1}{G_1}\right) \tag{A3}$$

$$m_{22} = \tfrac{1}{2}m_{12} \tag{A4}$$

$$m_{23} = m_{21} \tag{A5}$$

$$m_{24} = -m_{22} \tag{A6}$$

$$m_{32} = m_{12}e^{-lT_1} \tag{A7}$$

$$m_{34} = m_{12}e^{lT_1} \tag{A8}$$

$$m_{36} = 4\frac{G_2}{G_1}\left(\frac{2 + \frac{\lambda_2}{G_2}}{1 + \frac{\lambda_2}{G_2}}\right)e^{-lT_1} \tag{A9}$$

$$m_{38} = 4\frac{G_2}{G_1}\left(\frac{2 + \frac{\lambda_2}{G_2}}{1 + \frac{\lambda_2}{G_2}}\right)e^{lT_1} \tag{A10}$$

$$m_{41} = m_{21}e^{-lT_1} \tag{A11}$$

$$m_{42} = 2\left[\frac{2 + lT_1 + \frac{\lambda_1}{G_1} + 2lT_1\frac{\lambda_1}{G_1} + lT_1\left(\frac{\lambda_1}{G_1}\right)^2}{1 + \frac{\lambda_1}{G_1}}\right]e^{-lT_1} \tag{A12}$$

$$m_{43} = m_{21}e^{lT_1} \tag{A13}$$

$$m_{44} = 2\left[\frac{-2 + lT_1 - \frac{\lambda_1}{G_1} + 2lT_1\frac{\lambda_1}{G_1} + lT_1\left(\frac{\lambda_1}{G_1}\right)^2}{1 + \frac{\lambda_1}{G_1}}\right]e^{lT_1} \tag{A14}$$

$$m_{45} = 2l\frac{G_2}{G_1}\left(1 + \frac{\lambda_2}{G_2}\right)e^{-lT_1} \tag{A15}$$

$$m_{46} = -2\frac{G_2}{G_1}\left[\frac{2 + \frac{\lambda_2}{G_2} + lT_1 + 2lT_1\frac{\lambda_2}{G_2} + lT_1\left(\frac{\lambda_2}{G_2}\right)^2}{1 + \frac{\lambda_2}{G_2}}\right]e^{-lT_1} \tag{A16}$$

$$m_{47} = 2l\frac{G_2}{G_1}\left(1+\frac{\lambda_2}{G_2}\right)e^{lT_1} \tag{A17}$$

$$m_{48} = 2\frac{G_2}{G_1}\left[\frac{2+\frac{\lambda_2}{G_2}-lT_1-2lT_1\frac{\lambda_2}{G_2}-lT_1\left(\frac{\lambda_2}{G_2}\right)^2}{1+\frac{\lambda_2}{G_2}}\right]e^{lT_1} \tag{A18}$$

$$m_{51} = e^{-lT_1} \tag{A19}$$

$$m_{52} = -T_1 m_{51} \tag{A20}$$

$$m_{53} = e^{lT_1} \tag{A21}$$

$$m_{54} = -T_1 m_{53} \tag{A22}$$

$$m_{55} = -m_{51} \tag{A23}$$

$$m_{56} = -m_{52} \tag{A24}$$

$$m_{57} = -m_{53} \tag{A25}$$

$$m_{58} = -m_{54} \tag{A26}$$

$$m_{61} = m_{55} \tag{A27}$$

$$m_{62} = \left[\frac{3+lT_1+\frac{\lambda_1}{G_1}+lT_1\frac{\lambda_1}{G_1}}{l\left(1+\frac{\lambda_1}{G_1}\right)}\right]e^{-lT_1} \tag{A28}$$

$$m_{63} = m_{53} \tag{A29}$$

$$m_{64} = \left[\frac{3+lT_1+\frac{\lambda_1}{G_1}+lT_1\frac{\lambda_1}{G_1}}{l\left(1+\frac{\lambda_1}{G_1}\right)}\right]e^{lT_1} \tag{A30}$$

$$m_{65} = m_{51} \tag{A31}$$

$$m_{66} = -\left[\frac{3+\frac{\lambda_2}{G_2}+lT_1-lT_1\frac{\lambda_2}{G_2}}{l\left(1+\frac{\lambda_2}{G_2}\right)}\right]e^{-lT_1} \tag{A32}$$

$$m_{67} = m_{57} \tag{A33}$$

$$m_{68} = \left[\frac{-3-\frac{\lambda_2}{G_2}+lT_1-lT_1\frac{\lambda_2}{G_2}}{l\left(1+\frac{\lambda_2}{G_2}\right)}\right]e^{lT_1} \tag{A34}$$

$$m_{75} = e^{-l(T_1+T_2)} \tag{A35}$$

$$m_{76} = -(T_1+T_2)m_{75} \tag{A36}$$

$$m_{77} = e^{l(T_1+T_2)} \tag{A37}$$

$$m_{78} = -(T_1+T_2)m_{77} \tag{A38}$$

$$m_{85} = -m_{75} \tag{A39}$$

$$m_{86} = \left[\frac{3+\frac{\lambda_2}{G_2}+l(T_1+T_2)+l(T_1+T_2)\frac{\lambda_2}{G_2}}{l\left(1+\frac{\lambda_2}{G_2}\right)}\right]e^{-l(T_1+T_2)} \tag{A40}$$

$$m_{87} = m_{77} \tag{A41}$$

$$m_{88} = \left[\frac{3+\frac{\lambda_2}{G_2}+l(T_1+T_2)+l(T_1+T_2)\frac{\lambda_2}{G_2}}{l\left(1+\frac{\lambda_2}{G_2}\right)}\right]e^{l(T_1+T_2)} \tag{A42}$$